uc3m | Universidad Carlos III de Madrid

University Degree in Aerospace Engineering
2018-2019

Bachelor Thesis

"Metrological Analysis of 3D Printed Materials"

Ignacio Egido García

Álvaro Vaz-Romero Santero
Leganés, 2019

Abstract

Leading the industrial sector is what every company seeks. Inside the metal business there are a lot of competing parties that are on a constant searching for the best characteristics. New material properties or the latest technology are key factors that have an influence on riding high or not. One of the most recent building processes that is being slowly implemented on the modern industry of this century is the 3D manufacturing. This method puts an end to huge traditional building machines machines such as the ones used in conventional milling or forming processes, and forgets about joints and unnecessary wastes of material, being able to create difficult shapes that would otherwise be impossible to build.

Apart from its engaging theory, the other side of the coin shows a not so charming face. A big ignorance arises with this technology, as the lack of investigations and experiments leads to a disbelief that the metals will behave properly during service. This research intention is to continue with the small existing previous work, testing metals and checking its behavior under several circumstances. In order to help with this task, a profilometer will be used as the main equipment, a machine that is able to take images of a few micrometers and retrieve important data that can be further analyzed.

Stainless Steel specimens with two different porosities are going to be built and tested with Uniaxial Tensile Tests at three different temperatures, and their main breakage characteristics are going to be examined together with their porosity features. Variables to analyze will include roughness, fracture surface and necking. With this information, a study of the ductility of the material is going to be done, checking if there are differences in the Stainless Steel behavior in the whole range of the pieces.

Acknowledgments

I would like to express my great appreciation to my tutor Álvaro. Advice given has been a great help during the whole project.

I am also particularly grateful with my family, who has always supported me no matter what, taking away pressure when things were not working.

Finally, I wish to extend my thanks to my friends, for paving the way and encourage me at all times.

Contents

List of Figures

List of Tables

1 Motivation

Industrial requirements are in a continuous evolution due to the advance in technology. As it progress, the needs that arise vary, and as the rate of the improving technology is abrupt, these changes happen so quick that demand a nonstop and rapid investigation to meet them. Designing new manufacturing alternatives has turned out to be one of the most interesting investigation lines [13].

One way of coping with the industrial necessities is attained with the correct selection of the materials. Exploring new alternatives requires a high initial capital investment but, if it is done well, it can provide savings that remarkably overcome the original cost. Regarding metals, industries are now appealing for light alloys that can behave like their big brothers.

Inside the metal industry, one of the giants that deserves to be mentioned is the steel industry, as it is the second global largest one after the oil and gas industry. Steel in all its forms, even taking part in some alloys, offer a wide range of properties and applications, acting also as a key feature of innovation and growth in the automotive and aerospace sectors. Manufacturing cars, home appliance, cargo ships, surgical instruments and construction products are some of the other applications that steel can meet [14, 15]. Unfortunately, the steel sector has been mistreated during the world crisis, lowering the investments in infrastructure and machinery, and is still healing from the latest years [15].

Not only the recession has made its point into metal investigation but also national and global regulations. Just as an overview, in 2017 T.V. Narendran, managing director of Tata Steel, said that *"with new regulations in safety and emissions, the automotive material mix is expected to significantly change towards increased adoption of higher strength and corrosion resistant materials"* [16].

Computer based models are found to be an option; carrying a software that is able to come up with a solution without testing it first saves money and time. By implementing beforehand the metal characteristics it can retrieve a quick and reliable prediction of the test. However, concerning different manufacturing options, Additive Manufacturing emerges. 3D printing is a roughly new manufacturing process where a computer-aided design is sliced into small layers and built up by addition of these pieces with a powder of the metal as raw material. It is transforming the manufacturing industry, setting new guidelines for a proper use [17].

The problem of this manufacturing process arises with the quantity of flaws that can appear in the final piece. Microstructural defects, inclusions and porosity will definitely play a role in the built specimen. Besides, the cost of building a piece will depend on the porosity that it is desired. These defects will change the properties of the metal, altering the final characteristics and therefore its applications. This study aims to identify them and check how are going to be influenced by external factors such as temperature. Being able to do so can help to make a classification and ease the later selection of the material depending on the sector in which the metal is being implemented.

2 Objectives

During this investigation, Stainless Steel (SS 316L) specimens previously manufactured using AM technology (Selective Laser Melting) will be analyzed. These samples were manufactured following two possible building orientations and keeping two porosity grades. The final outcome is understanding the effect that manufacturing anisotropy and intrinsic porosity has in the material performance. In this work only one building direction and two porosity grades have been accounted for.

Since this research is embedded inside a bigger university project, and it has been done during the first steps of it, its main objective is to serve as an approach for the beginning and act as a guide for the continuity of it. For that reason, and under the premise of trying to clarify the methods and steps that can be used, the goals that are expected to be reached are:

- Learning the 3D building process of metals through Selective Laser Melting.
- Understanding the functioning of a profilometer and the intrinsic technology.
- Making a study of how stainless steel specimens built in the axial direction with Selective Laser Melting (SLM) work under uniaxial tensile tests at three different temperatures and two distinct porosities. This study includes:
  - A roughness metrological analysis.
  - An inspection of the pores, checking if they have suffered a coalescence and taking data such as its diameter and volume.
  - Ductility examination through maximum fracture height and radius of curvature variation at necking. Recognition of differences in ductility when changes in temperature and porosity are made.
  - 3D image processing of the fracture surfaces and necking regions of several specimens, as well as augmented pore figures to use them as a tool for a better comprehension.

3 Introduction

In this introductory chapter, previous knowledge about the manufacturing process is going to be explained: the specimens design, the parameters used or the technology with which the machine works. Between both the Introduction and Methodology sections these concepts are going to be presented.

3.1 Selective Laser Melting

When speaking about Selective Laser Melting (SLM), additive manufacturing (AM) has to be pronounced, as it is one of the techniques existing for this end.

Additive manufacturing aims to be a conjunction of processes with the unique goal of shaping a part. The key thing here is that AM works layer-by-layer, opposing with the well-known shaping processes such as machining, welding, molding or forming [1]. This allows the creation of difficult shapes that would otherwise be impossible to build, avoiding the use of joints that can vary the mechanical properties of the material and eliminating the unnecessary waste of material that most of the time is made.

Other advantages of Additive manufacturing in top of that would be the removal of moulds to construct the pieces, and also of the chemicals such as lubricants or coolants [18]. For these reasons, AM is now being accepted as a good choice over conventional techniques, gaining a place in small production.

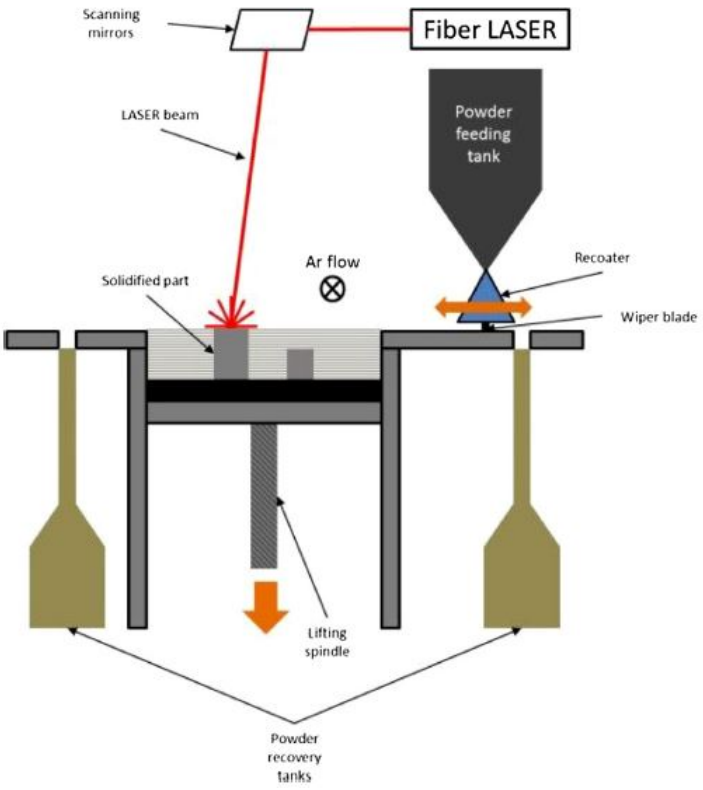

Figure 1: Principle of SLM processes [1].

Selective Laser Melting directly transforms a 3D model into a piece, dividing it into small coats of the order of micrometers and adding powder material in a layered way. Having the initial powder of the selected metal, a system deposits the required powder quantity above the previous layer. A tank feeder delivers material thanks to gravity, and a recoater moves distributing it (Fig. 1) [1]. Afterwards, a laser provides the temperature that melts together the actual and the previous layer (Fig. 2). That temperature has to be, at least, the melting temperature of the metal that is being used.

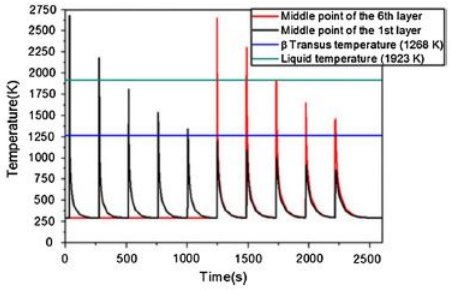

Figure 2: Thermal history of a Ti-6Al-4 V allow manufactured in WAAM [1].

It provides higher production rates, as it avoids the creation of dies and mechanization lines, but it also has limitations. Surface roughness increase when building a sample with this technology [19], and contamination in the parts regarding the printing process can affect the latter behaviour of the piece. In other words, it is not straight forward to make an estimation of the mechanical properties or the performance under some circumstances such as fatigue, as they will depend on a lot of factors, some of them uncontrollable.

3.1.1 Factors influencing the final properties of a SLM part

The emergence of flaws, superficial or not, will play a role on the properties of the final piece. Although some of then can be warned, the amount of factors involved is so large that would be impossible to prevent the appearance of defects.

Over the list given by Spears [20], including up to 50 parameters, just a dozen are thought as controllable. The whole set can be divided in four groups, depending on if they are laser, powder, powder bed or environment parameters. For example, in the case of the laser properties, the Average Power P_L (which is a measure of the total energy output of a laser) can be controlled. On the contrary, the Mode (continuous wave or pulsed), Peak Power P_{peak} (maximum power in a laser pulse), Frequency f (pulses per unit time) or Wavelength λ (distance between crests in laser electromagnetic waves) are predefined quantities.

Same will happen with the rest of the groups. The powder characteristics include the Melting Temperature T_m (temperature at which material melts), Boiling Temperature T_b (temperature at which material vaporizes) or Bulk Density ρ_b (material density) among others, all of them predefined. For the case of the powder bed, some of the controlled parameters will be the Deposition system parameters (recoater velocity, pressure, recoater type) and the Layer Thickness L (height of a single powder layer). Lastly, on the environment group, the Ambient Temperature T_∞ would be an example of a controllable parameter.

The list is really long and intents to show how difficult could be to balance the whole set. It can be extended for sure, increasing the difficulty of having everything in mind.

3.2 Profile and Areal Field Parameters

Surface metrology is a branch of metrology that studies the surface texture of a material. Its main related word is roughness, but it comprises everything related with small features measurements on the surface of a piece. Dealing with roughness has plenty of advantages, they go from reducing wear and therefore increasing the part lifespan to clean appearance on objects, which will be more interesting in an economical matter [10].

Regarding metrological studies, surface texture will definitely play a role. It will consist on extracting useful data from topographical measurements. As the information that can be obtained is so wide, there are several standards to classify it; parameters such as heights and distributions are included in the ISO specification standards [2].

- ISO 4287: involves profile measurements, and it is used in the 80% of the literature. Its main parameter is R_a, the arithmetic mean deviation of the assessed profile, and works with other like R_q or R_t that are specified in Table 1.

Parameter	**Units**	**Meaning**
R_a	μm	Arithmetic mean deviation
R_q	μm	Root mean square deviation
R_t	μm	Total height
R_p	μm	Maximum peak height
R_v	μm	Maximum pit height
R_z	μm	Maximum height
R_c	μm	Mean height
R_{sk}	[-]	Skewness
R_{ku}	[-]	Kurtosis

Table 1: ISO 4287 amplitude parameters - roughness profile [10].

- ISO 25178-2: encompasses areal parameters. It is not as used as previous standard, as it is included in the 20% of the cases. Its main feature is S_a, the analogous of R_a in an areal way, the arithmetical mean height of the scale limited surface. Different areal parameters are detailed in Table 2.

Parameter	**Units**	**Meaning**
S_a	μm	Arithmetic mean height
S_q	μm	Root mean square height
S_p	μm	Maximum peak height
S_v	μm	Maximum pit height
S_z	μm	Maximum height
S_{sk}	[-]	Skewness
S_{ku}	[-]	Kurtosis

Table 2: ISO 25178 height parameters [10].

Both R_a and S_a are the most used parameters. Profile measures have a lack of information, for example, Fig. 3 shows the difficulty trying to distinguish between a pit or a scratch. And, while it is true that areal parameters tend to give more information, as it is a three dimensional feature and reality goes in three dimensions too [2], it is important to be aware that the result is going to change depending on where the measure is done, its amplitude, the orientation and the resolution that it is being used. It is therefore important to work always with the same conditions in order to make good estimations and proper comparisons.

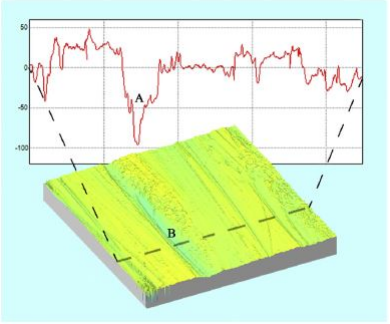

Figure 3: Profile measurement extracted from an areal measurement. 'A' generates doubts about whether it is a pit or a scratch, and 'B' clarifies that it belongs to a scratch [2].

Previous studies show how S_a changes with some specific parameters. As it has been previously mentioned, there is a wide number of parameters that have an influence on roughness, so the range of possibilities is huge. Each research focus on its own interests. The following list includes some of them:

- S_a decrease with heat input (laser power) except for θ=35º (lower heat dissipation).
- High energy contour conditions gives a smoothing effect.
- The increase of the beam diameter leads to an increase of the surface roughness.
- Increase of scan velocity increases S_a. This one can be deducted due to the unmelted powder particles that can stand when decreasing the velocity [7].

Augmentation alter the parameters too; lower magnification objectives will let complete tracks to be seen while higher ones will show smaller features. The choice will depend on the investigation concerns. Besides that, some parameters changing the roughness won't influence it anymore depending on the magnification used [4].

3.3 Material

SS316 stands for Grade 316 Stainless Steel. It is one of the most typical AM alloys and it will be compared with different ones in a bigger magnitude project. From lower to higher percentage of appearance, nickel alloys are incorporated in just a 5% of the papers, being the Inconel 625 the one used in the 75% of them. Aluminium alloys amount another 5%, and refractory materials such as cobalt chrome or alumina a 7%. Ongoing, titanium allows cover a 34% of the references, with Ti6Al4V being the main choice 94% of the times. Ultimately, and as far as it is concerned, stainless steel alloys comprise a 39%, with SS316L in the 70% of the references [2]. Grade 316L is a low carbon version of 316 that is going to be cited along the following lines.

The stainless steels are arranged in families according to its crystalline structure. They refer to some metal proportions, and are the Austenitic, Ferritic, Duplex and Martensitics & Precipitation Hardening families. On top of that, each family has different stainless steel grades regarding to specific properties, usually denominated with three digits, as stated by the Society of Automotive Engineers (SAE).

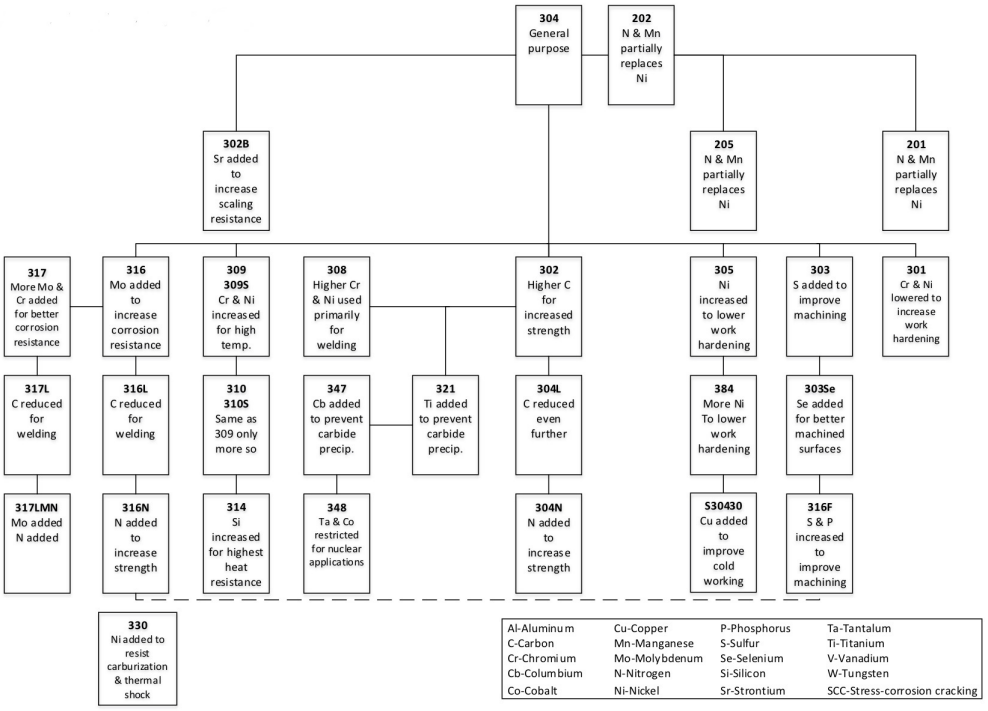

Figure 4: Austenitic stainless steels [3].

The austenitic family is the most used, and it basically includes chromium and nickel along with manganese and molybdenum in some cases. Their main feature is their toughness and their corrosion and creep resistance [3], and the most famous one is Grade 304, followed by Grade 316.

Coming out of Figure 4, Grade 316 differentiates from Grade 304 with the addition of molybdenum, that increases the corrosion resistance especially to pitting and crevice in chloride environments. Also, it has good forming and welding characteristics, making it a perfect choice for industrial applications [11].

3.3.1 Composition

Grade 316 embraces several stainless steels apart from Grade 316 itself. The low carbon version, Grade 316L, and the high carbon version, Grade 316H, which behaves properly under high temperatures, are the most famous ones. Together with these three main versions, there are additionally Grade 316Ti and Grade 316N.

Grade		C	Mn	Si	P	S	Cr	Mo	Ni	N
316	Min	-	-	-	0	-	16.0	2.0	10.0	-
	Max	0.08	2.0	0.75	0.045	0.03	18.0	3.0	14.0	0.10
316L	Min	-	-	-	-	-	16.0	2.0	10.0	-
	Max	0.03	2.0	0.75	0.045	0.03	18.0	3.0	14.0	0.10
316H	Min	0.04	0.04	0	-	-	16.0	2.0	10.0	-
	Max	0.10	0.10	0.75	0.045	0.03	18.0	3.0	14.0	-

Table 3: Composition ranges for Grade 316 [11].

3.3.2 Properties

Related with properties, they can be split in two categories, mechanical and physical. Table 4 shows the most significant ones.

Measurement	Range (after heat treatment)	Standard
Density	7.9 g/cm^3	
Tensile Strength	485 – 595 MPa	DIN EN ISO 6892-1:2009
Elongation at Break	25 – 55%	DIN EN ISO 6892-1:2009
E-Modulus	180 GPa	DIN EN ISO 6892-1:2009
Yield strength	380 – 560 MPa	DIN EN ISO 6892-1:2009
Hardness	89 HRB	DIN EN ISO 6508-1
Relative Density	Ca. 100%	
Specific Heat Capacity	500 J/(kg K)	
Air - and Watertight	Yes	

Table 4: Datasheet of Grade 316 [12].

All the information included in this table about the Stainless Steel properties has been retrieved from the Datasheet given by *Materialise*, the company that has granted the specimens for the investigation.

3.3.3 Applications

From Atlas Steels Grade Data Sheet [21], the main applications for this stainless steel comprise:

- Food processing equipment.
- Laboratory equipment.
- Architectural panelling, railings and trim.
- Boat fittings.
- Chemical containers.
- Heat exchangers.
- Screens for mining, quarrying and water filtration.
- Threaded fasteners.
- Springs.

3.4 Equipment

This section aims to clarify the technology used in order to make the post testing analysis. What is a profilometer, how does it work and how it is going to be used are some of the topics that will be covered.

Another characteristic that will determine the metrological parameters is the technology used to make the inspections. The accuracy and precision of the instruments will govern the quality of the measurements [2].It is therefore useful to understand how the machinery works.

The profilometer is the tool that will allow the measurements on roughness to be taken, as well as images and traces or pores information. It can be thought as a microscopy that uses the finest technology to create 3D images with a sufficient accuracy. The different pieces that it includes are presented on Figure 5 in a schematic way. Optical lenses are brought together with a sophisticated lightning system and a CCD sensor. CCD stands for Charged Coupled Device; it drives pixels with RGB colours, is more sensitive to light and captures a wider range of tones than other similar sensors [22].

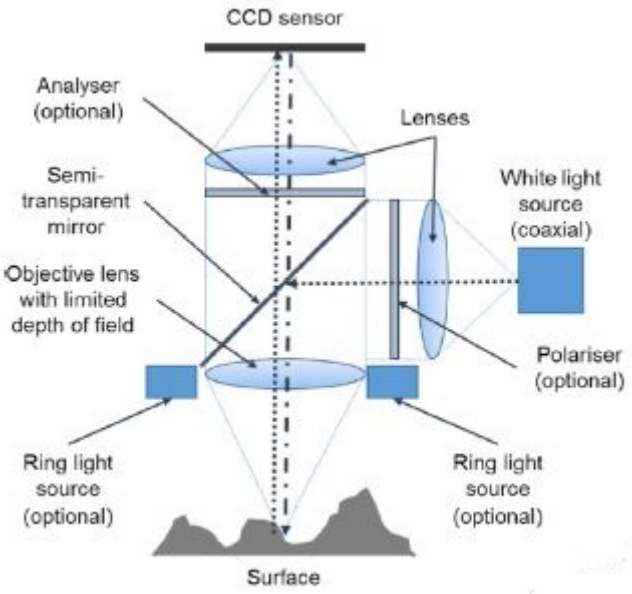

Figure 5: Focus variation scheme [4].

3.4.1 Focus Variation

But, how does it create the 3D images? Well, focus variation (FV) takes a determined number or images, starting from the bottom of the piece to a top selected height, moving along the Z direction. An embedded algorithm within the machine takes each pixel of a single image, that will coincide with a certain XY location, and measures the contrast with respect to the surrounding pixels, that will be brighter, darker or the same shade. This procedure is repeated for the corresponding same pixel of every taken image, and will give a contrast curve for each pixel when combining the whole X, Y and Z information, creating a 3D point [4]. The same process repeated for the totality of the pixels will give the related final image (see Fig. 6).

When compared with other optical technologies, focus variation is ahead of its rivals. Profile projectors do pattern matching comparing the image with a reference. They have the advantage of quick measurements, but are bounded to two dimensions. Also, orientation defines the results, that will vary with it. Structured light is favourable for large objects due to its velocity when processing images. However, it has a low depth of field and that limits its applications. Confocal measurement can be used with smooth surfaces such as silicon, and White light interferometer (WLI) struggles with surface roughness but behaves properly with lenses and glass structures [23].

Focus variation *"closes the gap between typical 3D coordinate measuring technology and classical surface metrology devices"* [23]. Complex pieces were measured under different technologies, depending on the perspective or needs. Now, FV can test form, dimension, position and roughness in a single system.

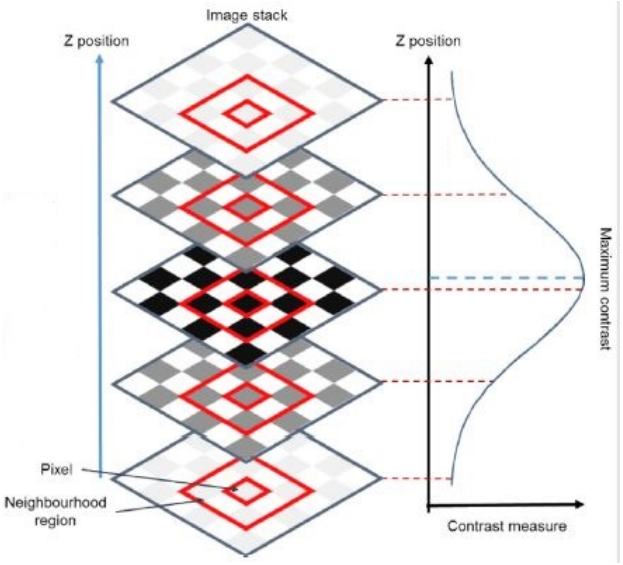

Figure 6: Image contrast curve in focus variation [4].

3.5 Specimen design

The design of the specimens where the tests are going to be performed is a key point for the investigation. They have been built according to a standard test method for tension testing of materials, particularly one from the ASTM norm denominated E8/E8M−13a. The acronym stands for American Society for Testing and Materials, and the number 13 is specifying the year of last reapproval.

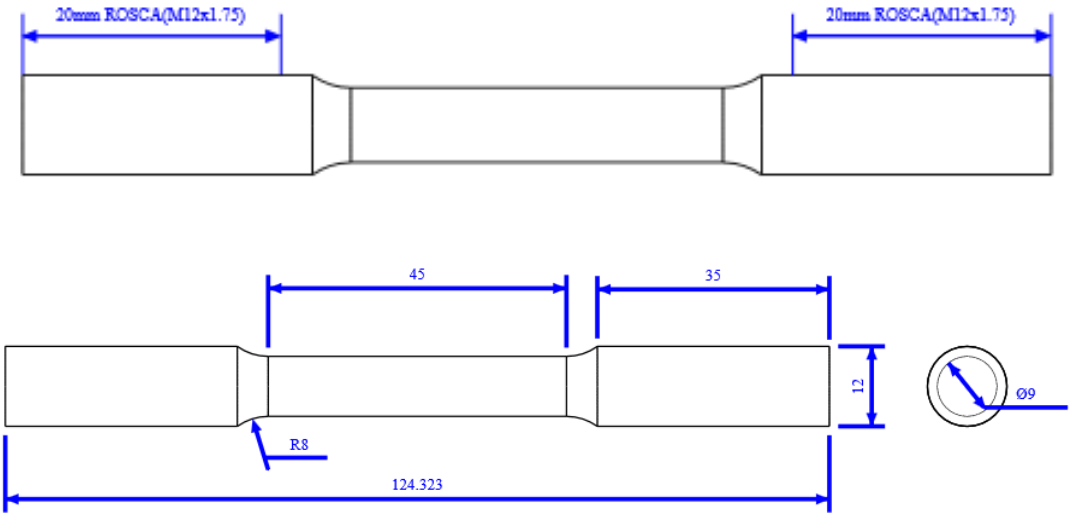

Figure 7: Specimen design.

In Figure 7 above, precise dimensions of the specimens can be seen, in millimeters. The shape that conforms with the standard is a cylinder with a central thinner part. The total cylinder length is 124.323 millimeters and the diameter is 12 millimeters, while the inner part ranges a total of 45 millimeters with a diameter of 9 millimeters. The two lateral bigger zones are 35 millimeters each, and the joint between the central and the lateral parts is done with a radius of 8 millimeters. Finally, the specimen is completed with a thread at both laterals of 20 millimeters long.

Having this in mind for the dimensions, then several specimens have been built with some differences, as a way of comparing them and observe how they behave under some circumstances. For that reason, the next distinction will be the building direction. There are two main orientations, commonly known as axial and flat. The axial piece would start to be built from one side to another along the Z-direction, whereas the flat would follow the XY-direction, requiring a support when the central part of the piece is being printed.

Figure 8 helps clarifying this two orientations; the left specimen will correspond to the axial one while the specimen on the right will be the referred as flat.

Another changed characteristic is chosen to be the porosity. There are going to be, again, two different ones, 99.5% and 95%. Subsequently, one last difference will be made, the temperature at which the tests are done. There will be three options: option one, that the test is performed at ambient conditions; option 2, that the test is carried out at 100°C; and the last one, option three, that the test is done rising the temperature up to 150°C.

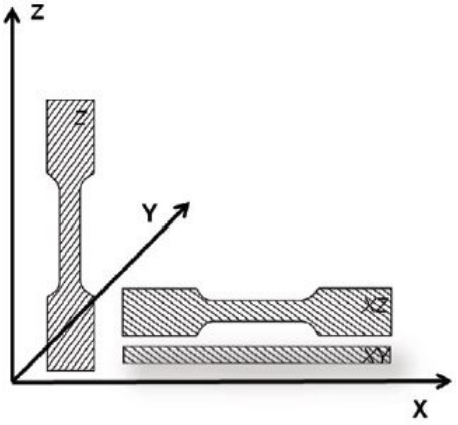

Figure 8: Building direction of the specimens [5].

The combination of each possibility will give a total of 12 specimens per material (2 building directions X 2 porosities X 3 temperatures). Within these lines, the cases of axial orientations are going to be studied.

- **SS316**
  - Axial
    - 99.5% of porosity
      - Ambient temperature
      - 100°C
      - 150°C
    - 95% of porosity
      - Ambient temperature
      - 100°C
      - 150°C
  - Flat
    - 99.5% of porosity
      - Ambient temperature
      - 100°C
      - 150°C
    - 95% of porosity
      - Ambient temperature
      - 100°C
      - 150°C

4 State of the Art

What has been studied about this matter has been done throughout the last years, as Selective Laser Melting is a relatively new technology, and 3D material printing is most expanded in plastic rather than in metals. Considering this fact, studies are more focused on analyzing the mechanical properties of the material per se or even the surface roughness than to carry out fracture tests and evaluate the results. By any means, it can be found some brush strokes about pores, crack initiation and crack growth.

4.1 Material characterization

Most of the existing papers center their attraction in defining the material, calculating its properties and comparing them with specimens built with conventional processes such as molding or forming. These features are going to be examined deeper in the following lines.

Densities are measured using the Archimede's method, which is really easy to use and does not require an X-ray machine. It is fast and cheap, and gives enough information. It consists on measuring the mass in air and in a fluid (usually water), and calculate the density afterwards with the following formula [7]:

$$\rho_p = \frac{m_a}{m_a - m_{fl}} \times (\rho_{fl} - \rho_a) + \rho_a \tag{1}$$

Mechanical properties will be affected by density: dense parts will have a finer microstructure, and therefore better flow stresses [24].

The main tests to determine the mechanical properties are tensile, hardness and Charpy impact tests. Building orientation turns out to be a decisive factor, as the samples present anisotropy in their properties. By considering its stress-strain curves, the elongation at break happens to be lower for the XY oriented [5].

Ductility has been checked for two different orientations, and parts with XY direction show differences with Z built specimens when doing tensile tests, but it is not affected in Charpy tests [5]. Besides, hardness is higher when observing it along the built direction than in the perpendicular one, while yield strength and ultimate tensile strength are isotropic [1]. These results can vary with the material, so nothing can be stated as general as the number of studies are still not enough.

Ultimately, the effect of heat treatment has been reported by Prashanth in order to see the changes in the mechanical behaviour of the specimens from a microstructure point of view, but the tensile tests were all performed at room temperature. The yield and the fracture strength decreased with the annealing temperature and the fracture strain increased because of the coarsing of the microstructure with annealing temperature [25].

4.2 Defects

Final properties are difficult to control because of the quantity of defects: porosities, hot cracking or poor surface state. Clusters from powders agglomeration can occur too [18].

Hot cracking stands for the formation of shrinkage cracks during the solidification of weld metal [26]. The inter-dentritic spaces of the weld metal can have a lack of liquid supply when the solidification range is large, causing cracking. As this defect is more present in an alloy, for example in AlSi10Mg or AlSi12, by adding more eutetic composition it can be reduced [1].

Balling, where coarse molten metal droplets are formed, is seen in Selective Laser Melting, and will give a determined surface quality [1]. Micro-pore formation can be caused because of balling [24].

Koutiri has also studied that, for high cycle fatigue, cracks are initiated mostly due to porosities on the surface or sub-surface, high surface roughness that produces stress concentrations, and unmelted particles close to the surface [7]. As porosities are the main defect, they are evaluated in a separate section.

4.2.1 Porosities

Porosities are the biggest defect in a specimen built with Selective Laser Melting technology. With density calculations it can be retrieved a lot of information about the level of porosity, and therefore about how the material will behave. Galy divides the pores in two types, depending on the cause that originated them: metallurgical, if they are due to surrounding gas absorption, and parameter based, if are the consequence of a flaw [1]. An example of a parameter based pore cause would be the laser scan speed: when it increases, the molten pool size decreases, and therefore the interaction between molten pores decreases too, leading to porosity [24].

The bigger the pore, the most dangerous it is, as it will be responsible of cracks, especially if it is not spherical. On top of that, big pores can appear with the coalesce of smaller ones. Regarding the parameter based pores, they can be formed due to the presence of impurities, low absorption of energy, atmospheric conditions, evaporation process, etc. [1].

Together with the geometry, the size of the pore and the place of the specimen where it appears are important features. In the sample volume, it is likely to be circular and to have a size between 10 to 40 μm while when reaching the surface the sphericity is decreased and the size increase to 150 and 200 μm [7]. Building orientation will affect porosity too: horizontal printed specimens have more possibilities of having pores, and its porosity is reduced after dynamic testing [24].

An investigation with X-ray is interesting, as it can be analyzed the evolution of the pores effortless. Brayshaw conducted something like this with 3D X-ray tomography. Figure 9 shows the initial porosity: left sample presents pores of 50-100 μm with a level of plastic straining, and right sample pores of 10 μm, except for a larger one. The porosity of these specimens is 81×10^{-5} and 4.4×10^{-5}, respectively [6].

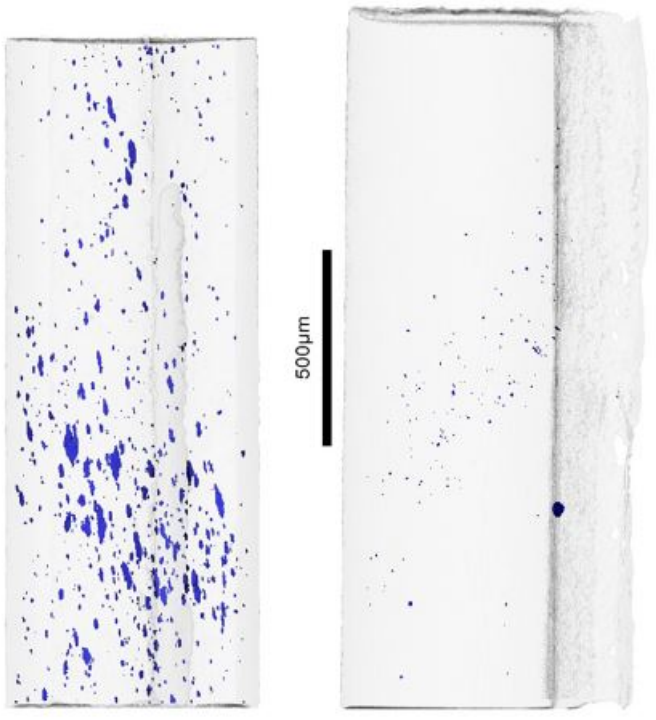

Figure 9: Initial tomography of two different specimens [6].

After the fracture, voids are significantly increased closed to the fracture surface due to void nucleation and growth. The large void away from the fracture zone in the right sample of Figure 10 is probably initial porosity [6].

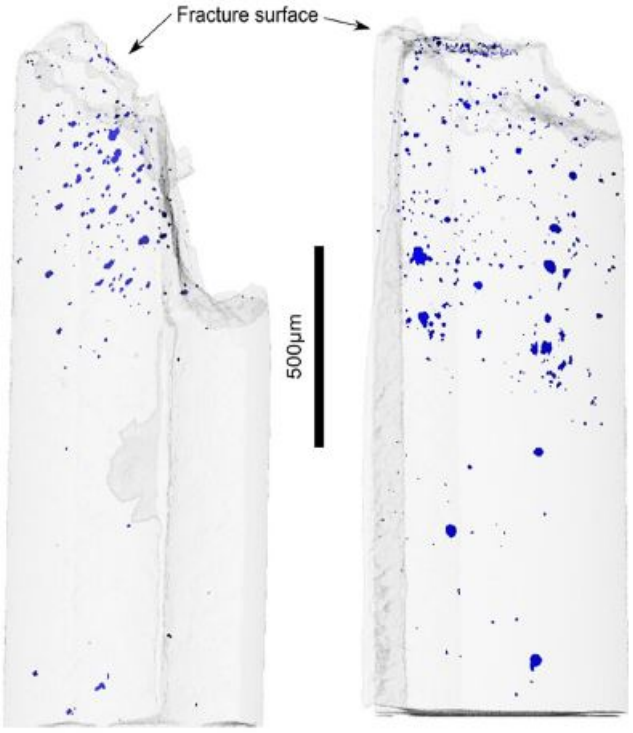

Figure 10: Tomography after fracture of two different specimens [6].

4.3 Fracture surface

Large pores near the border make parts more sensitive to crack initiation. That evidence, along with the fact that they are more numerous in Z built oriented specimens, make them a critical defect [5].

Koutiri made a comparison between re-polished and as-built SLM specimens failure mechanisms. When analyzing re-polished parts, the crack initiation happened because of two reasons, depending on the specimen: one crack initiation occurred on the sub-surface without any defect, and it was the material plasticity what had controlled the fracture, while the other was due to pores below the surface. For the case of as-built parts, three mechanisms were seen to affect: particles embedded on the surface, the most harmful, the degree of porosity close to the surface and the local plasticity of the material [7].

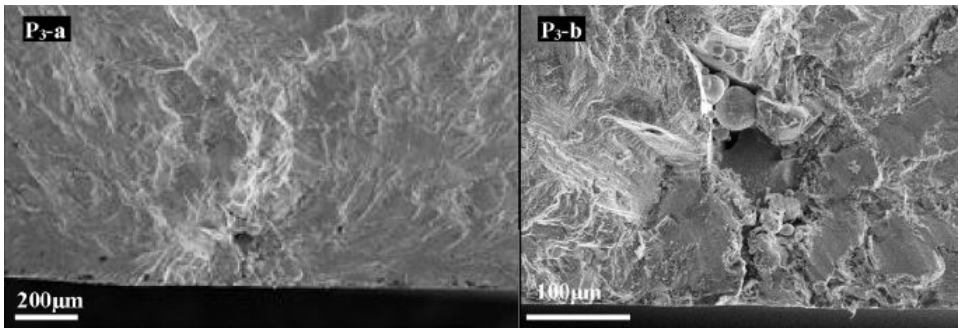

Figure 11: Crack initiation image of a polished specimen [7].

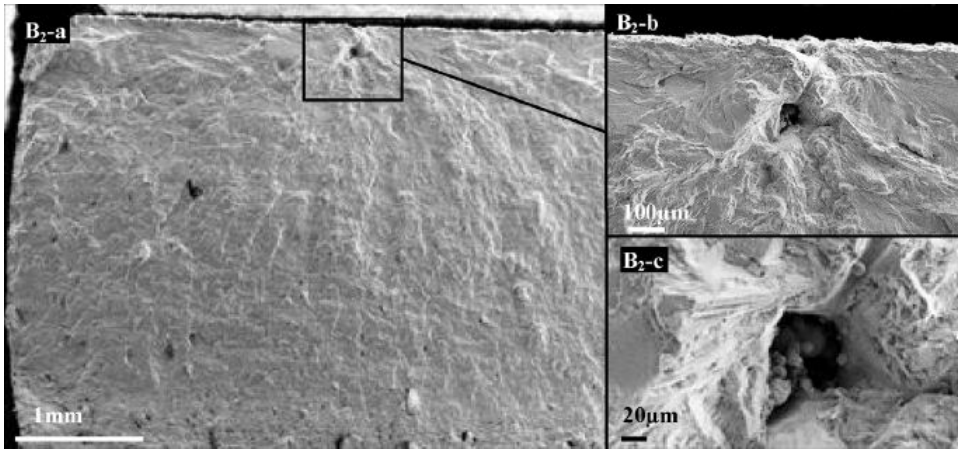

Figure 12: Crack initiation image of an as-built specimen [7].

Rashid checked that the way a sample failed had something to do with the building orientation. Horizontal specimens failed due to high porosity, and inclined and vertical ones either by lack of fusion or bulk porosities [8].

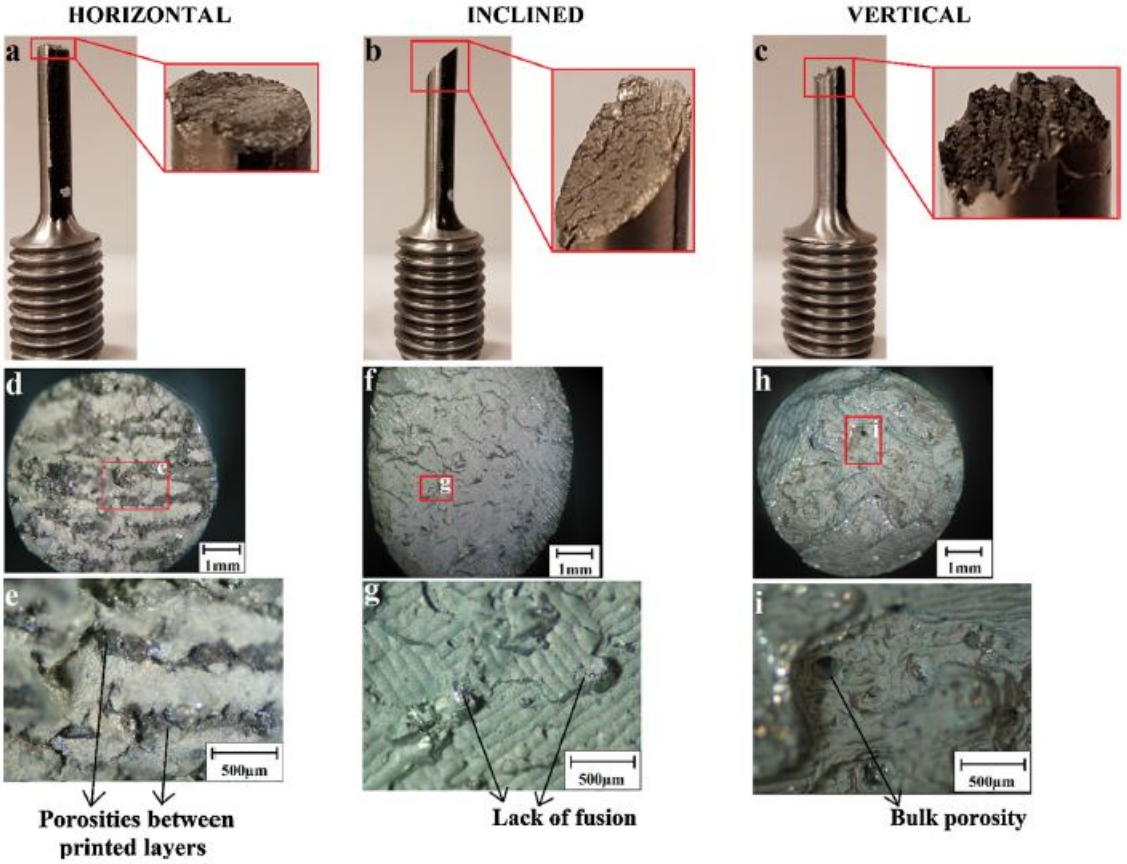

Figure 13: Fracture surface for three different building orientations [8].

Lastly, Manfredi studies show fracture surfaces after tensile tests. He assumed that the failure could have been because of a ductile fracture or the result of growth and coalescence of micro-voids. When amplifying the fracture surface, the dimples shown showed the energy of fracture dissipation ability. The dimensions of these micro-voids went from 250 to 500 nm per side, and the dimple thickness of about 60 nm [18].

Concerning crack growth testing, it always includes a pre-crack specimen subjected to stress, and then the measure of the growth of that crack is performed [27]. Moreover, crack growth energy changes with temperature. From Prokic experiments, at room temperature it is higher than crack initiation energy whereas at -40°C and -55°C is the other way around, crack initiation energy is higher than crack growth energy [28].

5 Methodology

Once the specimens are built through Selective Laser Melting technology, they are tested through a uniaxial tensile test. This test is commonly used to characterize the material behaviour under quasi-static loading conditions. In addition, a fracture surface analysis can help to understand the material response due to inhomogeneities, flaws or particles in the microstructure.

5.1 Uniaxial Tensile Test

The test consists on subjecting an specimen to a controlled tensile displacement along a single axis. Specifically in a uniaxial test, the displacement is usually kept at a constant rate. Identifying its response to loading gives an stress-strain curve, that supplies elastic and plastic properties, and make possible the calculation of the Young's modulus, yield stress, ultimate tensile strength and elastic strain energy density [29].

The test is performed until total fracture of the specimen, changing completely its initial shape and giving not only a curve but also a new form to study. Additionally, the test is done under three different temperatures for each of the porosities in order to check if and how this factor affects the behaviour of the material.

5.2 Measurements

The methodology proposed is described in detail below.

5.2.1 Roughness

The first parameter to be obtained is the material roughness, a standard variable in surface metrology.

Although it has been already pointed out, it is worth noting that measurements have to be taken in a very rigorous way, following always the same steps and taking care if the results are wanted to be consistent with each other. A small variation within each measurement will override the whole set of calculations. Being more specific, lighting has to be always the same, resolution has to remain unchanged, and the size of the line or box where the results are being obtained too. All of the roughness measurements have been taken on the flat side of the specimen in order to avoid any kind of curved zone that could spoil the results.

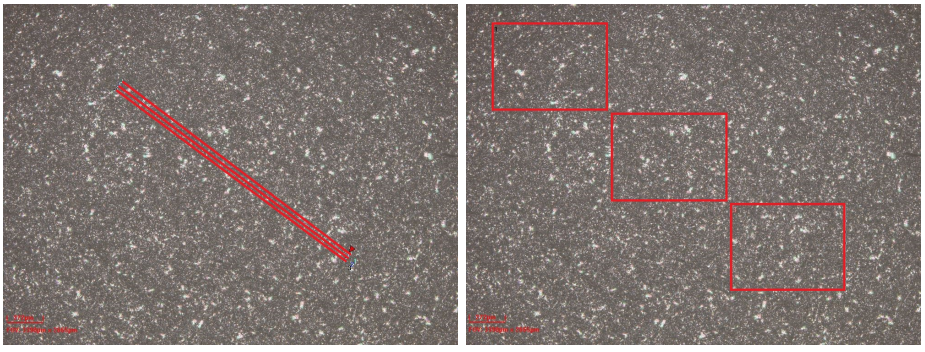

Figure 14: Roughness measurement. On the left, R_a parameter; on the right, S_a.

Figure 14 shows the line from where R_a is being calculated on the left, and the same but for S_a on the right. As S_a is an areal parameter, the way it is computed is by selecting a zone on the image, and placing a box with always the same dimensions and geometry. This procedure is done three times for both the profile and the areal parameters, and the mean of the different values is finally considered. The chosen lightning is around 30% for the 5X augmentation and 22% for the 20X. The figure is darkened for a better view of the selected area. For the resolution, the size per step selected is 2 μm for all the augmentations.

Each data has to be accompanied with its error/uncertainty. Equations [2] and [3] show how it is calculated. The first one gives the Standard Deviation (SD, or σ), that measures how much the values vary from one another. Thenceforth, The Standard Error of the Mean (SEM), which quantifies how precisely you know the true mean [30], is computed from the SD, following the second equation. The "n" factor represents the number of observations, x_i each of them and $\dot{x}$ the mean. These errors are included in the graphs and help clarifying the results.

$$SD = \sqrt{\frac{\sum_{i=1}^{n}(x_i - \bar{x})^2}{n-1}} \tag{2}$$

$$SEM = \frac{SD}{\sqrt{n}} \tag{3}$$

5.2.2 Fracture surface

For the inspection of the fracture itself, a stitching is done in order to have a general view of the surface, as with such an augmentation is not possible to create a complete image. What a stitching consists on is to concatenate small sections of the piece with a 10% of overlapping and create a bigger image with all of the small views. In order to encompass the whole surface, a 3x2 stitching has been done, which means that a total of 6 images have been obtained individually before the final concatenation.

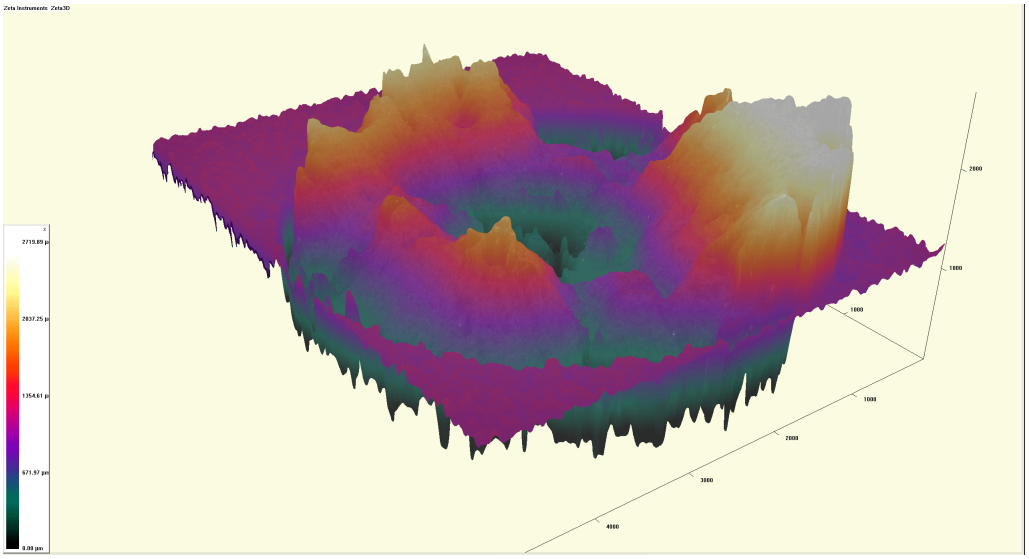

Figure 15: 3D Fracture Surface representation of a 99.5% porosity, T_{amb} specimen.

From the stitching, a 3D representation of the fracture is obtained, colored with false colours in order to understand the peaks and valleys of the surface. White and yellow zones correspond to the highest points of the surface, while, on the contrary, black and green correspond to the lowest ones. Having this in mind, a cross section is made as a way of calculating the fracture height. By substracting the value of the highest point and the value of the lowest point it can be obtained that distance. Figure 16 shows how this cross section is set for the 99.5% porosity, T_{amb} specimen. The value acquired will be presented in the Results section.

Along with the fracture height, the stitching can help to identify and select an interesting pore, and make some calculations of the diameter, that will serve as a first approximation.

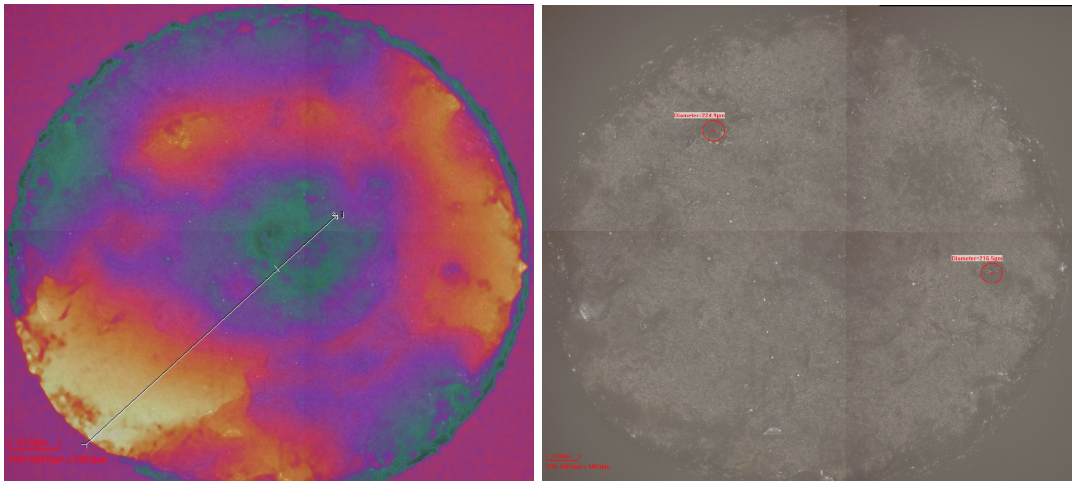

Figure 16: 2D Fracture Surface representation of a 99.5% porosity, T_{amb} specimen. On the left, cross section used for the fracture height calculation; on the right, pores selection and diameter approximation.

5.2.3 Pores

Concerning pores, the procedure to use will be the following. Once the fracture surface is already inspected, a zone is going to be chosen by looking at it, having as a guide the specimen itself as well. False colours help with this task as the most evident pores may be seen directly. After the desired pore is selected, pictures with the 5X augmentations will be taken until centering it. The microscope objective will be changed to the 20X and 50X, if necessary, and data will be collected.

Information about pore shape, volume, height, and a possible coalescence will be retrieved, and 2D and 3D pictures of the pore and its surroundings too.

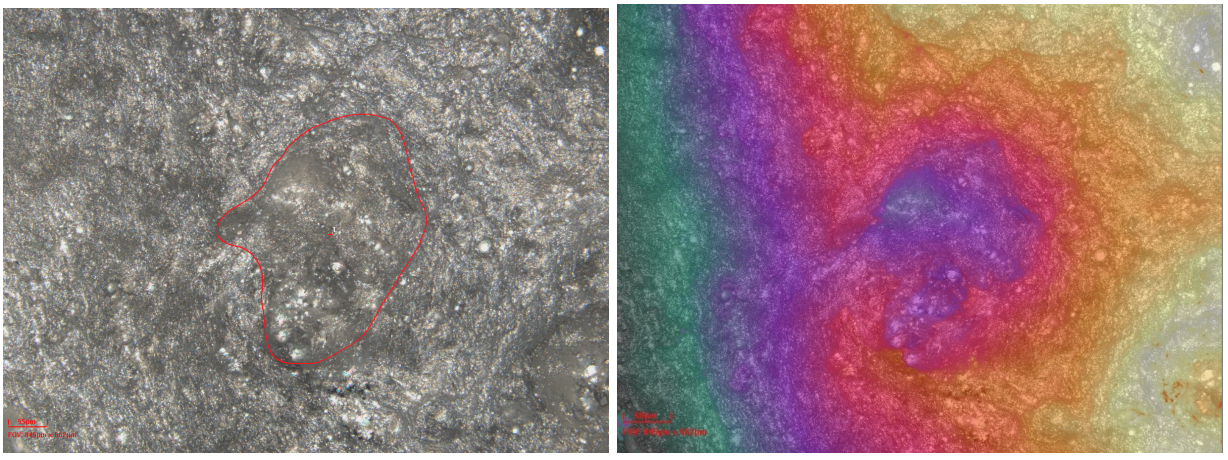

Figure 17: 2D Pore image of a 99.5% porosity, 100°C specimen at 20X augmentation. On the left, real colour image with the pore rounded in red; on the right, false colour representation.

5.2.4 Necking

Lastly, many information can be obtained from the necking of the piece. The necked region is big enough not to be fitted in with a single measurement, so a stitching is required too. A 3x3 stitching has been done for each necking, so a total of 9 images have been obtained previously.

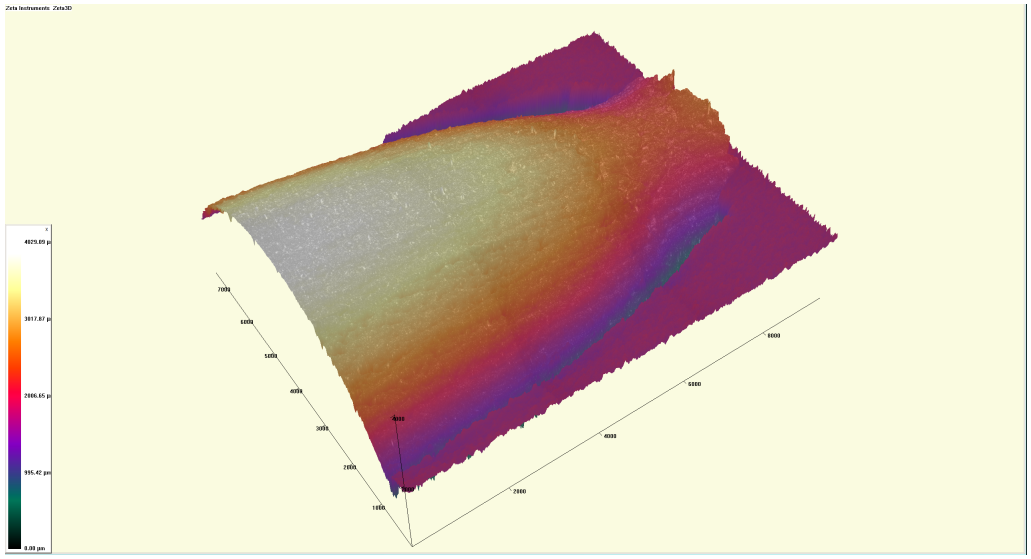

Figure 18: 3D Necking representation of a 99.5% porosity, 150°C specimen.

3D recreation aids to fully inspect the piece. Geometry variation can be examined, and even surface anomalies can be detected, if any. Also, from this step the radius of curvature changes can be appreciated. For a better comprehension, a few cross sections have been set along the necking to get a graph that will allow to calculate those radius of curvature. Figure 19 shows this method.

In order to compare every radius of curvature change, the ratio of the variation of the radius over the initial radius has been used. The information obtained from the total set of specimens is going to be presented on the next sections. The r_0 will be 4500 μm, that corresponds with the initial radius prior to the test, and the r_{final} the pink cross section, as selecting one more to its right would not represent properly the end of the necking and would lead to errors.

$$Ratio = \frac{r_0 - r_{final}}{r_0} \tag{4}$$

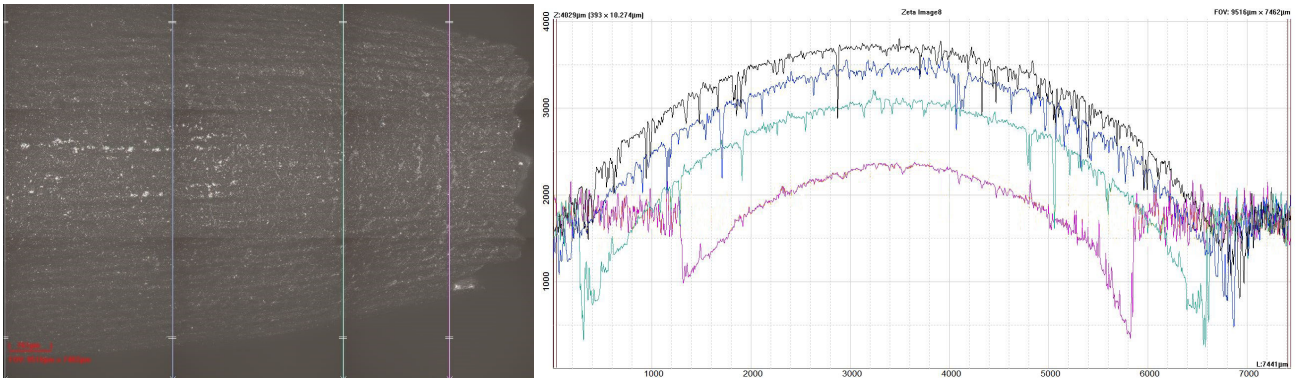

Figure 19: Radius of curvature variation for a 99.5% porosity, T_{amb} specimen. On the left, 2D view with the cross sections used; on the right, graph with the different radius or curvature.

6 Results

After performing the different inspections, the data retrieved from the whole set of specimens is presented below.

6.1 Roughness

For the case of roughness, measures of R_a and S_a were taken, finding particular results depending on the porosity and the temperature of the specimen, and depending on the augmentation. Two tables with those information are shown, one for each parameter, selecting the final mean of the three examinations.

99.5%	**5X**	**20X**	**95%**	**5X**	**20X**
T_{amb}	18.08	2.943	T_{amb}	21.46	5.126
100°C	18.10	2.995	**100°C**	21.17	5.191
150°C	18.32	3.074	**150°C**	21.53	5.136

Table 5: R_a $[\mu m]$.

99.5%	**5X**	**20X**	**95%**	**5X**	**20X**
T_{amb}	19.21	2.667	T_{amb}	21.44	3.790
100°C	19.24	2.647	**100°C**	21.39	3.746
150°C	19.03	2.609	**150°C**	21.37	3.791

Table 6: S_a $[\mu m]$.

Having all of the results together helps figuring out if they follow a certain behavior or not, and how is that behavior. However, a graph is always a better tool for that task, giving information about possible variations in the results, growths, errors, etc. Figures 20 and 21 present a comparison for the R_a and S_a parameters separately, including the SEM.

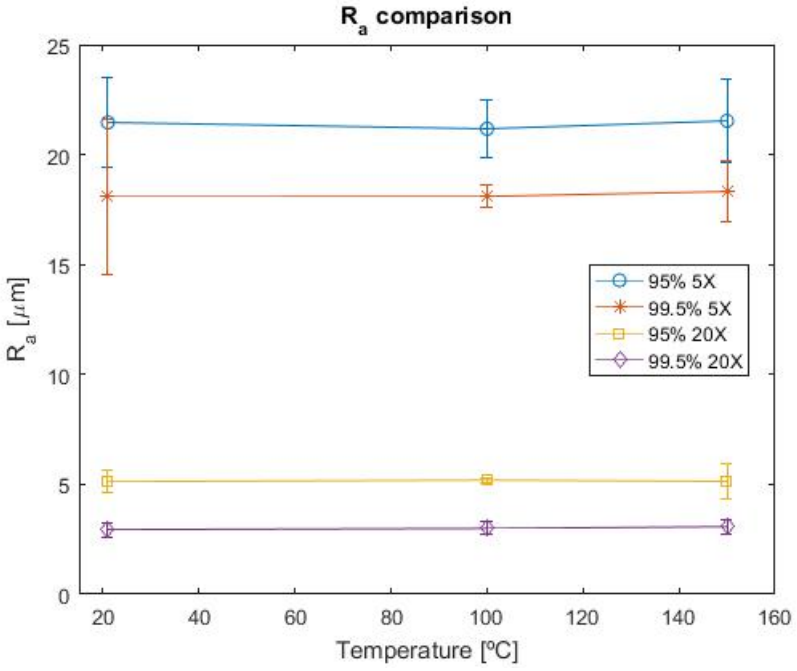

Figure 20: R_a against temperature comparison.

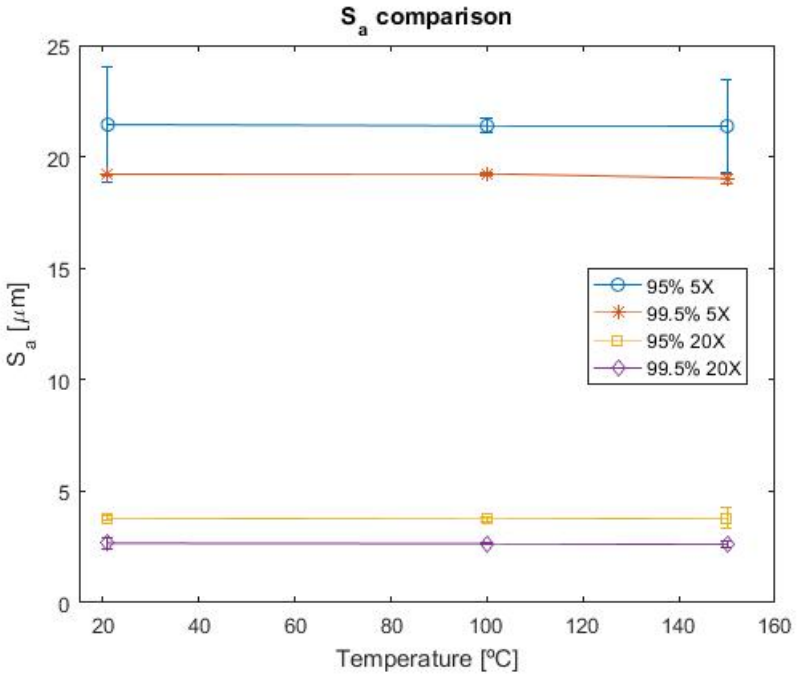

Figure 21: S_a against temperature comparison.

6.2 Fracture surface

The fracture surface has been analyzed by taking several 3D pictures of each of the specimens and measuring the maximum fracture height.

As the specimens have two parts, one for each side of the breakage, the total number of images is twelve. Figures are presented with the two parts together as a way of making an easy analogy and checking that both parts perfectly fit. Just before each 3D representation, pictures of the real specimen with which it corresponds are included. Fractures don't follow any path, and although it is true that in the majority of the cases a concave and a convex part can be differentiated, it is difficult to predict the mode of failure, or to state that the fracture is caused because of a certain pore without further analysis such as, for instance, a microstructure analysis using Scanning Electron Microscopy (SEM).

All of the images have been processed, applying a mathematical filter to mitigate and smooth spurious noise. At any rate, there is still some noise, in some of them more than in others, but adding more filters would distort the image too much, making it unreal.

Lastly, it is important to mention the legend meaning. The colors will depend on the height, and the numbers represent a height too, but respect to the minimum and maximum values selected when taking the 3D image. That is, if the bottom part is taken too low, the white value will seem higher than it is in reality. So it is useful to create the view but the values can't be directly treated. However, when computing the fracture height, as it is done by the substraction between the maximum and the minimum values, it will be independent of the accuracy with which the selection of the global minimum has been taken. Note that some color bars have been adjusted and don't start in zero.

Figure 22: 99.5% porosity, T_{amb} specimen.

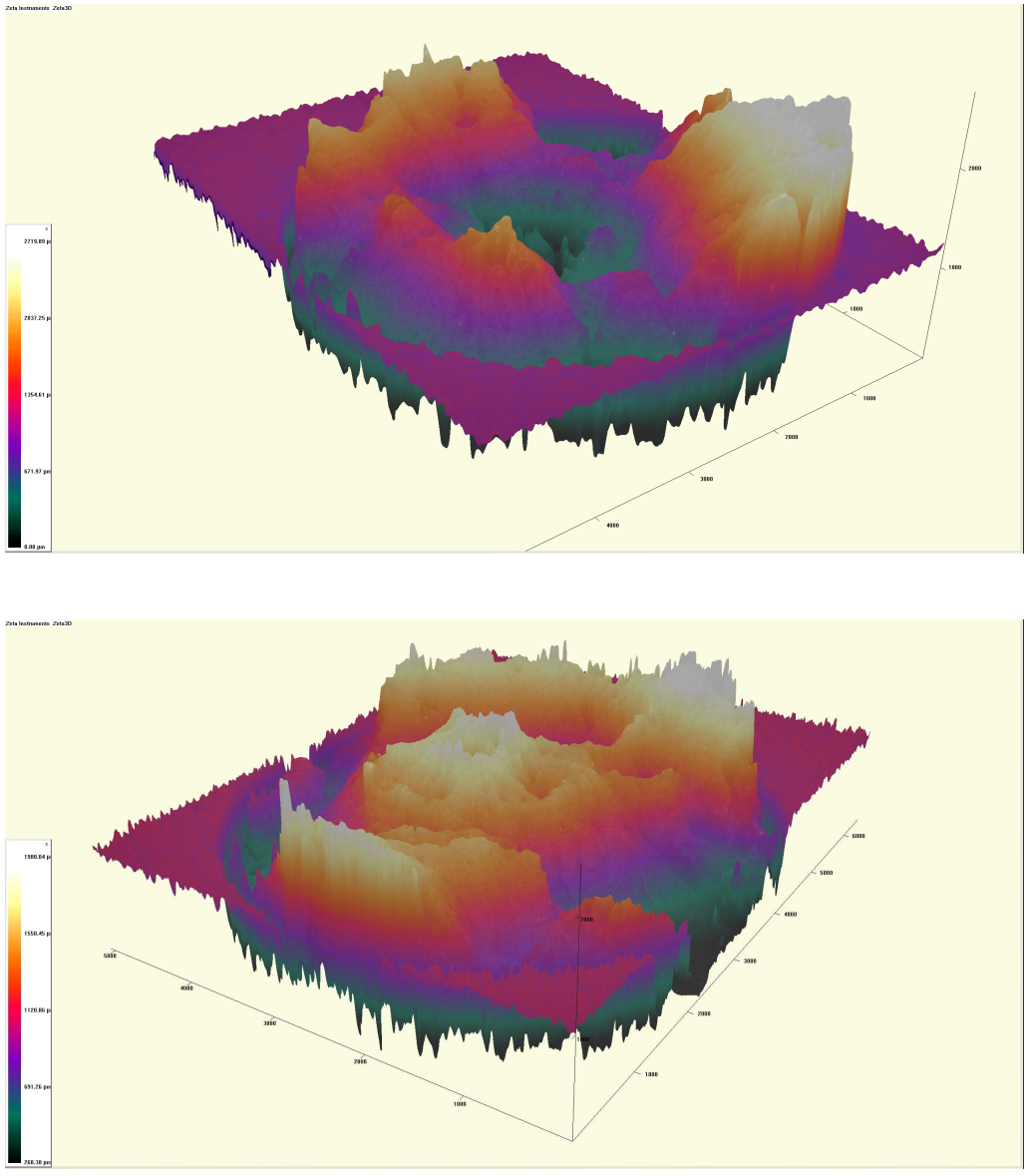

Figure 23: 3D Fracture Surface representation of a 99.5% porosity, T_{amb} specimen.

Figure 24: 99.5% porosity, 100°C specimen.

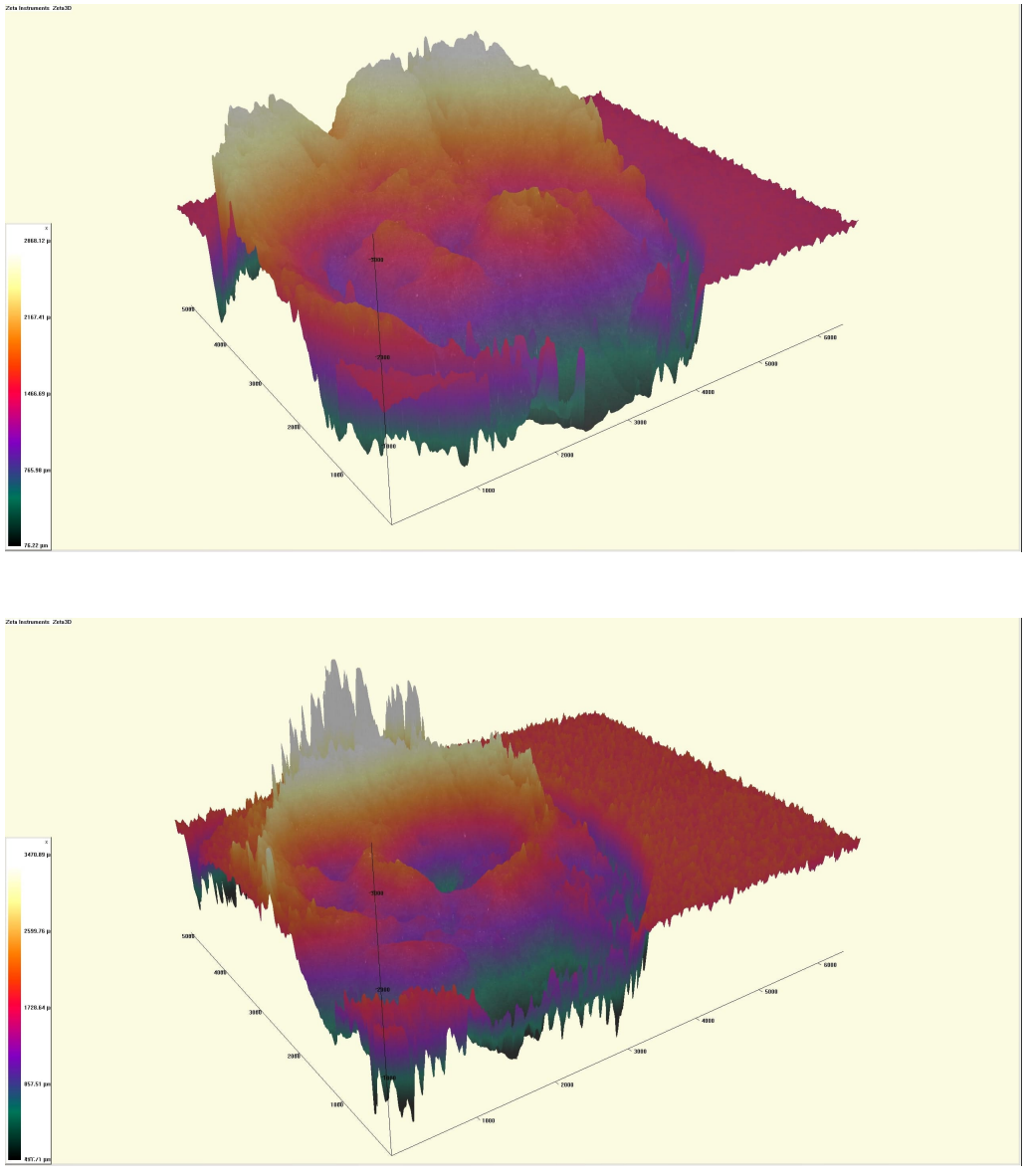

Figure 25: 3D Fracture Surface representation of a 99.5% porosity, 100°C specimen.

Figure 26: 99.5% porosity, 150°C specimen.

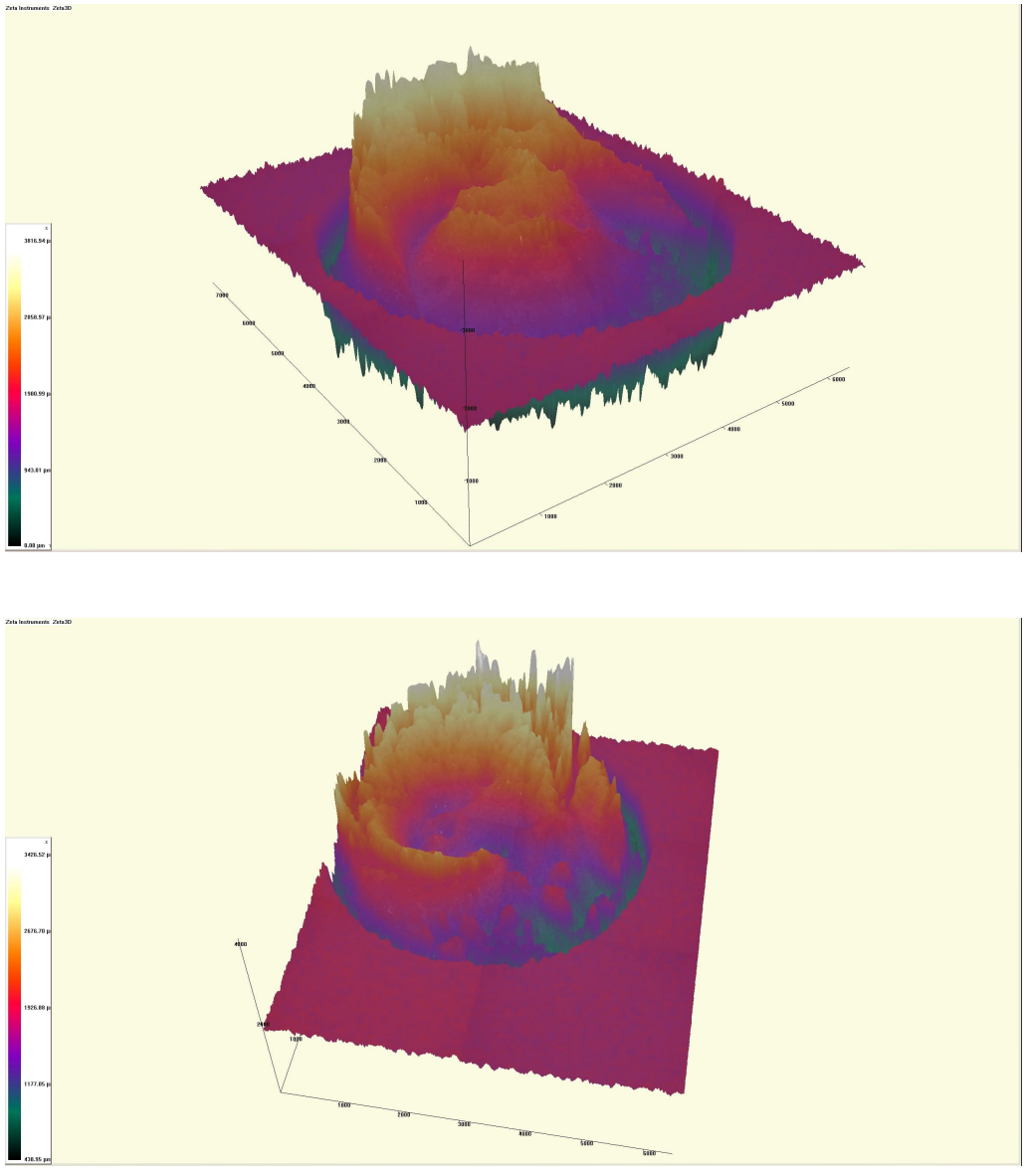

Figure 27: 3D Fracture Surface representation of a 99.5% porosity, 150°C specimen.

Figure 28: 95% porosity, T_{amb} specimen.

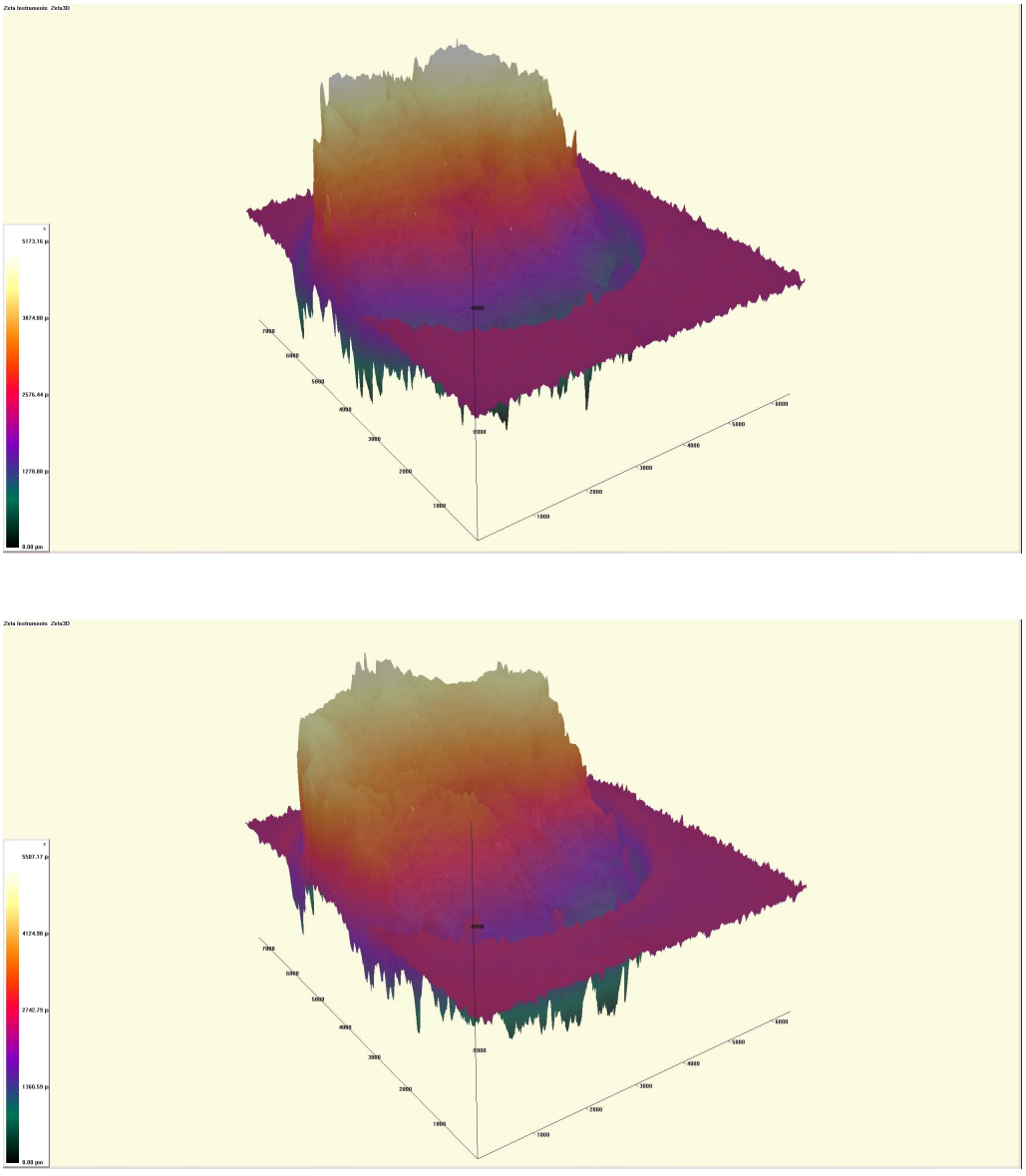

Figure 29: 3D Fracture Surface representation of a 95% porosity, T_{amb} specimen.

Figure 30: 95% porosity, 100°C specimen.

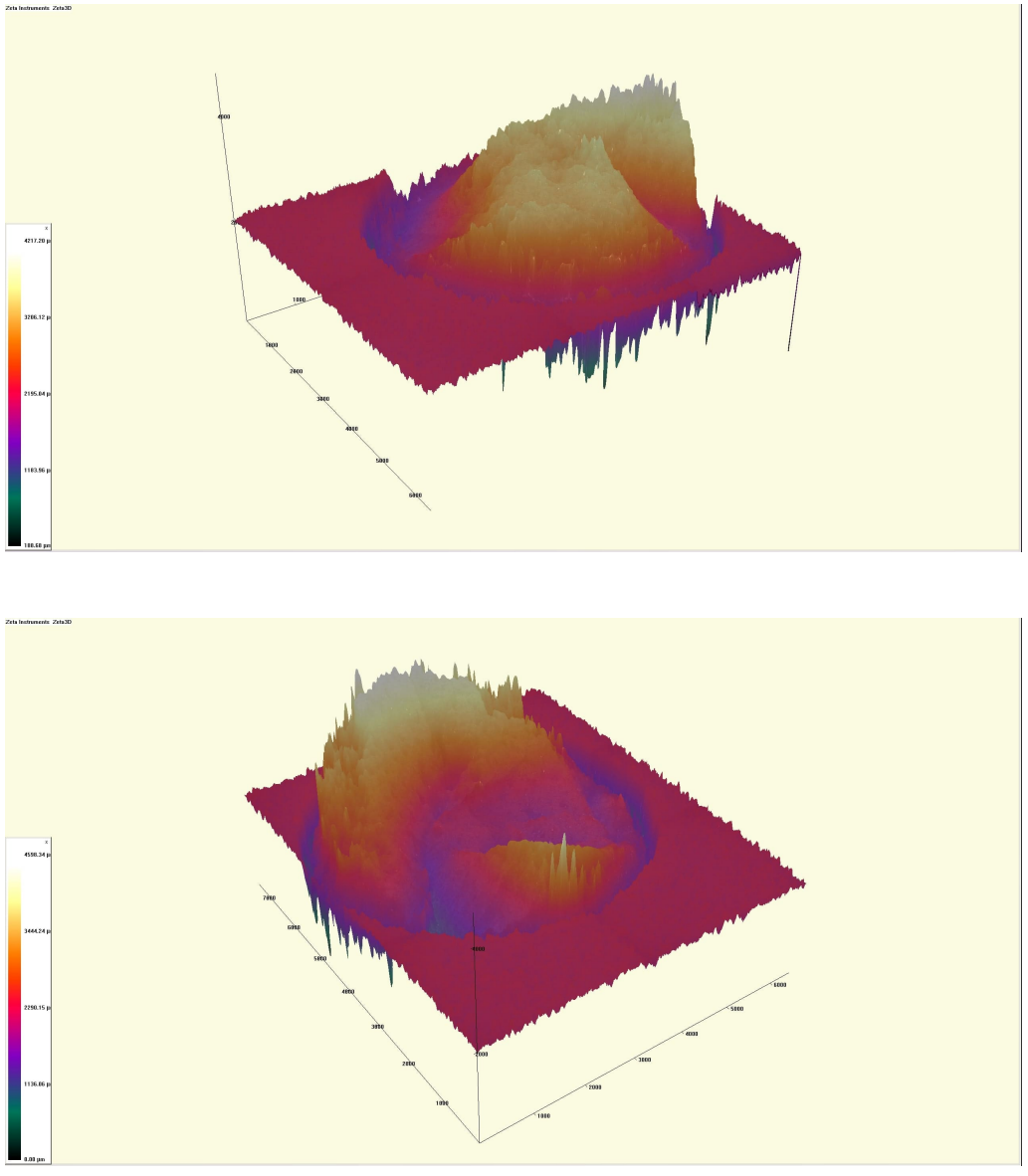

Figure 31: 3D Fracture Surface representation of a 95% porosity, 100°C specimen.

Figure 32: 95% porosity, 150°C specimen.

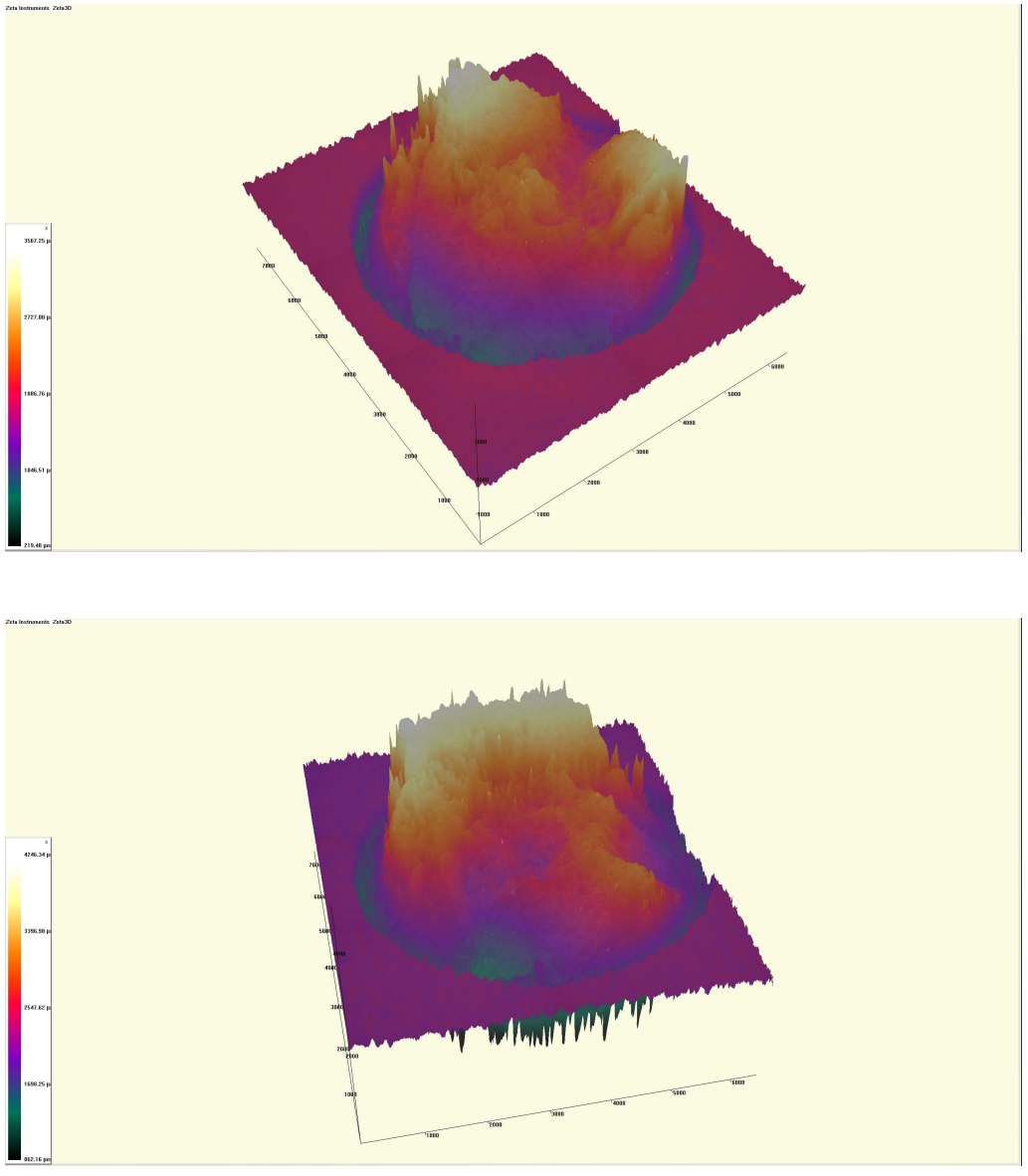

Figure 33: 3D Fracture Surface representation of a 95% porosity, 150°C specimen.

After the pictures presentation, the values obtained for the maximum fracture height are shown in the following table. Just one measure per specimen has been taken, as the heights must be equal. Possible mismatches are due to the friction and erosion when the different pieces touch each other, if speaking of a few microns disparities. A graph displaying the variation of those values as a function on the temperature has been added too.

99.5%	**Fracture height** [μm]	**95%**	**Fracture height** [μm]
T_{amb}	2085.27	T_{amb}	2184.45
100°C	2856.10	**100°C**	2937.65
150°C	3194.74	**150°C**	3243.07

Table 7: Fracture height.

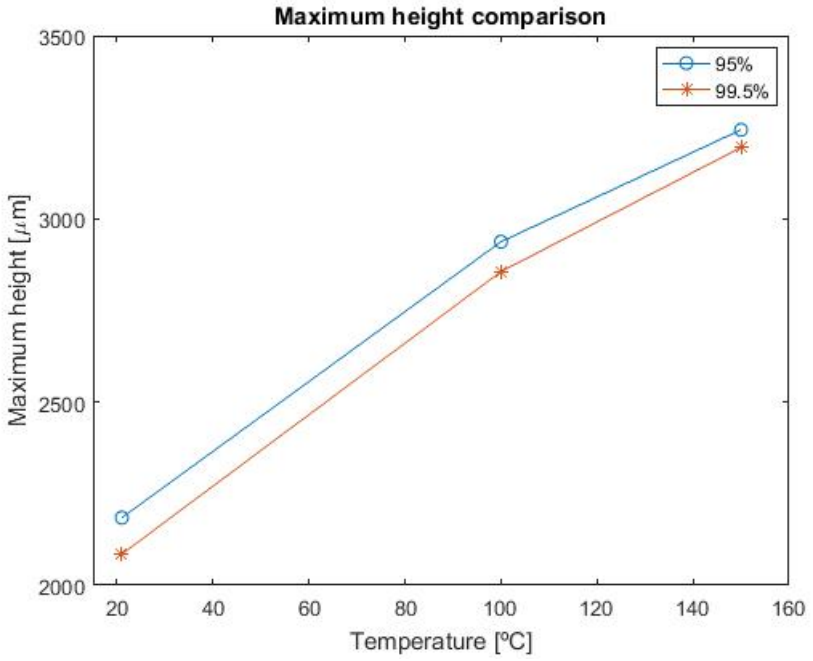

Figure 34: Maximum fracture height as a function of temperature.

6.3 Pores

Within these lines some pores are going to be further examined. Pores from all the specimens have been inspected, and information such as it diameter, depth or volume has been extracted.

Finding a path for these pores regarding the porosity or temperature is quite difficult, as examining just one isolated pore or one group of them per specimen does not give enough information to state that every pore is going to be that big or with such geometry. For that intention, a high number of pores should be inspected from each specimen, and even the location where they are located can be a factor that changes its nature, so it must be taken into account.

Also, guessing the pore that have caused the fracture is impossible, so interesting zones or pores that can be easily seen with the 5X augmentation have been chosen.

Hence, the intention with this section is to start checking the behavior of these defects, analyze what kind of information can be extracted and try to find any logic among all of them.

6.3.1 Pore 1

The first of the pores to be inspected belongs to the 99.5% porosity, T_{amb} specimen. Figure 35 shows the stitching made on the fracture surface, where two possible choices have been previously made. Finally, the one on the right has been picked, located at approximately the border of the piece. The 3D figure below can help with the observation of an almost spherical shape.

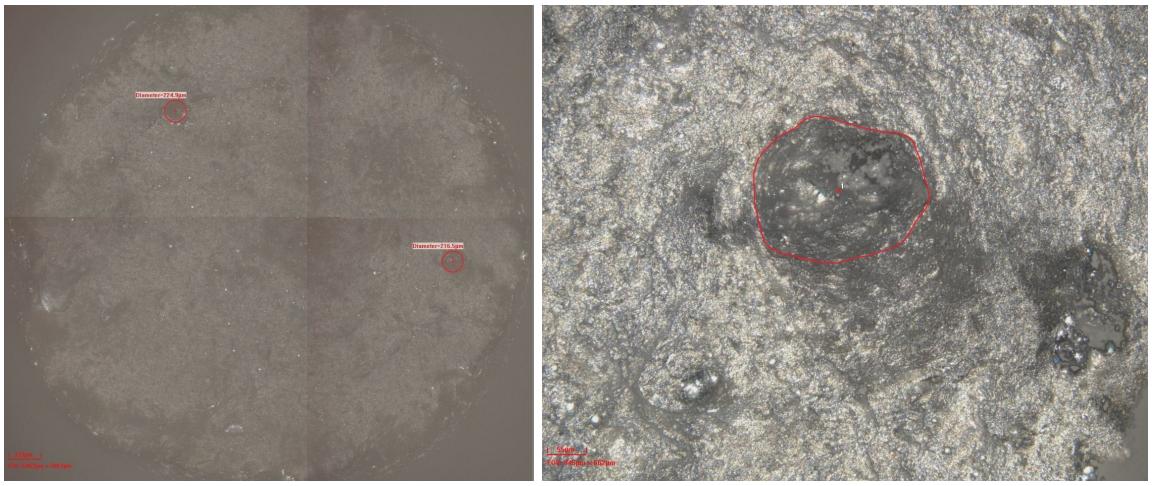

Figure 35: 2D Pore on a 99.5% porosity, T_{amb} specimen. On the left, whole fracture surface image with two selected pores; on the right, pore on the right amplified at 20X and surrounded.

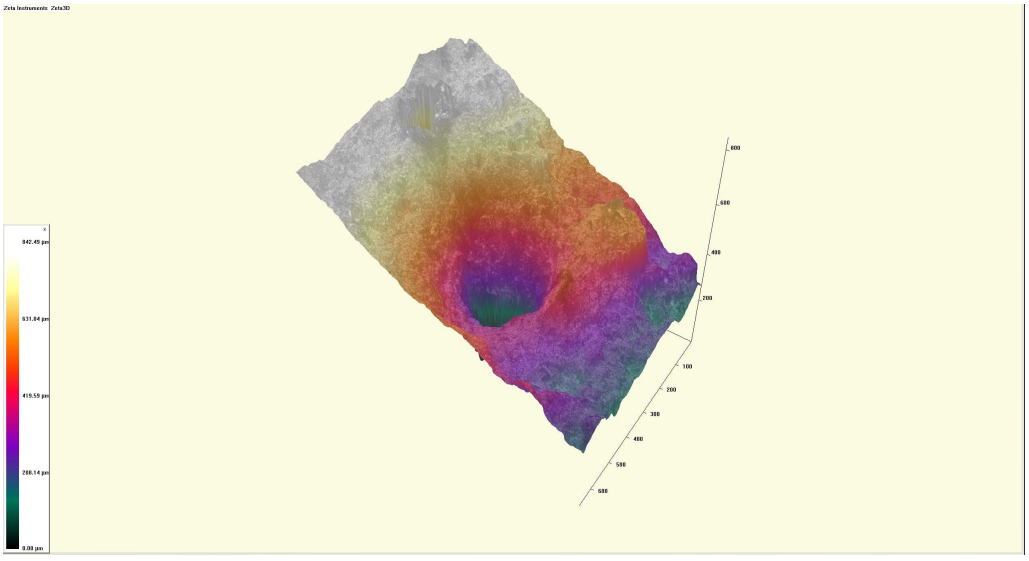

Figure 36: 3D Pore representation of a 99.5% porosity, T_{amb} specimen.

The final diameter is 225.09 μm, which does not differ much from the earlier guess on the fracture surface stitching, which was 216.50 μm. A 3.82% of error was made, and although it wan not a high value, it is a good practice to try to observe the pore amplified to take more accurate measurements.

Diameter [μm]	**Depth** [μm]	**Area** [μm^2]	**Volume** [μm^3]
225.09	438.29	39792.9	10683232.00

Table 8: Pore information of a 99.5% porosity, T_{amb} specimen.

6.3.2 Pore 2

This second pore does not longer belong to the T_{amb} specimen but to the 100°C of temperature. The zone where the pore is placed can be seen in Figure 37, surrounded with a red circle.

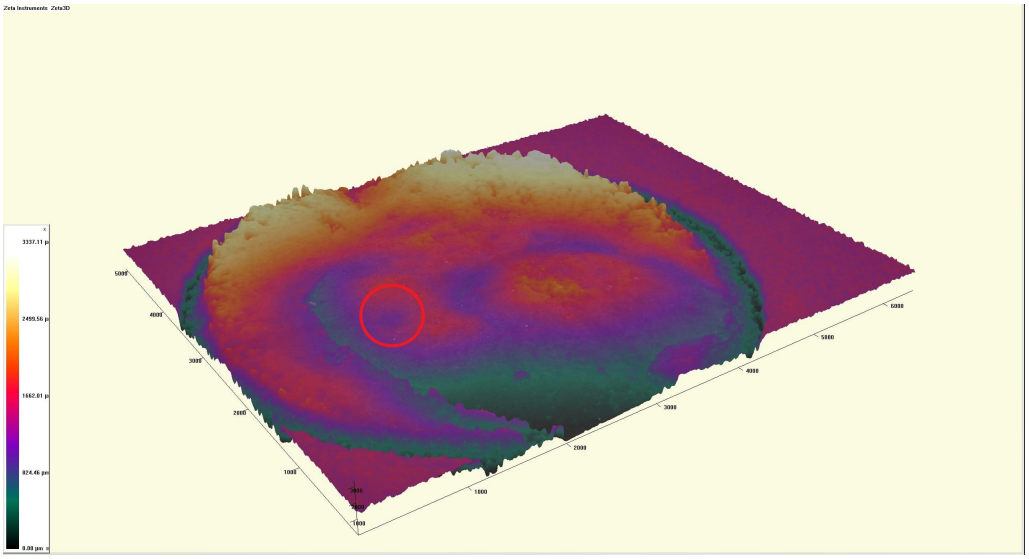

Figure 37: Pore zone selection from fracture surface of a 99.5% porosity, 100°C specimen.

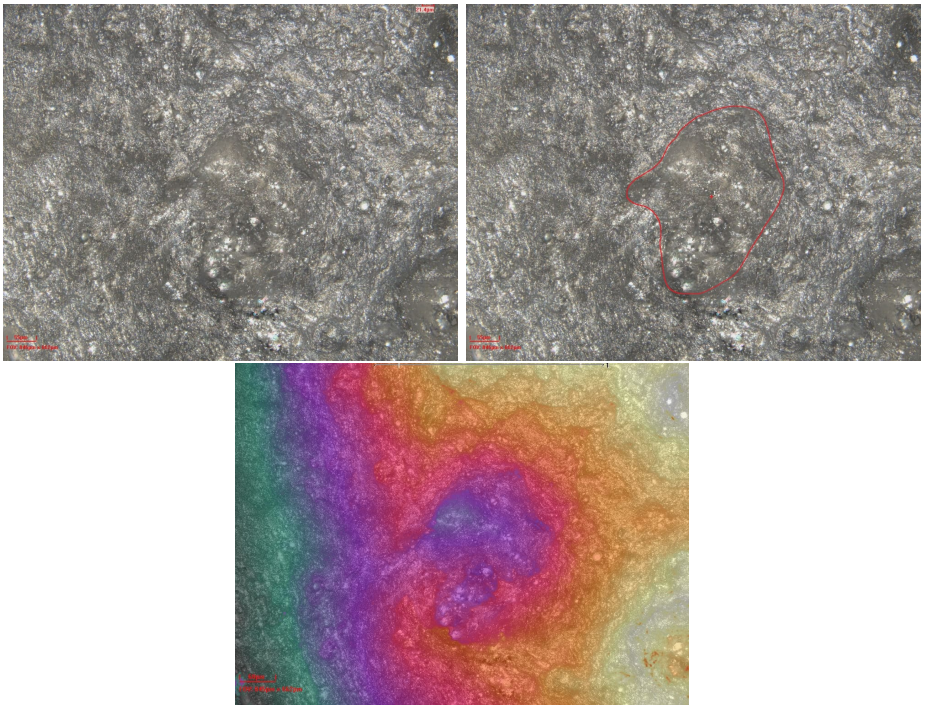

Figure 38: 2D Pore on a 99.5% porosity, 100°C specimen and 20X augmentation. From left to right and top to bottom, real color surface; surrounded pore; colored surface.

Both false and real color are brought together with the pore margins as a way of showing how those margins have been set. Without the false color representation it is hopeless to try to imagine the shape of the pore. Even though there are some times where the light hits the bottom part of the pore and a sparkle can be seen, it does not always happen and there will still be troubles with how big it is.

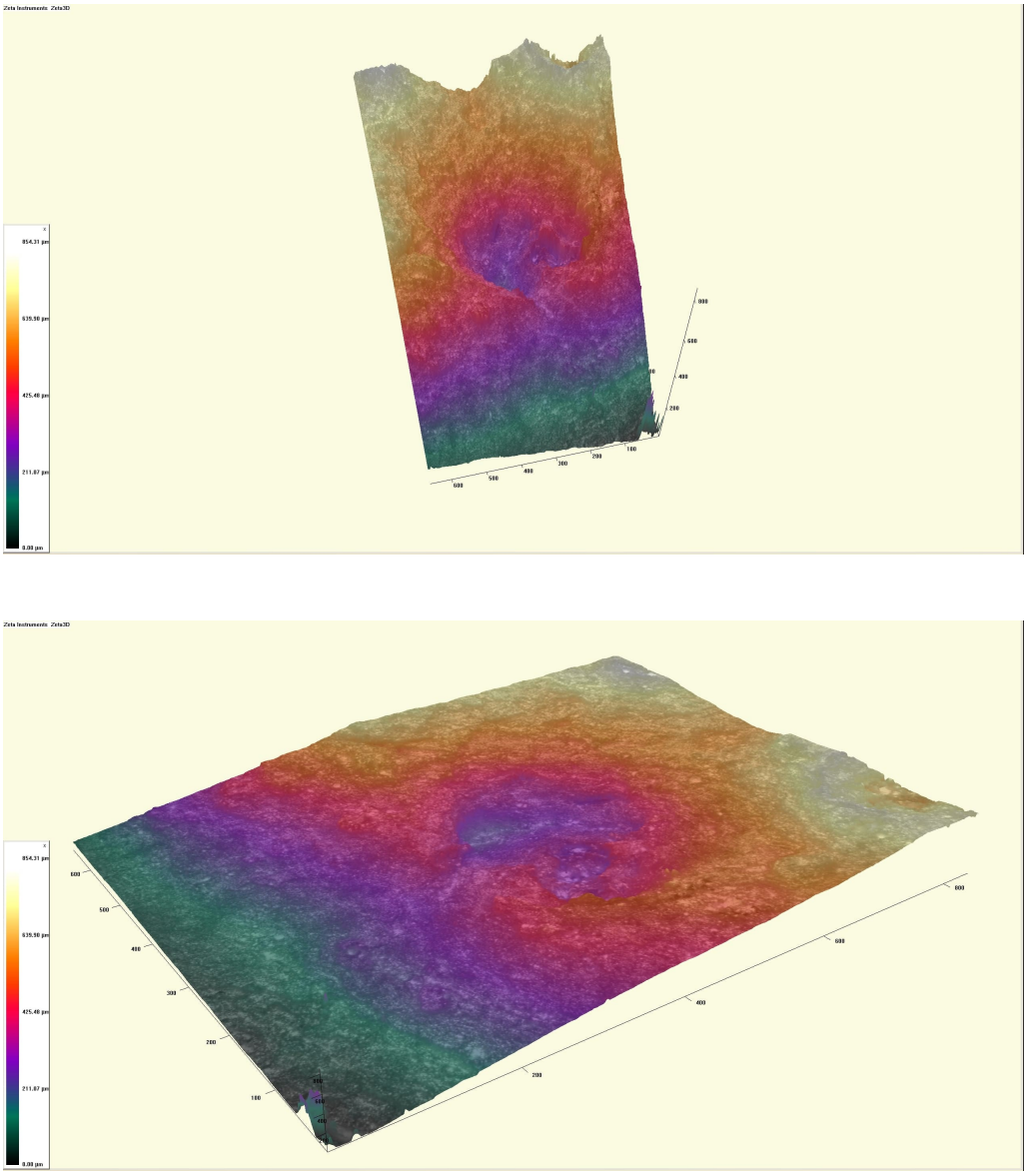

Figure 39: 3D Pore representation of a 99.5% porosity, 100°C specimen. On the top, 1:1 scaled image; on the bottom, crushed image.

As this pore is small enough with the 20X augmentation, and with a naked eye it does not present a clear shape, it has been inspected with the 50X objective too. Now, what could have previously been thought as a big quasi spherical pore is clarified, and a coalescence of small pores is seen. The combination of four pores or group of pores forms the big one. Even some of these groups seem to be composed of another coalescence of voids, but taking measurements of each and every one of them is a hard task, so regrouping is preferred. Group number 2 is an example of this feature.

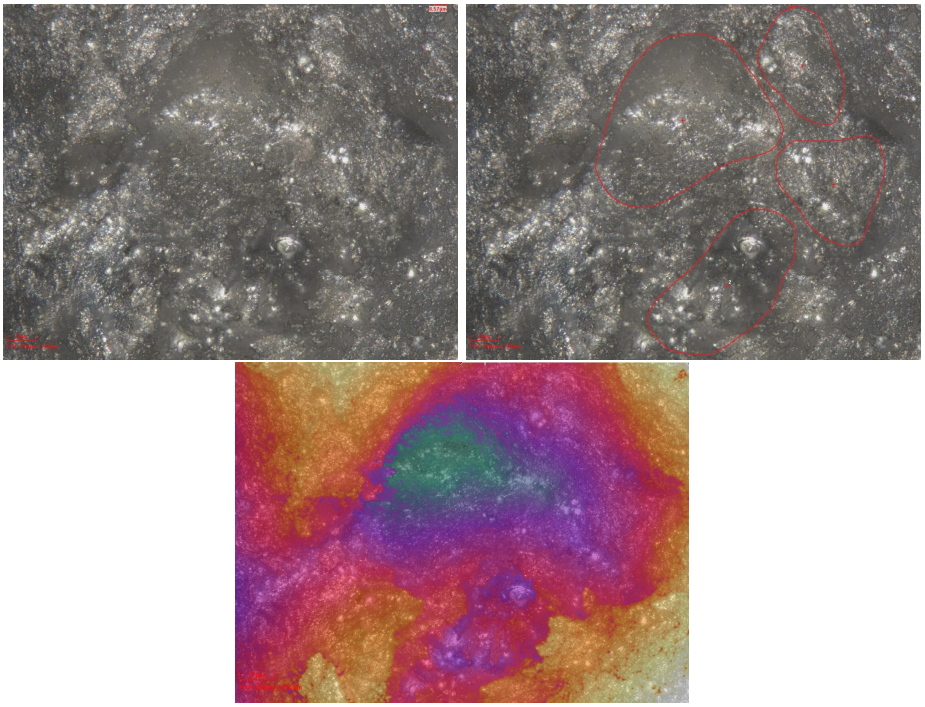

Figure 40: 2D Pore on a 99.5% porosity, 100°C specimen and 50X augmentation. From left to right, real color surface; surrounded pore; colored surface.

The information retrieved is shown in the following table, with a numeration of the pores corresponding with the one of the previous figure. The volume that was calculated from the 20X augmentation is not shown in the table, but has a value of 22700294.00 μm^3. Making the sum of all of the volumes it can be found that the total volume is 3113939.60 μm^3, which gives an error of 86.28%. Clearly, a much smaller pore margins were selected, as this formation was unknown.

Number	**Diameter** [μm]	**Depth** [μm]	**Area** [μm^2]	**Volume** [μm^3]
1	123.86	158.75	12049.6	976779.9
2	96.09	113.19	7251.7	1020590.4
3	78.99	-	4901.09	609617.1
4	70.74	-	3930.1	506952.2

Table 9: Pores information of a 99.5% porosity, 100°C specimen.

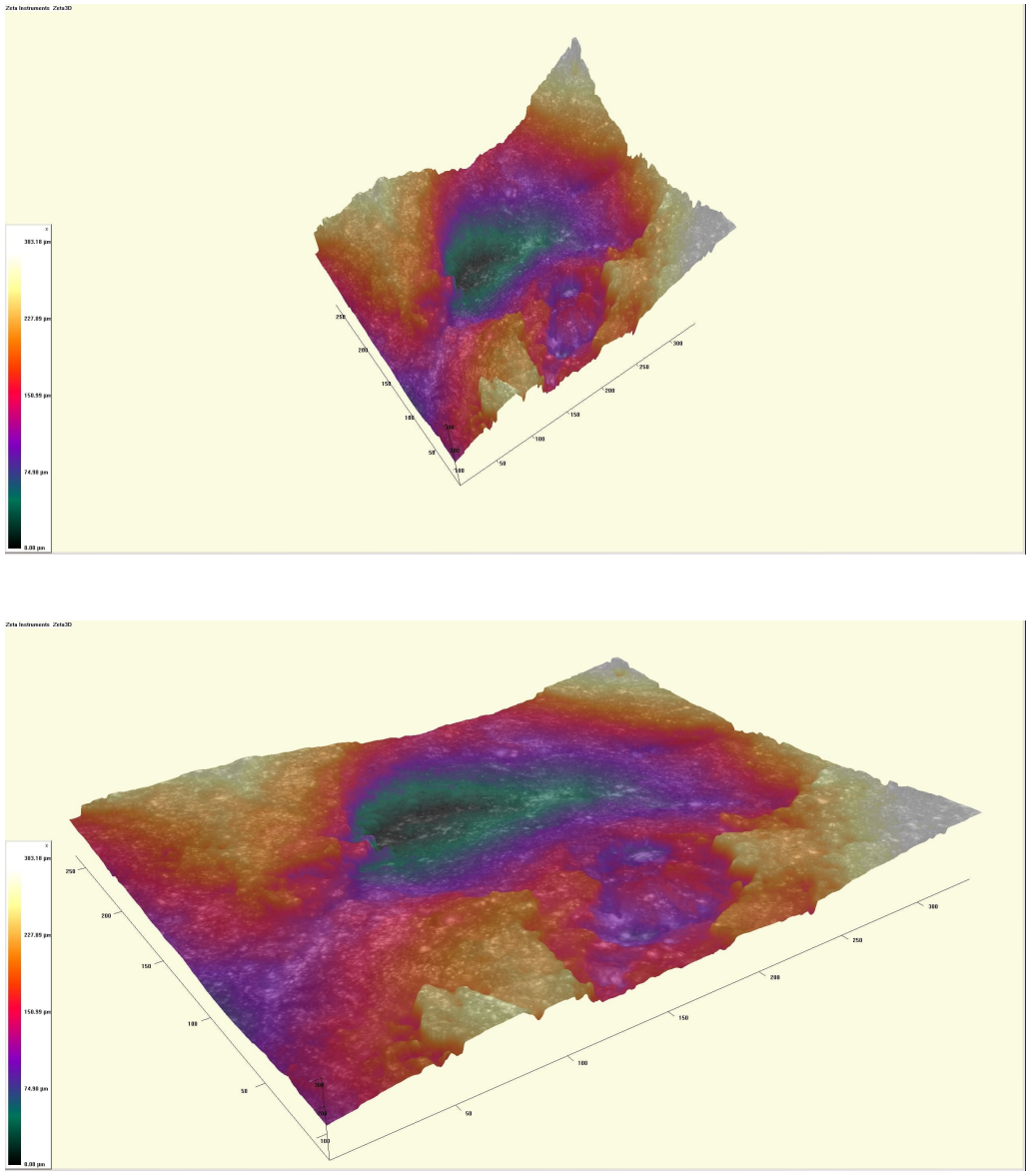

Figure 41: 3D Pore representation of a 99.5% porosity, 100°C specimen. On the top, 1:1 scaled image; on the bottom, crushed image.

6.3.3 Pore 3

The third pore to be analyzed corresponds to a 99.5% porosity, 100°C specimen. The location is rather random, as does not coincide with the highest or the lowest part of the fracture surface. A possible coalescence of pores is observed again, now with much more pronounced rounded shapes. The table at the end of the page includes the information of the five of them. Actually, it is not absolutely clear to be a coalescence of pores, and a further analysis and higher augmentations would be needed.

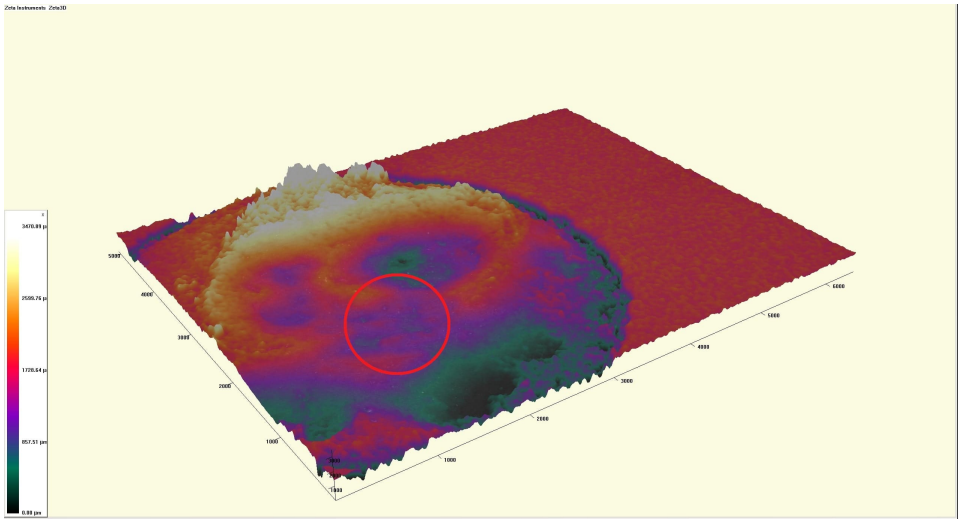

Figure 42: Pore zone selection from fracture surface of a 99.5% porosity, 100°C specimen.

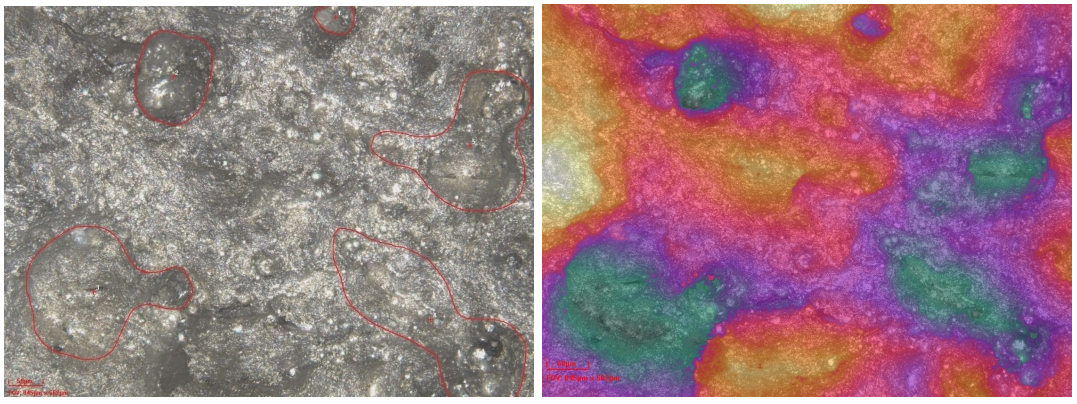

Figure 43: 2D Pore on a 99.5% porosity, 100°C specimen and 20X augmentation. On the left, surrounded pores; on the right, colored surface.

In this previous figures, small voids can be observed as the sparkles that were commented before. On Figure 44, the 3D representation shows it too.

Number	**Diameter** $[\mu m]$	**Depth** $[\mu m]$	**Area** $[\mu m^2]$	**Volume** $[\mu m^3]$
1	59.11	-	2743.76	656809.1
2	137.69	255.54	14890.5	2126422.8
3	210.01	174.18	34639.6	3811666.25
4	228.93	267.67	41160.3	5794766.00
5	203.68	214.36	32583.3	4940008.50

Table 10: Pores information of a 99.5% porosity, 100°C specimen.

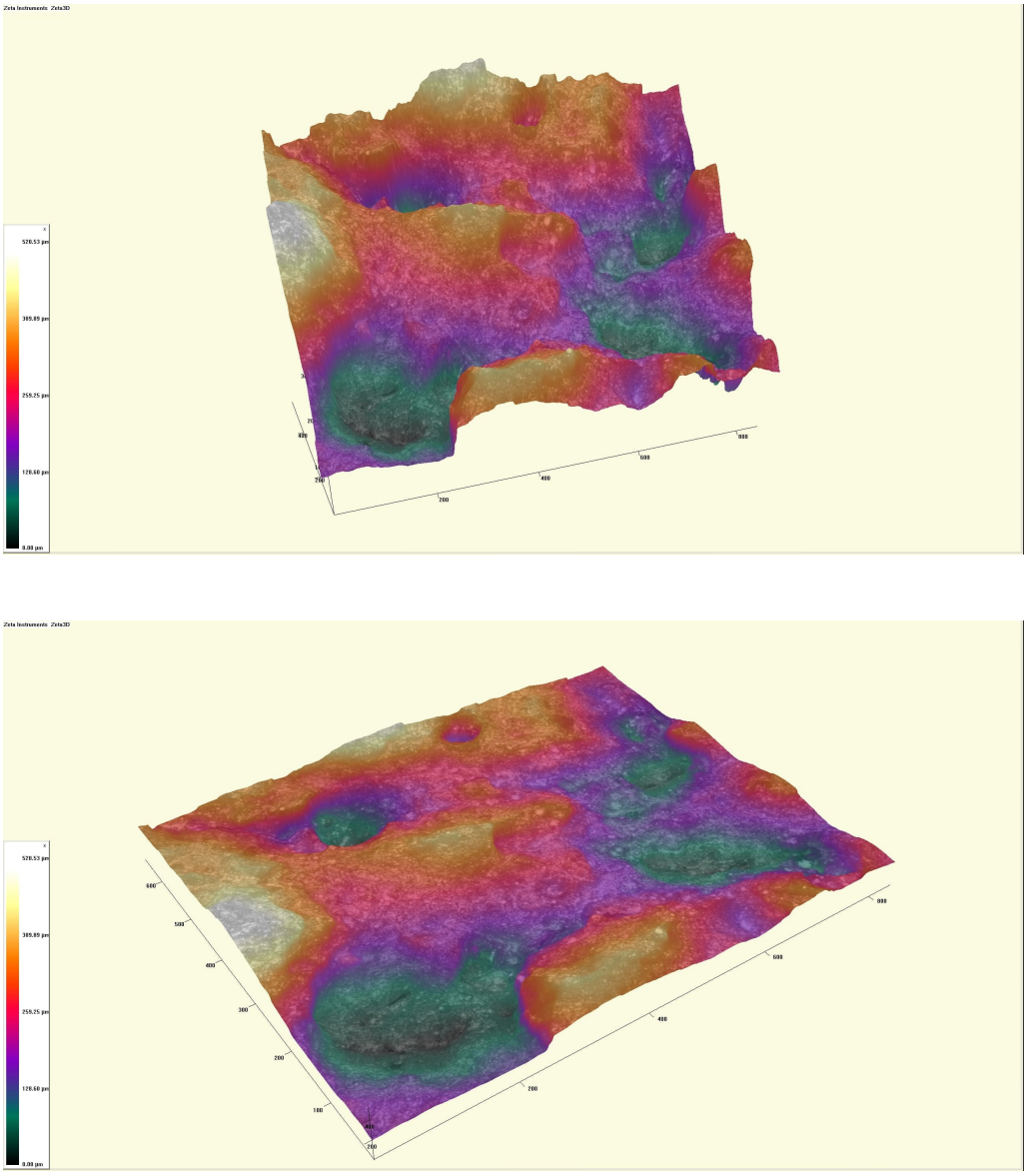

Figure 44: 3D Pore representation of a 99.5% porosity, 100°C specimen. On the top, 1:1 scaled image; on the bottom, crushed image.

6.3.4 Pore 4

The fourth pore location is quite interesting as it is situated at the end of a crack that takes more than a half of the fracture surface. It is part of a 99.5% porosity, 150°C specimen and has a big spherical shape that can be seen from the 5X stitching.

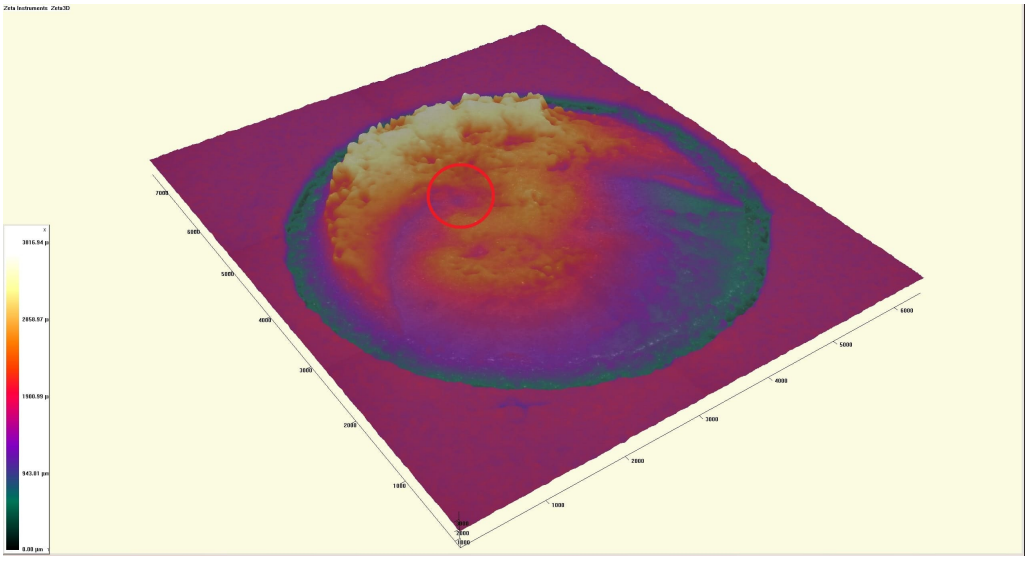

Figure 45: Pore zone selection from fracture surface of a 99.5% porosity, 150°C specimen.

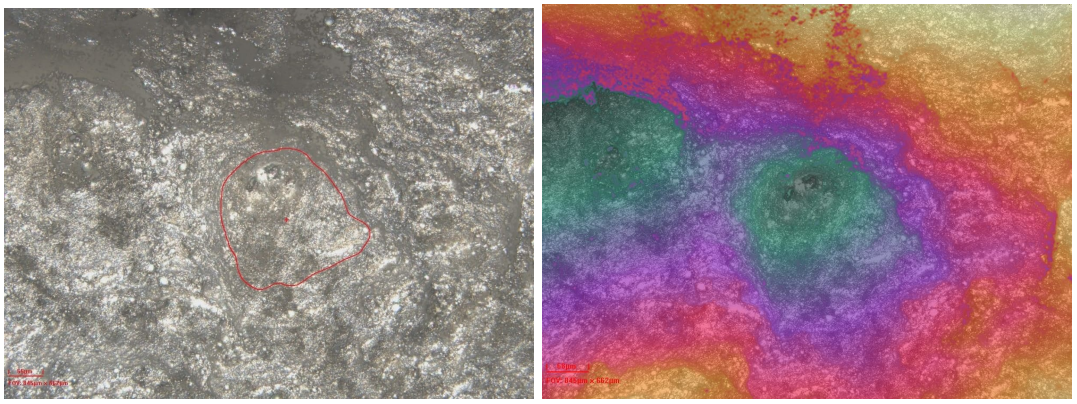

Figure 46: 2D Pore on a 99.5% porosity, 150°C specimen and 20X augmentation. On the left, surrounded pore; on the right, colored surface.

Diameter [μm]	**Depth** [μm]	**Area** [μm^2]	**Volume** [μm^3]
218.70	329.15	37565.7	6413499.00

Table 11: Pores information of a 99.5% porosity, 150°C specimen.

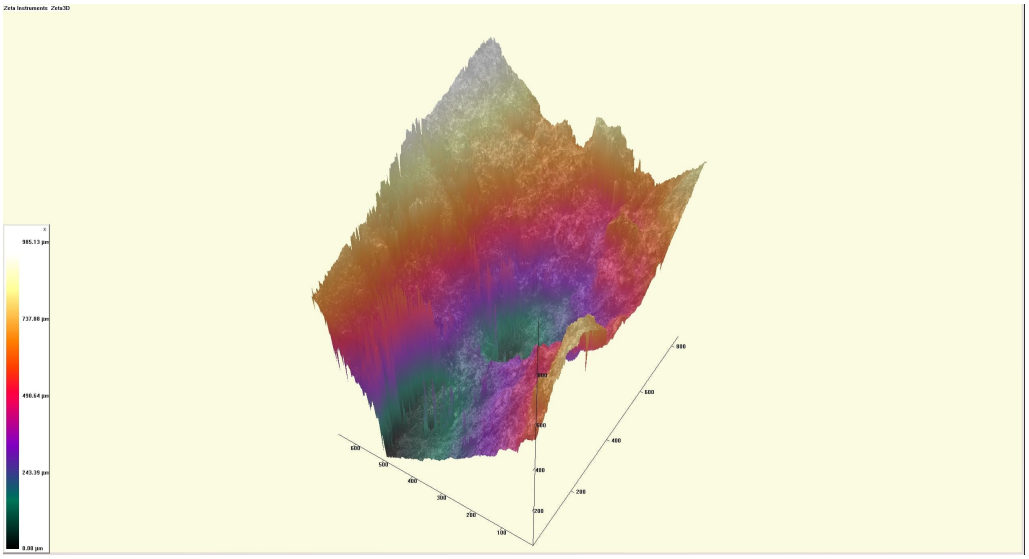

Figure 47: 3D Pore representation of a 99.5% porosity, 100°C specimen.

6.3.5 Pore 5

Changing to the 95% porosity, next pore is retrieved from the T_{amb} piece, that has an inclined fracture surface. The selected pore is located in the center of the specimen. This time the shape is not as spherical as other defects and follows an ellipsoidal geometry. Anyways, an imaginary diameter has been computed from the area for a possible diameter comparison.

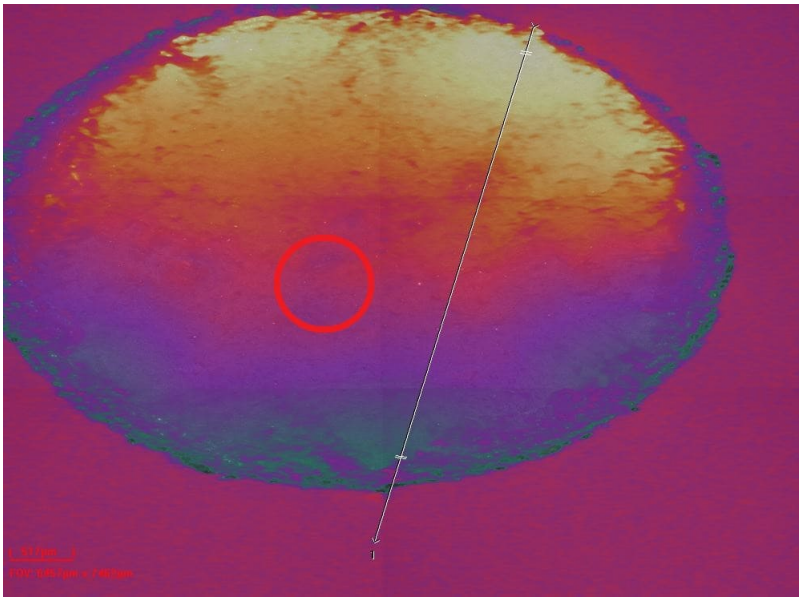

Figure 48: Pore zone selection from fracture surface of a 95% porosity, T_{amb} specimen.

Diameter $[\mu m]$	**Depth** $[\mu m]$	**Area** $[\mu m^2]$	**Volume** $[\mu m^3]$
222.00	219.17	38708.4	7770585.00

Table 12: Pore information of a 95% porosity, T_{amb} specimen.

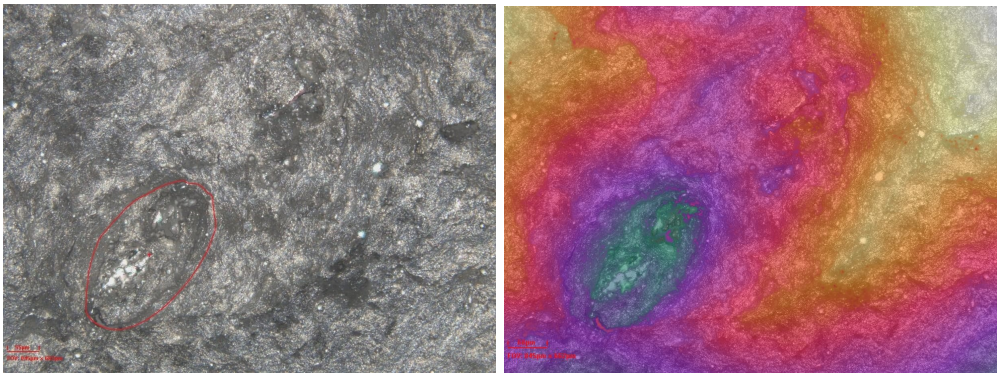

Figure 49: 2D Pore on a 95% porosity, T_{amb} specimen and 20X augmentation. On the left, surrounded pore; on the right, colored surface.

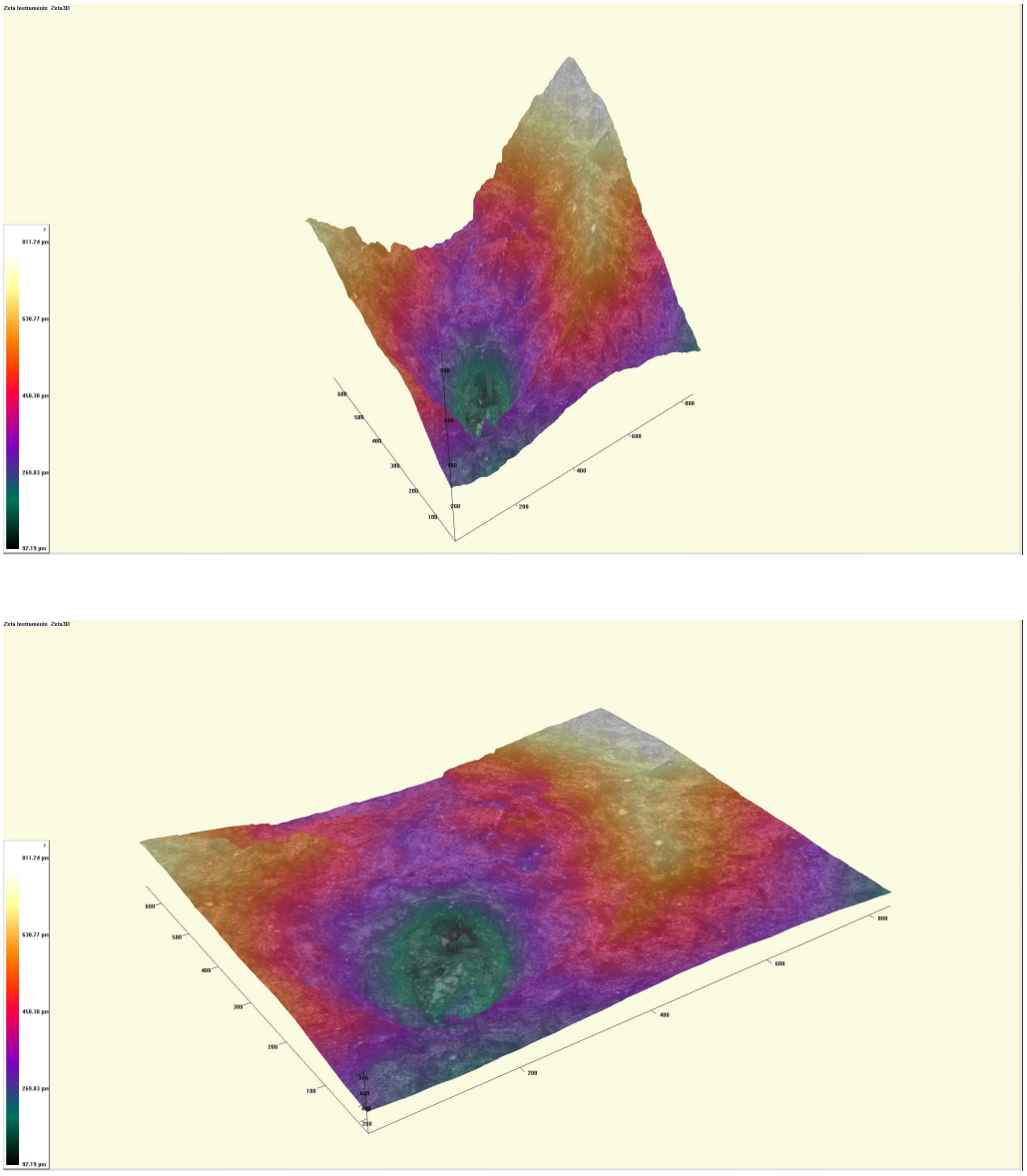

Figure 50: 3D Pore representation of a 95% porosity, T_{amb} specimen. On the top, 1:1 scaled image; on the bottom, crushed image.

6.3.6 Pore 6

This pore is inspected again from a 95% porosity, T_{amb} specimen, but now from the analogous part. The location is near the border of the fracture surface, and the shape spherical, a practically perfect sphere, in fact. The information obtained is presented in Table 13.

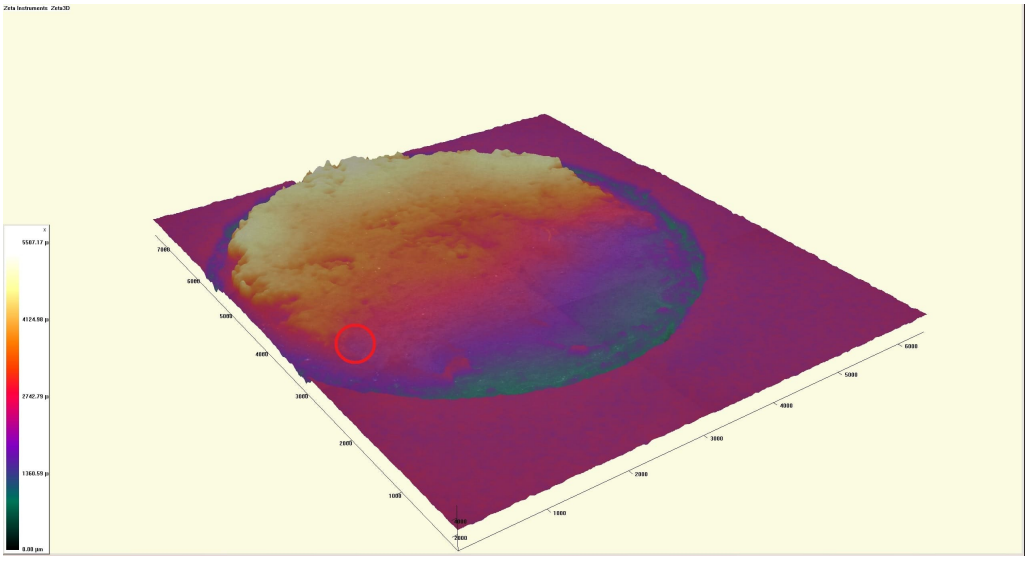

Figure 51: Pore zone selection from fracture surface of a 95% porosity, T_{amb} specimen.

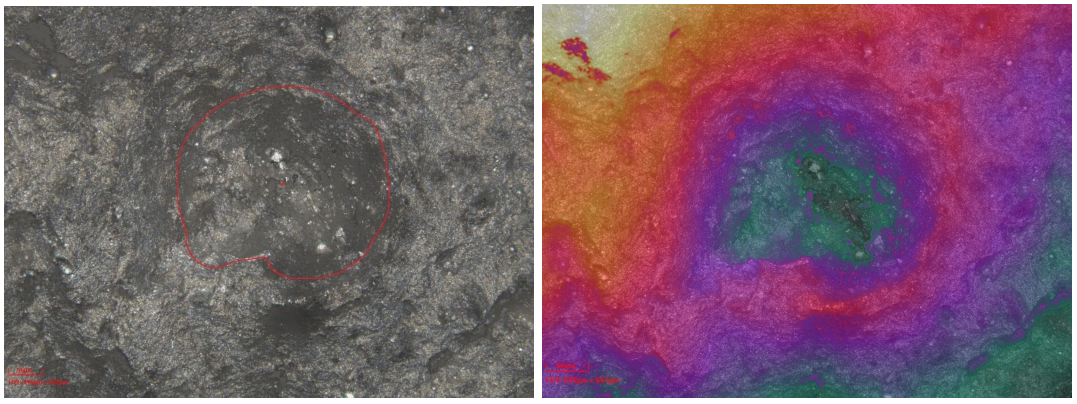

Figure 52: 2D Pore on a 95% porosity, T_{amb} specimen and 20X augmentation. On the left, surrounded pore; on the right, colored surface.

Diameter $[\mu m]$	**Depth** $[\mu m]$	**Area** $[\mu m^2]$	**Volume** $[\mu m^3]$
328.2	265.90	84599.6	17271346.00

Table 13: Pore information of a 95% porosity, T_{amb} specimen.

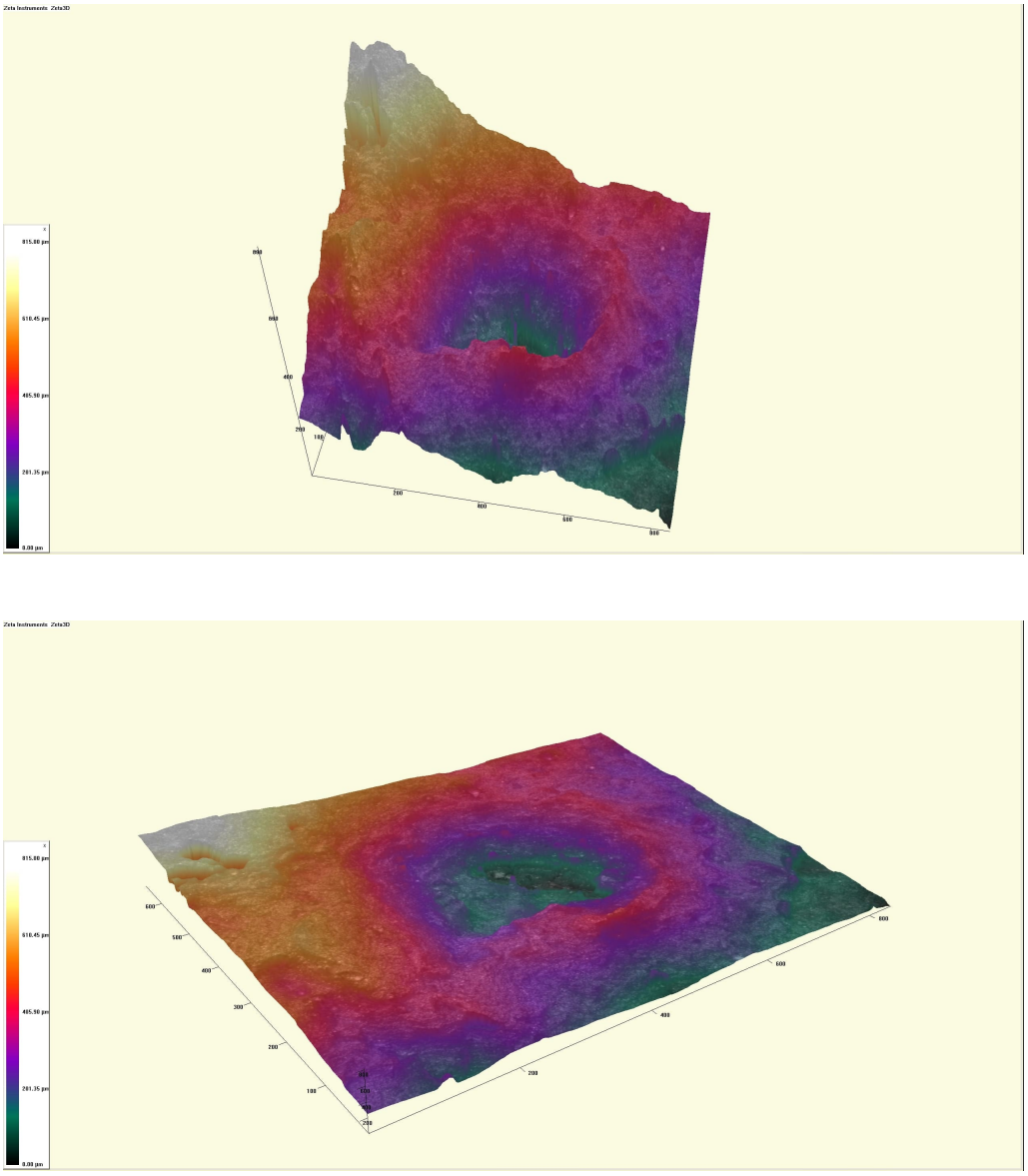

Figure 53: 3D Pore representation of a 95% porosity, T_{amb} specimen. On the top, 1:1 scaled image; on the bottom, crushed image.

6.3.7 Pore 7

This group of pores is part of the 95% porosity, 100°C specimen. Its location does not seem to be remarkable but for the fact that it belongs to one of the lowest parts of the fracture surface. What attracts the most attention is the position of these pores with respect to each other, as three of them are equally spaced, joined by an imaginary line.

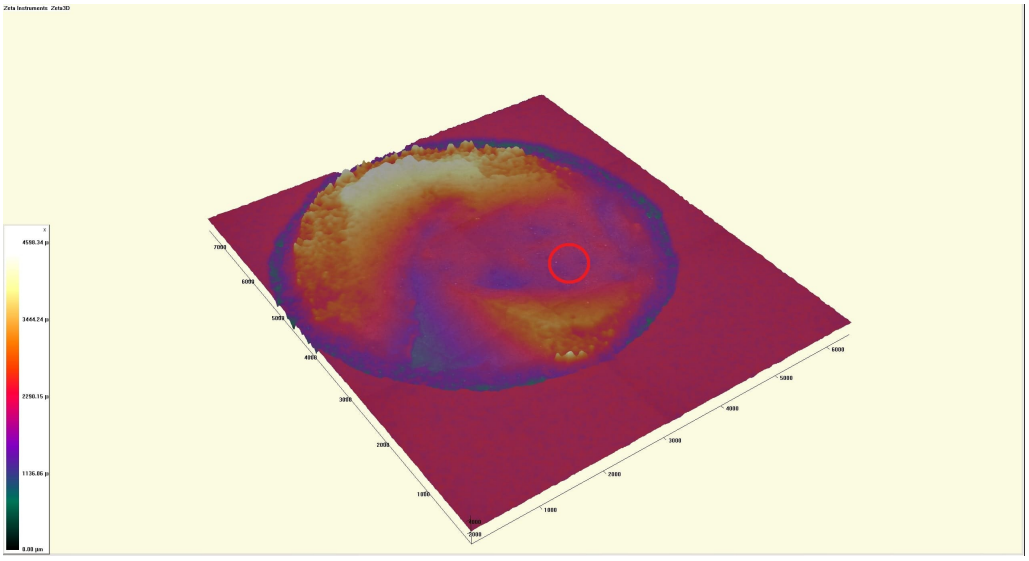

Figure 54: Pore zone selection from fracture surface of a 95% porosity, 100°C specimen.

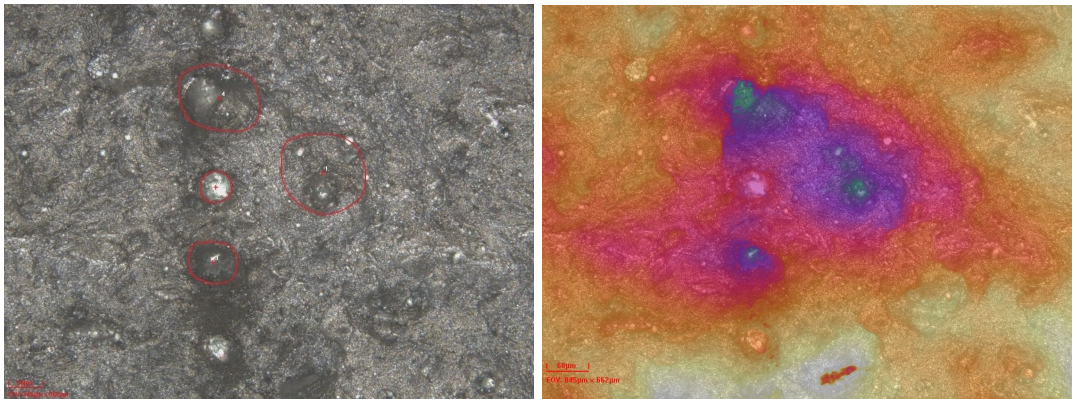

Figure 55: 2D Pores on a 95% porosity, 100°C specimen and 20X augmentation. On the left, surrounded pores; on the right, colored surface.

Number	**Diameter** $[\mu m]$	**Depth** $[\mu m]$	**Area** $[\mu m^2]$	**Volume** $[\mu m^3]$
1	135.10	-	14334.9	2637718.75
2	52.28	36.79	2146.73	527418.9
3	76.20	109.34	4560.6	989283.4
4	121.24	197.35	11545.4	2238679.50

Table 14: Pore information of a 95% porosity, 100°C specimen.

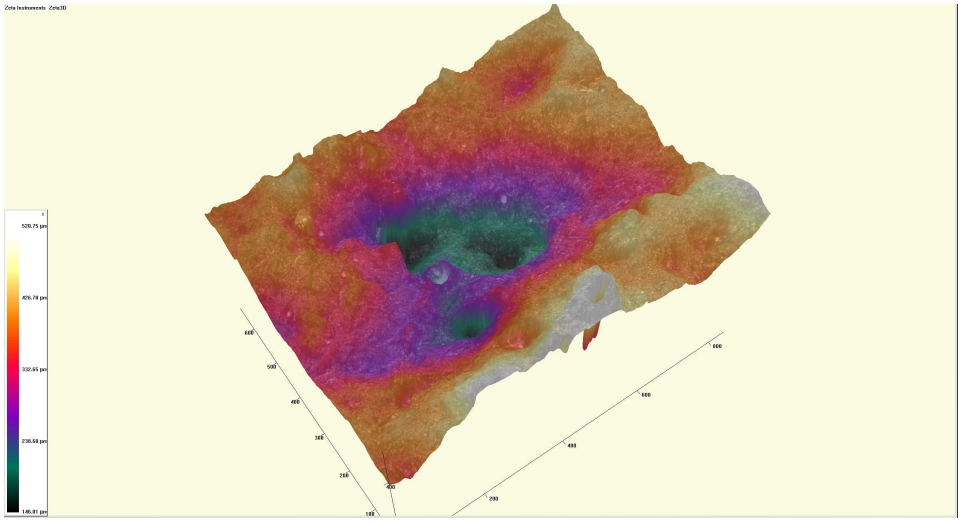

Figure 56: 3D Pore representation of a 95% porosity, 100°C specimen.

6.3.8 Pore 8

The last two group of pores to be inspected are from a 95% porosity, 150°C specimen, each of them from one of the two parts of the breakage. This time, the whole set of pores has been divided into seven small ones, which have come together to form the big one and maybe cause the fracture.

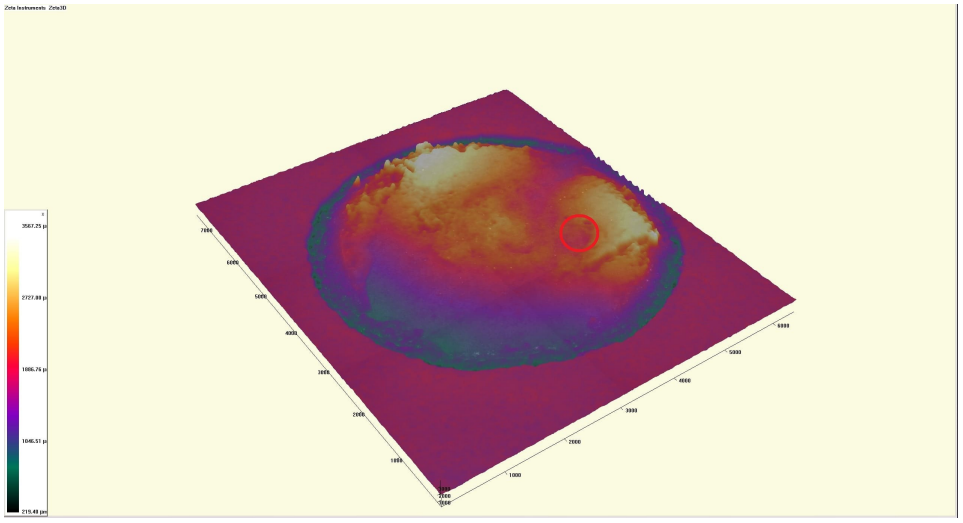

Figure 57: Pore zone selection from fracture surface of a 95% porosity, 150°C specimen.

Number	**Diameter** $[\mu m]$	**Depth** $[\mu m]$	**Area** $[\mu m^2]$	**Volume** $[\mu m^3]$
1	140.88	165.85	15588.5	2859813.50
2	70.81	131.45	3938.3	1000364.9
3	48.10	69.91	1817.27	568390.3
4	77.86	61.44	4761.0	1254541.6
5	71.73	80.08	4041.14	1113213.1
6	93.29	95.86	6835.37	1568749.1
7	121.91	111.46	11674.4	2598402.50

Table 15: Pore information of a 95% porosity, 150°C specimen.

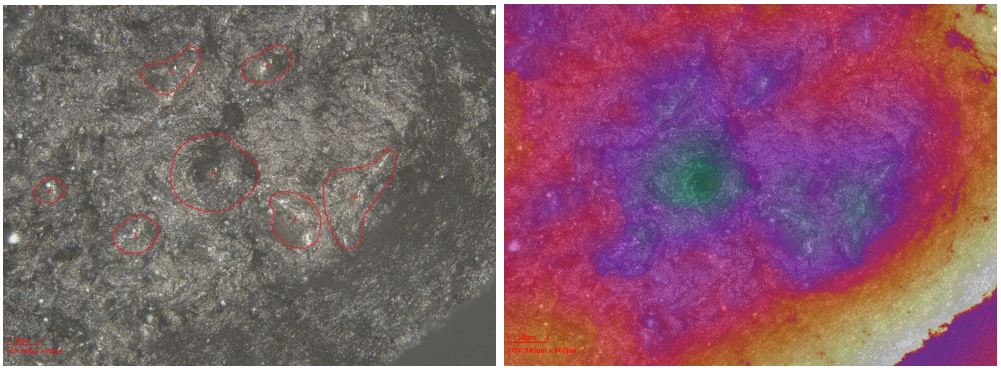

Figure 58: 2D Pore on a 95% porosity, 150°C specimen and 20X augmentation. On the left, surrounded pore; on the right, colored surface.

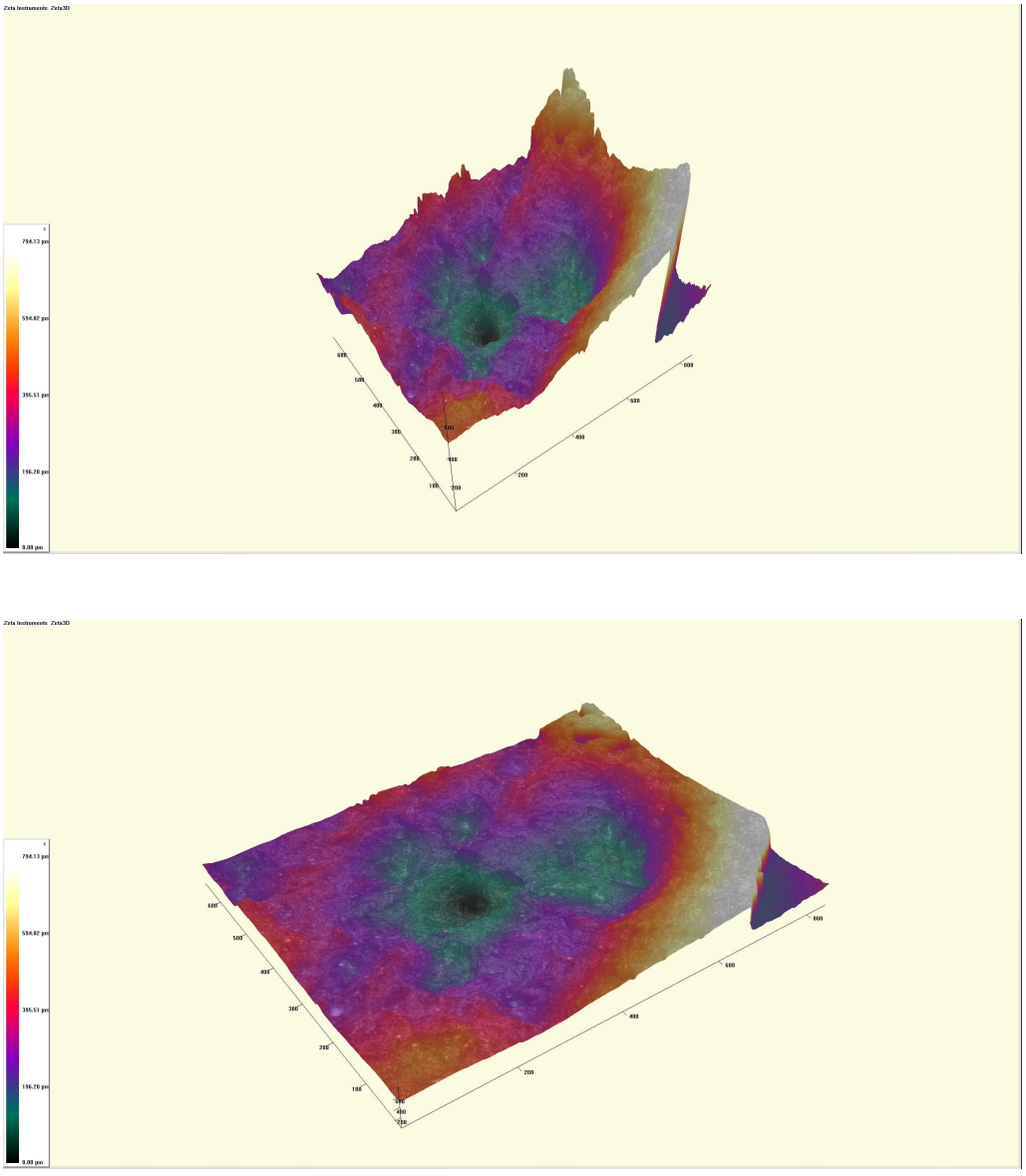

Figure 59: 3D Pore representation of a 95% porosity, 150°C specimen. On the top, 1:1 scaled image; on the bottom, crushed image.

6.3.9 Pore 9

As it has been previously explained, this last group of seven pores is part of the 95% porosity, 150°C specimen, particularly from the analogous breakage piece. Situated in the middle of the fracture surface, this combination of pores has been split into several voids, giving an idea of what could have been before the coalescence and final crack.

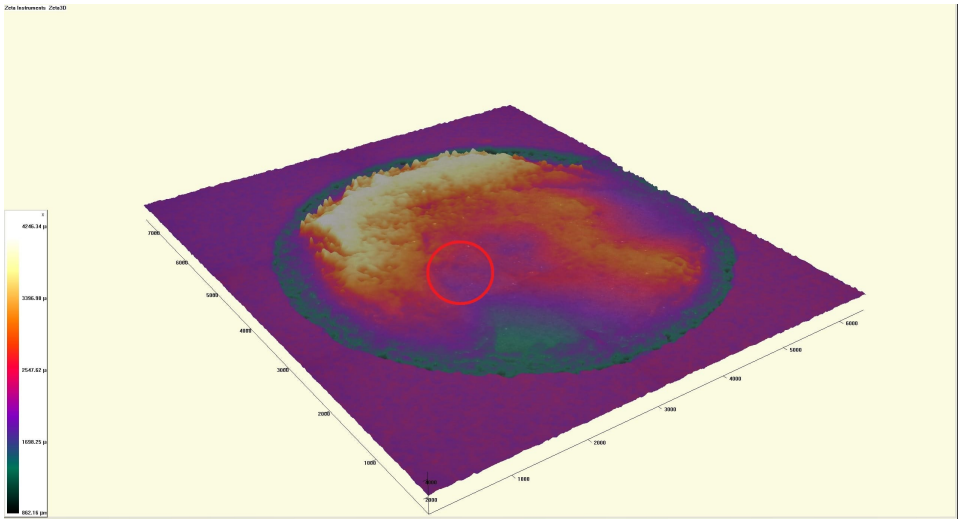

Figure 60: Pore zone selection from fracture surface of a 95% porosity, 150°C specimen.

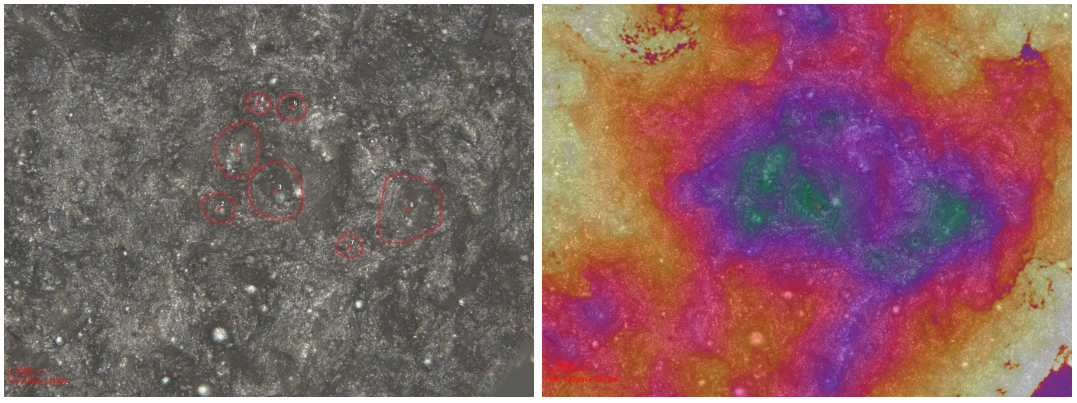

Figure 61: 2D Pore on a 95% porosity, 150°C specimen and 20X augmentation. On the left, surrounded pore; on the right, colored surface.

Number	**Diameter** [μm]	**Depth** [μm]	**Area** [μm^2]	**Volume** [μm^3]
1	80.29	82.92	5063.3	635143.6
2	52.05	77.29	2127.7	265104.2
3	90.85	123.23	6482.58	755974.9
4	37.27	58.23	1090.75	183374.4
5	46.6	40.74	1705.87	274473.9
6	107.69	118.83	9108.7	1213752.8
7	40.72	105.20	1302.13	199495.1

Table 16: Pore information of a 95% porosity, 150°C specimen.

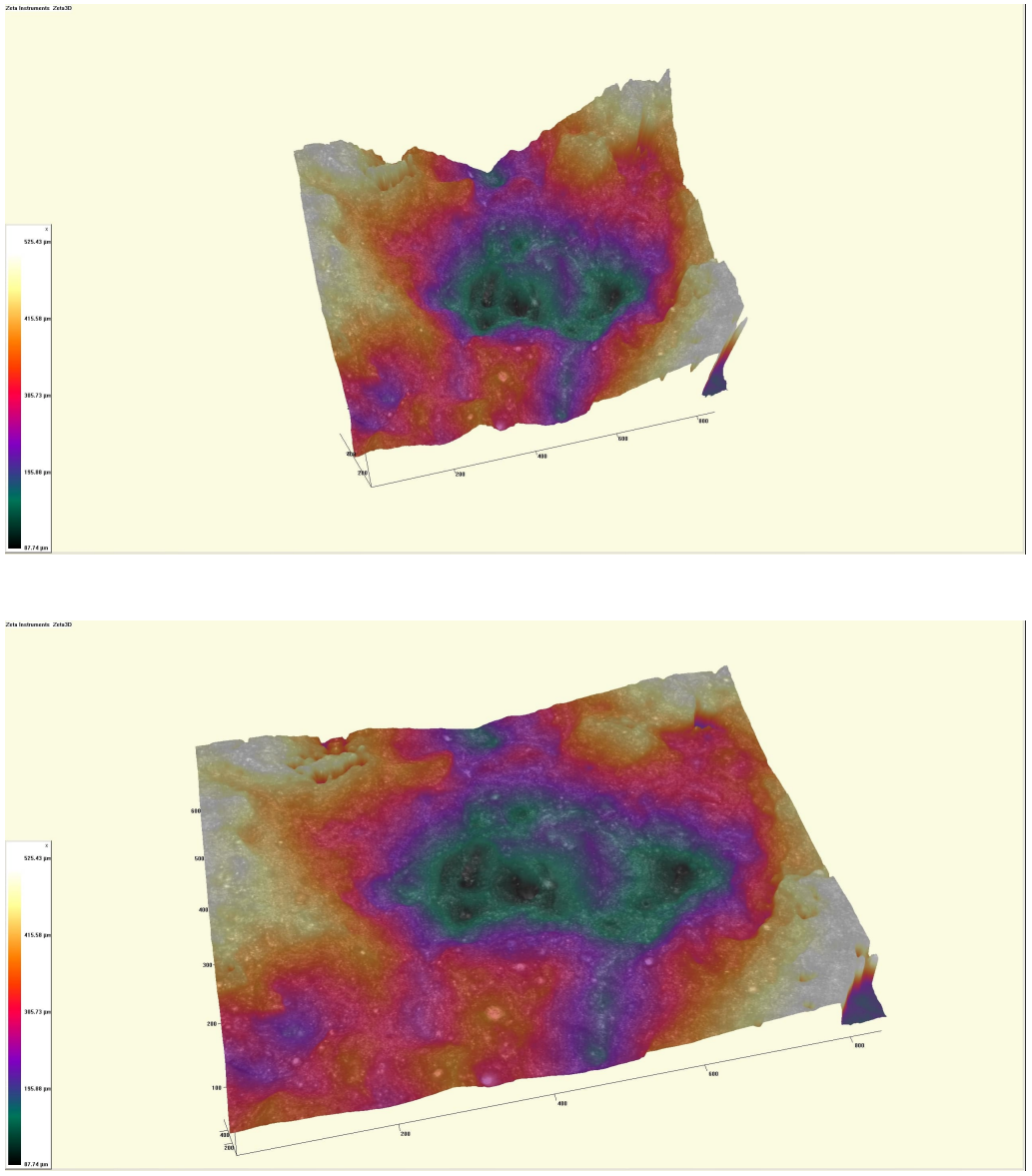

Figure 62: 3D Pore representation of a 95% porosity, 150°C specimen. On the top, 1:1 scaled image; on the bottom, crushed image.

6.4 Necking

Under ductile fracture, a phenomenon called necking is presented in the geometry of the piece. It is related to a near-instantaneous approach to total failure, which will be the time when the specimen breaks into two different pieces. As the load is carried through a testing machine, the displacement is controlled and the necking can appear. In other words, it is a reduction in the external cross-section in a fixed way [31].

The necking of the samples has been 3D represented, and its radius of curvature measured along its axial direction to see how does it changes with distance. Regarding the shape of those neckings, the big majority presents shear lip formation, with a concave and a convex part, while some suggest an asymmetric cross-sectional slip such as Figures 29 and 31, corresponding with the 95% of porosity, T_{amb} and 100°C specimens. Although this feature is part of the necking, it can be better understood in the fracture surface section as its pictures makes it clearer.

The colors will aid once again to the reconstruction of the three dimensions, with the whiter colors showing the top zones and the darker ones the bottom parts. About the measurements taken, they will not depend on a global maximum of minimum, as they are direct measurements of the radius of curvature in a cross-section of the specimen. A table with the vales of the centers of curvature and their corresponding distance to fracture can be found below. Note that those measures have been taken only for one of the two parts of the broken piece, as it is supposed to be symmetric. The 3D pictures have been taken for the two different pieces for every specimen but for the 99.5% of porosity and T_{amb}, where just one has been taken.

Specimen	**Radius 1** [μm] (**Distance 1** [μm])	**Radius 2** [μm] (**Distance 2** [μm])	**Radius 3** [μm] (**Distance 3** [μm])	**Radius 4** [μm] (**Distance 4** [μm])
99.5%, T_{amb}	3819.8	3529.8	3139.9	2669.9
	(9131.44)	(6269.13)	(3293.59)	(1476.58)
99.5%, 100°C	3834.8	3464.9	3124.9	2534.9
	(9062.25)	(6030.05)	(3862.36)	(1787.14)
99.5%, 150°C	3654.8	3319.9	2894.9	2374.9
	(9165.65)	(6191.11)	(4150.50)	(1913.95)
95%, T_{amb}	3699.8	3374.9	3064.9	2909.9
	(9257.78)	(6237.22)	(3309.00)	(2317.35)
95%, 100°C	3654.8	3369.9	3149.9	2799.9
	(924670)	(6226.33)	(4046.82)	(2478.84)
95%, 150°C	3479.9	3279.9	2839.9	2621.3
	(9074.21)	(6087.19)	(4020.37)	(1737.65)

Table 17: Radius of curvature and their corresponding distance to fracture.

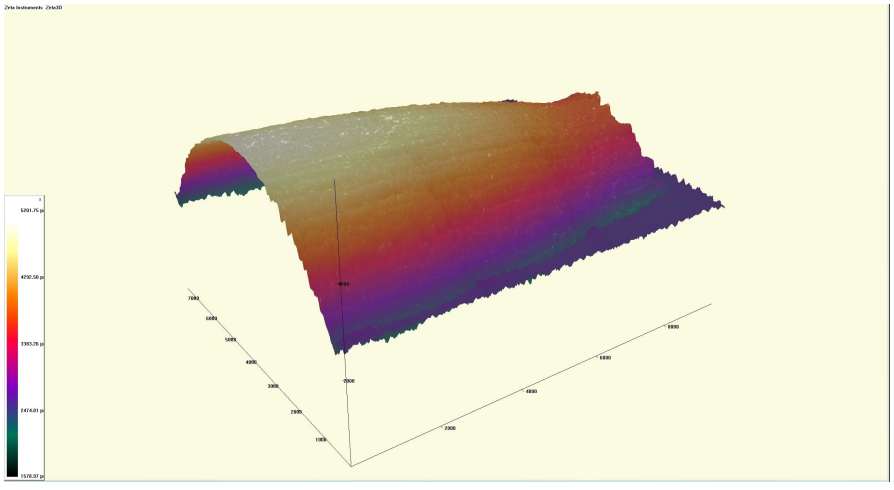

Figure 63: 3D Necking representation of a 99.5% porosity, T_{amb} specimen.

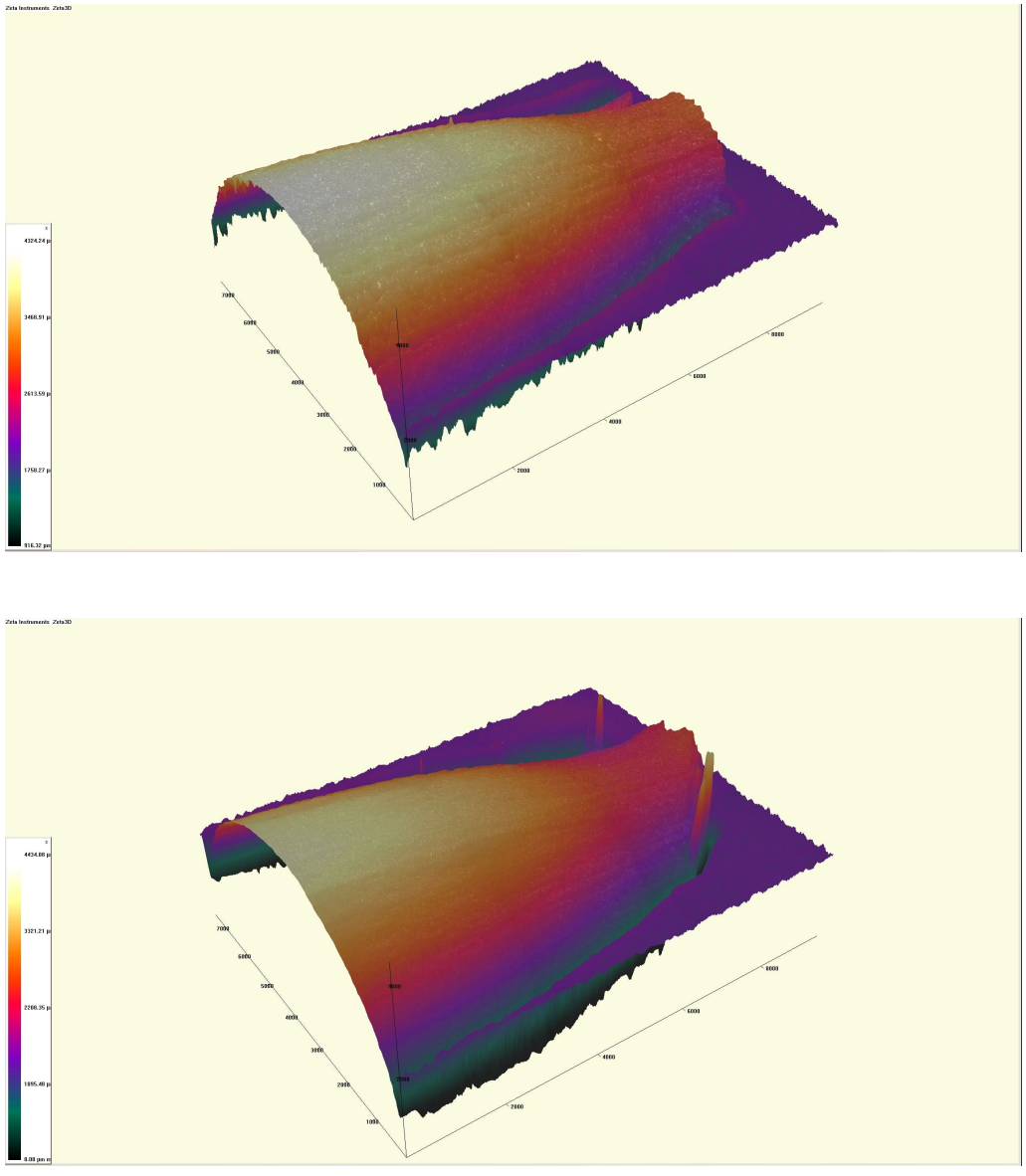

Figure 64: 3D Necking representation of a 99.5% porosity, 100°C specimen.

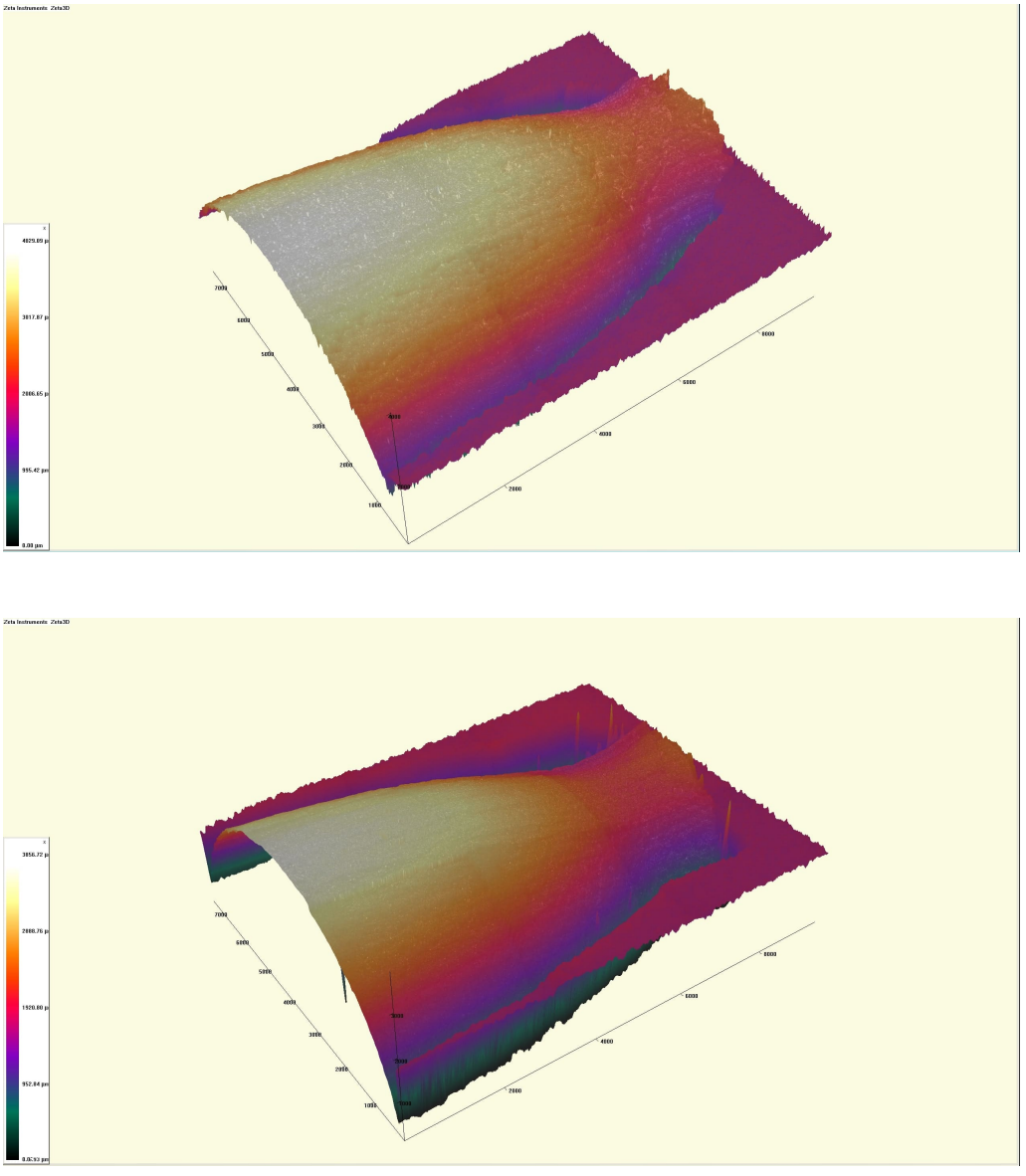

Figure 65: 3D Necking representation of a 99.5% porosity, 150°C specimen.

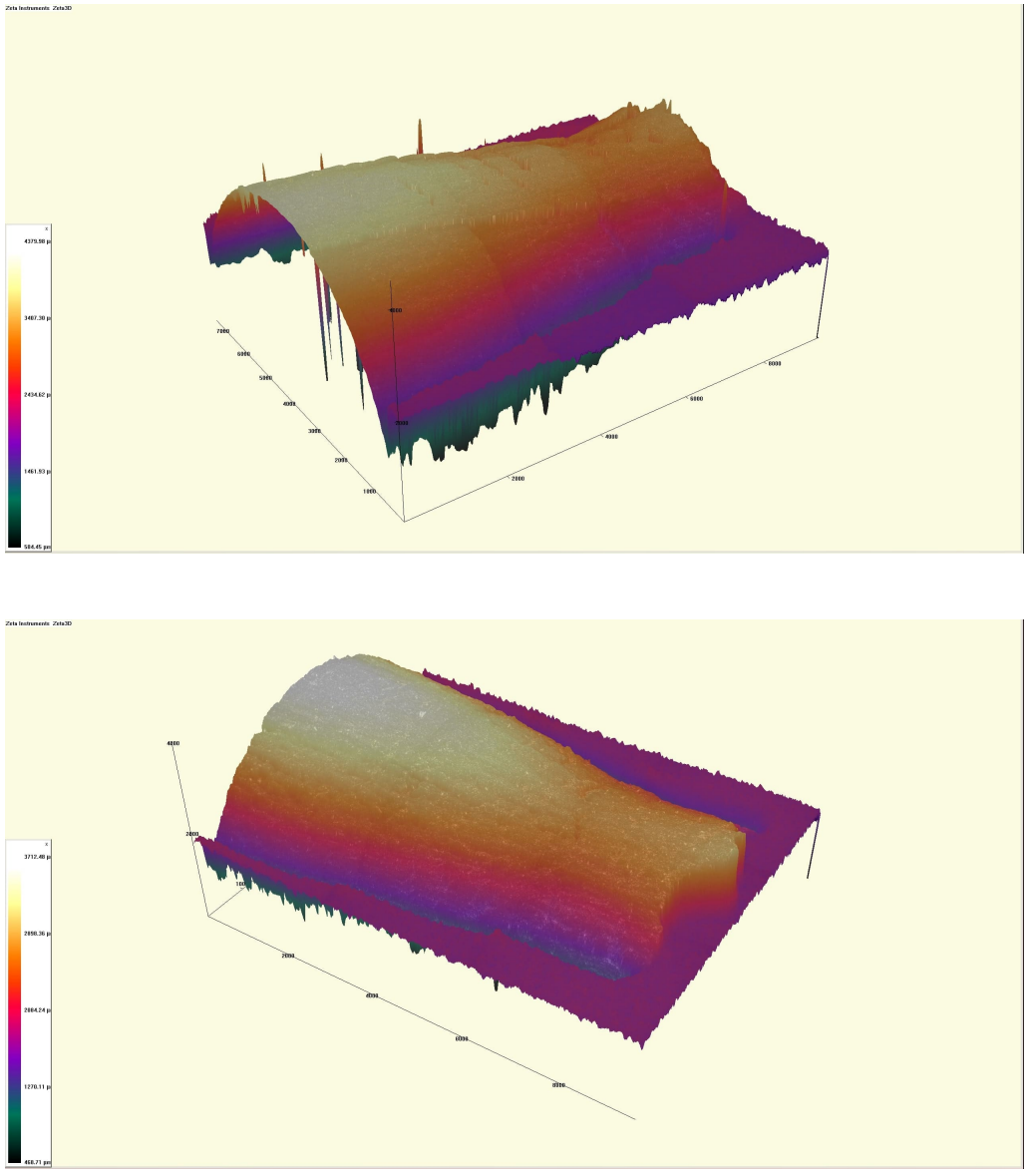

Figure 66: 3D Necking representation of a 95% porosity, T_{amb} specimen.

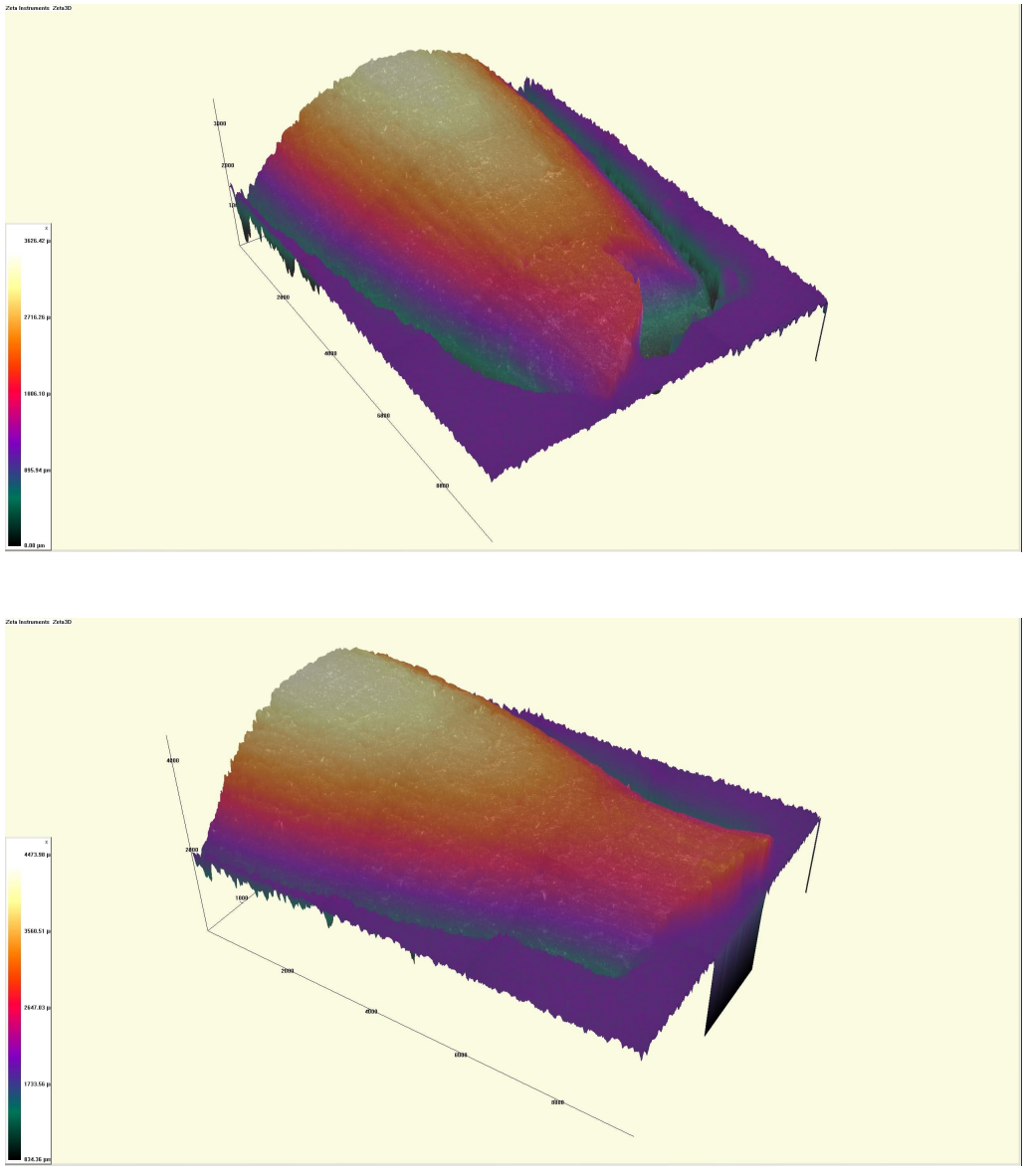

Figure 67: 3D Necking representation of a 95% porosity, 100°C specimen.

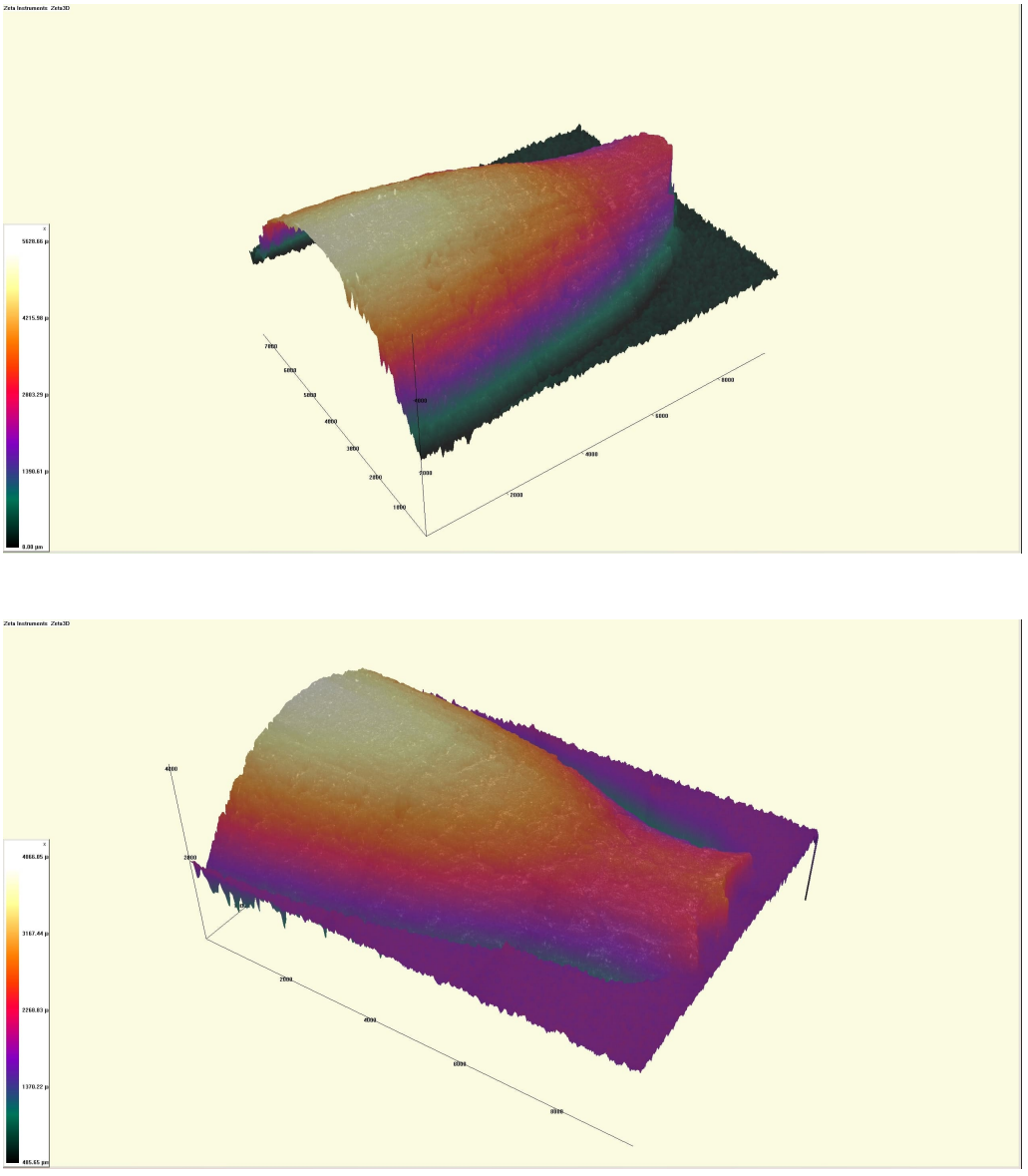

Figure 68: 3D Necking representation of a 95% porosity, 150°C specimen.

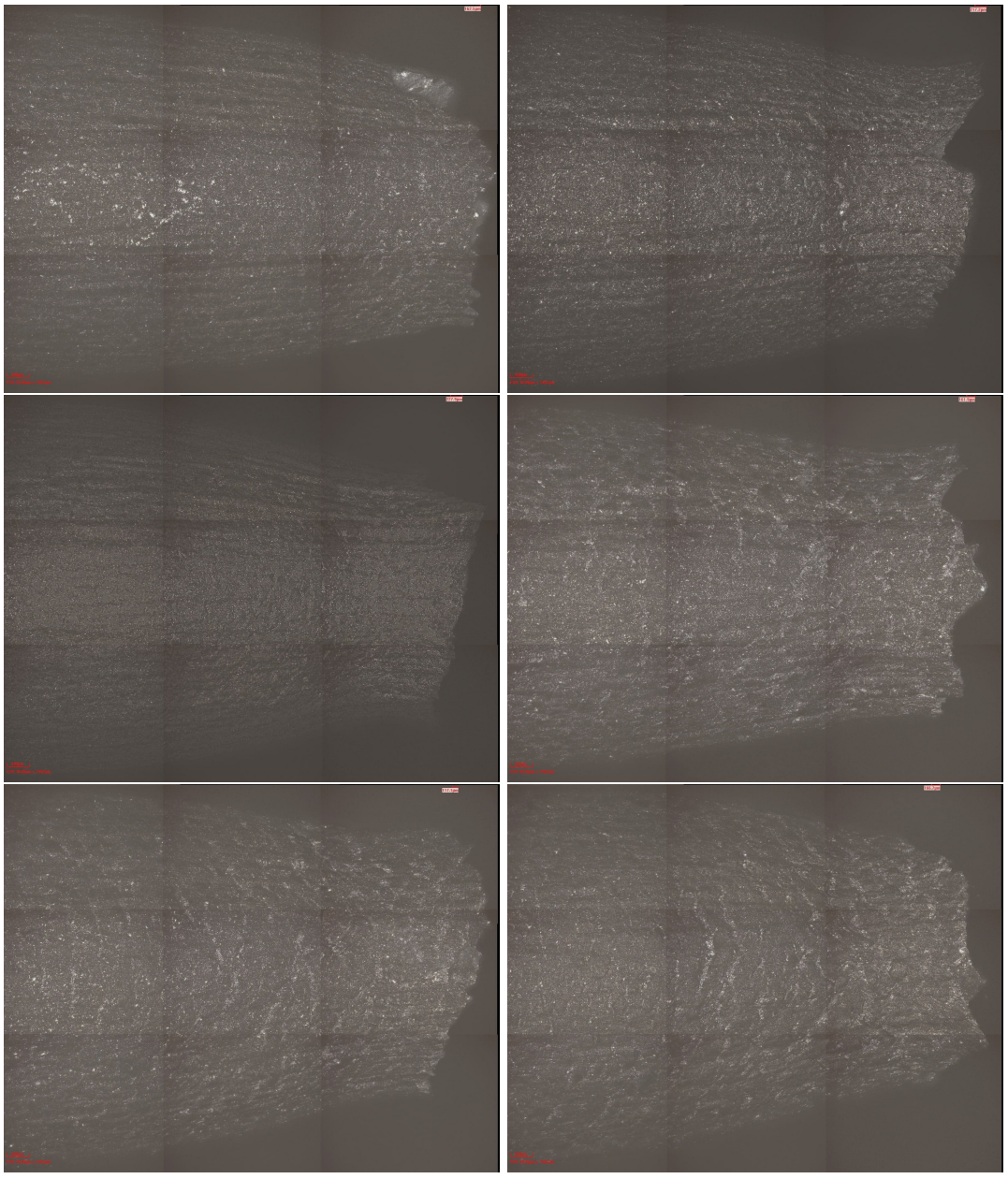

Figure 69: 2D Necking images. From left to right and from top to bottom, 99.5% porosity, T_{amb} specimen; 99.5% porosity, 100°C specimen; 99.5% porosity, 150°C specimen; 95% porosity, T_{amb} specimen; 95% porosity, 100°C specimen; 95% porosity, 150°C specimen.

Together with the image processing, the data from the previous table has been treated in order to get some valid information. First of all, the data has been transformed into dimensionless quantities, and afterwards plotted together to check if there exists changes with respect to temperature or porosity. An extra value of 4500 μm has been added for a distance of 12000 μm, which corresponds to the initial radius. Looking at the graphs, there is a decreasing trend in the radius of curvature when approaching the boundary.

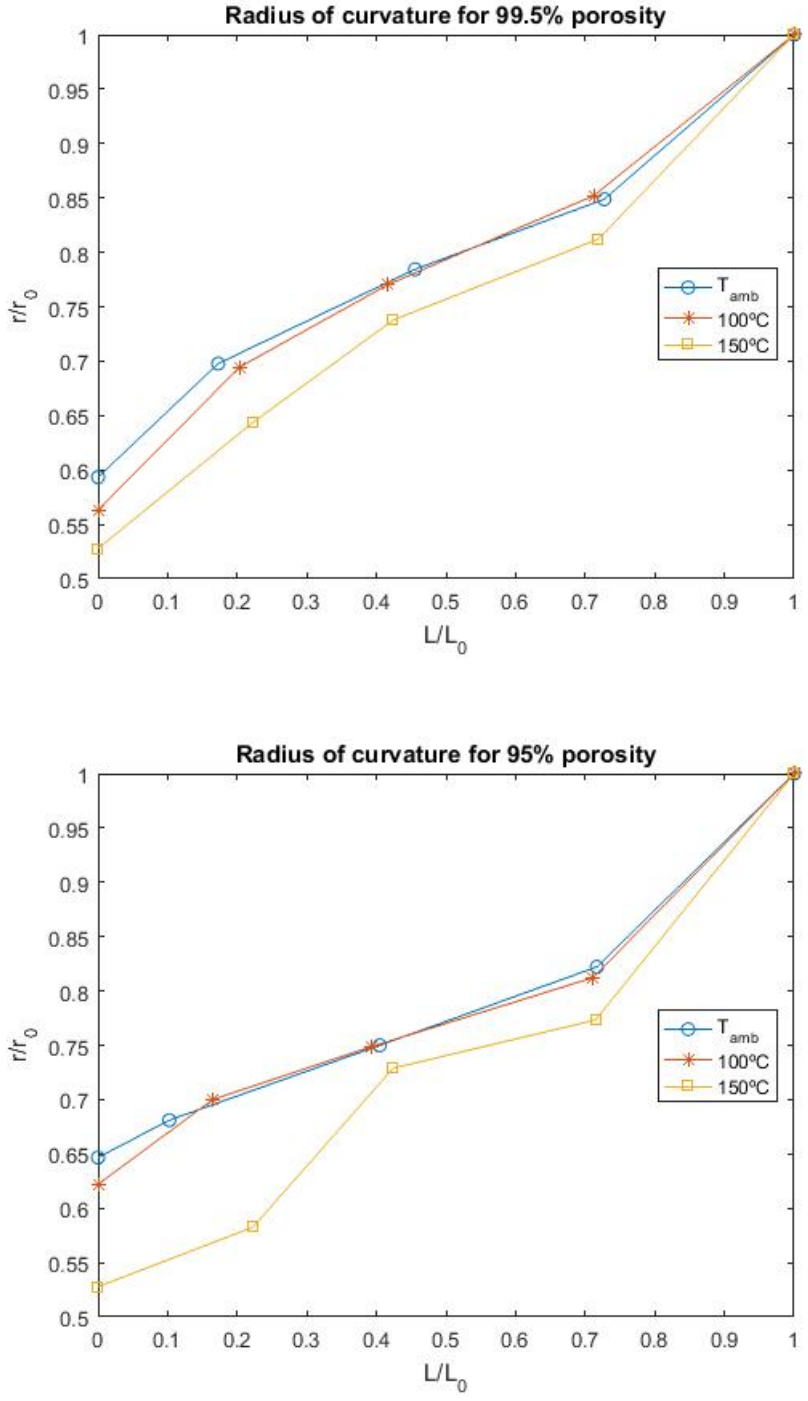

Figure 70: Radius of curvature as a function of distance to fracture. On the top, 99.5% porosity; on the bottom, 95% porosity.

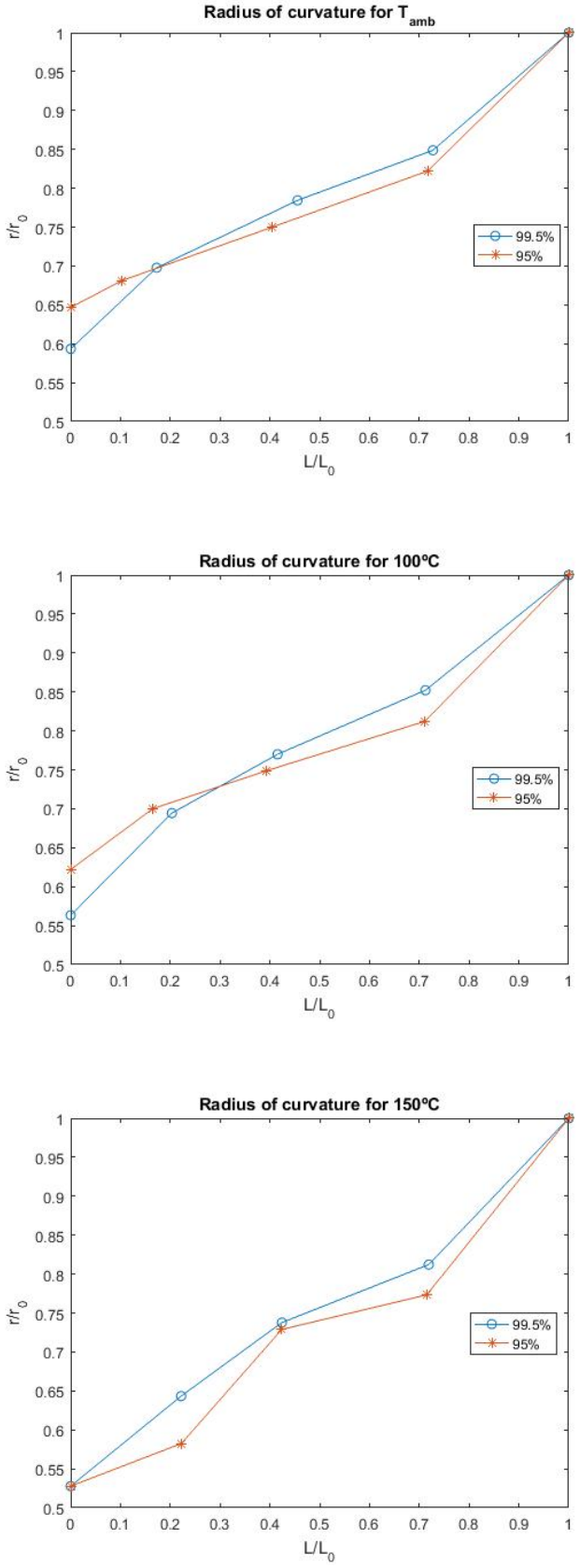

Figure 71: Radius of curvature as a function of distance to fracture. From top to bottom, T_{amb}; 100°C; 150°C.

The ratio $\Delta r/r_0$ has also been plotted.

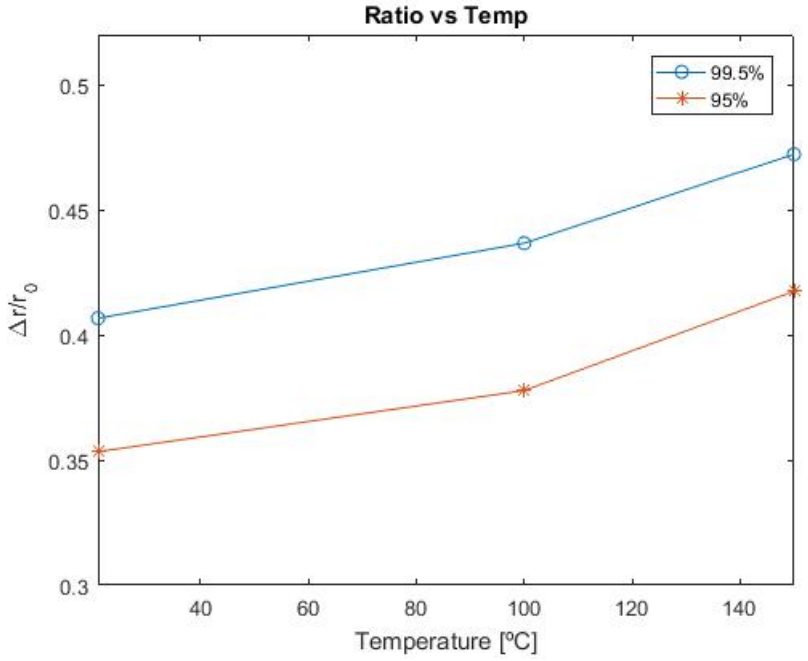

Figure 72: Ratio $\Delta r/r_0$ as a function of temperature.

6.4.1 Stretch marks

Even when looking at the tested specimens without the profilometer, it can be seen some stretch marks on the surface that were not there before the testing. Those marks are repeated along the whole surface of the specimen and in a more intense way when reaching the fracture zone. Every specimen shows them independently of its temperature or porosity.

As a further exploration, a few pictures have been taken of one of those stretch marks belonging to the 99.5% porosity, 100°C specimen.

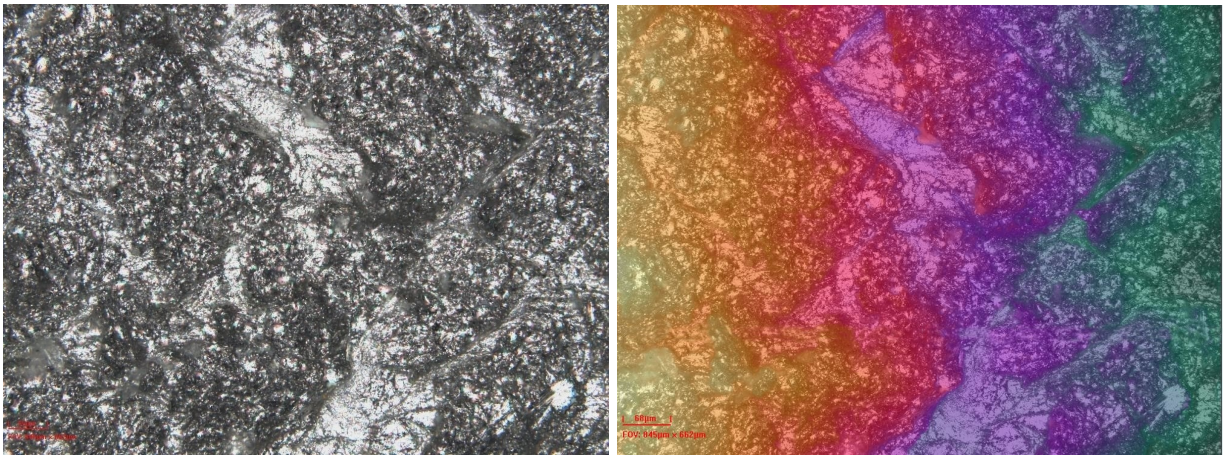

Figure 73: Stretch marks on a 99.5% porosity, 100°C specimen. On the left, 2D image; on the right, colored surface.

A total of eight measurements of the width have been taken along its path. The mean has been found to be 123.9, with a SEM of 7.8. It also looks like its trace follows a circle, more precisely, a circle with a radius of curvature of 828.0 μm. Finally, a 3D representation has been taken to clarify the shape of this stretch mark.

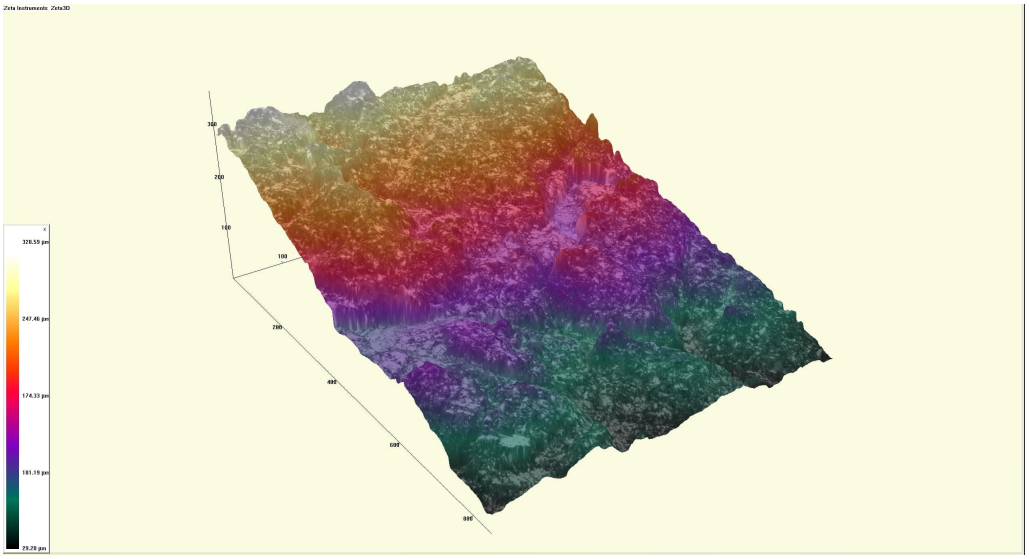

Figure 74: 3D Stretch mark on a 99.5% porosity, 100°C specimen and 20X augmentation.

7 Discussion

Regardless all of the figures and 3D representations, what must be highlighted are the results themselves, the information collected and plotted. While it is true that the pictures help to understand what is being done, they are useless without the accompaniment of good data. That is the main reason why not only pictures have been presented but also tables and plots showing that information in a more schematic way.

Following the order settled in the previous section, the **roughness** features are the first of the results that must be fully inspected. Both the profile and surface parameters, R_a and S_a, respectively, have been studied for a total of six different specimens, varying their porosity. What it has come up is that they present the same behavior, independently of the precision of the feature itself. While profile parameters can lead to errors due to the lack of information with which they work, in this case its behavior is the same as the surface parameter one, so its results are reliable. If R_a results were chaotic but S_a ones were more stable, it could have been stated that S_a works better for these type of measurements, but it is not the case for this investigation. This has happened because of the place where the inspections have been done. Initially, the measurements were made in the rounded surface of the specimen, and it led to errors due to the inconsistency of measuring the roughness with a profilometer that was not flattening the surface. When the place was changed and the measurements were taken in the correct place, which is the bottom part or the specimen that has remained untouched when the test were made, the results that are available now were obtained. Even with all of this in mind, R_a has higher values of the SEM, although they only vary in a slight way.

Figures 20 and 21 are the ones where the roughness graphs are shown. They can be commented together due to the similarities that are found. Two clear differentiated zones are presented: the one for the 5X augmentation and the one for the 20X. The two porosities vary among them but not in such a way as the difference that can be seen with the augmentations. 5X values are the highest, with mean R_a values of 18.17 for the 99.5% porosity and 21.39 for the 95% one, because of the field of vision that this augmentation has. As the surface inspected is higher, the possibility of finding higher peaks increases. And with the surface parameter it works in the same way, finding now mean values of 19.16 for the 99.5% porosity and 21.40 for the 95% one. What it has to be noted is that S_a measurements could have been taken selecting the whole screen area, but this would have not worked because of two reasons: if the selected zone had a crack, selecting the whole screen would have made impossible to avoid taking measurements there, and also because of the elimination of the possibility of taking more than one datum, what would have made it be selected as the correct one, throwing out the SEM. For the 20X augmentation, the data obtained have mean R_a values of 3.004 for the 99.5% porosity and 5.151 for the 95%, and mean S_a values of 2.641 for the 99.5% porosity and 3.776 for the 95%.

Concerning the variations as a result of the porosity, the values of the 95% of porosity are higher than the 99.5% ones. This is the quality grade employed by the supplier to fit their standards. Despite the fact that 99.5 is higher than 95, it does not mean that the 99.5% has more pores. What that number is indicating is the amount of occupied and free space that there is in the specimen. That is, the 95% will have a 5% of the space emptied with voids, while the 99.5% will only give a 0.5% of its whole space to that voids. Having more voids will increase the possibilities of fracture, either because of the coalescence of these pores into higher ones, making it difficult to endurance to the testing loads, or because of the voids themselves if they are big enough. But in the case of roughness it is not important the resistance but the surface that they provide. Finally, concerning the difference in temperature, the roughness remains unchanged for the three cases. Since the test should not make dissimilarities in the surface, the roughness parameters have to remain unaltered. Again, this is true because of the place where the measurements are taken. It has been seen in the results section that in the necked region, near the fracture surface, it appeared stretch marks after the testing of the specimens. If the inspection would have been made there, considering that the surface was planar, it will not have had any sense.

Subsequently, the **fracture surface** has been studied. Together with the various shapes that are presented, that are going to be reviewed with the necking, the maximum fracture height has been measured for each of the cases. The variation of this value has something to do with the ductility of the material.

Ductility is one of the main mechanical properties of metals, and it is measured as the elongation to failure of a sample during standard uniaxial tensile test, just as the tests that have been performed within this investigation. Some understanding problems arise here, with the confusion of ductility and plasticity. Ductility can be thought-out as tensile plasticity, but it is not the same. While ductility is affected by microstructure, plasticity depends on the crystal structure or the number of available slip systems to accommodate plastic deformation. Besides, ductility is

also related with the geometry of the specimen, particularly at high deformation velocities. The use of the cross-area reduction at fracture is a good indication of ductility for conventional metals [32].

What is observed in Figure 34 is a linear increase in maximum fracture height with temperature for both porosities. More tests at different temperatures should be done to guarantee the linear behavior or discover an asymptotic or parabolic one. This growth has a relation with ductility and temperature sensitivity, as when the temperature is increased, the ability of the particles to move increases too, therefore increasing ductility. If the metal is more ductile, its resistance to failure will increase, that is, it will be more difficult for the particles to fully separate and break the specimen. This will lead to thinner cross sections and, regarding maximum fracture height, higher values due to this plastic deformation that will be increased.

For the case of the porosity variation, 95% specimens show a slightly higher maximum fracture height than the ones with a 99.5% of porosity. In spite of the fact that for both porosities it grows with temperature, this increase in porosity should give a reduction in maximum fracture height. The tiny holes inside the lower porosity specimen should make it fail first, spending less time withstanding the load and increasing the height. For the higher porosity specimens what should occur is just the opposite, the lack of voids should increase the resistance to fracture, which will enable the formation of higher heights due to the force exerted by the particles between them to prevent breakage. The same will happen with the cross-section, that will be mentioned afterwards. But in this cases what results is just the opposite. Unfortunately, there is not enough data to come up with a reason, and more experiments should be done with a higher number of metals to try to understand it. Figure 75 below shows a ductile fracture, where the maximum fracture height formation can be studied.

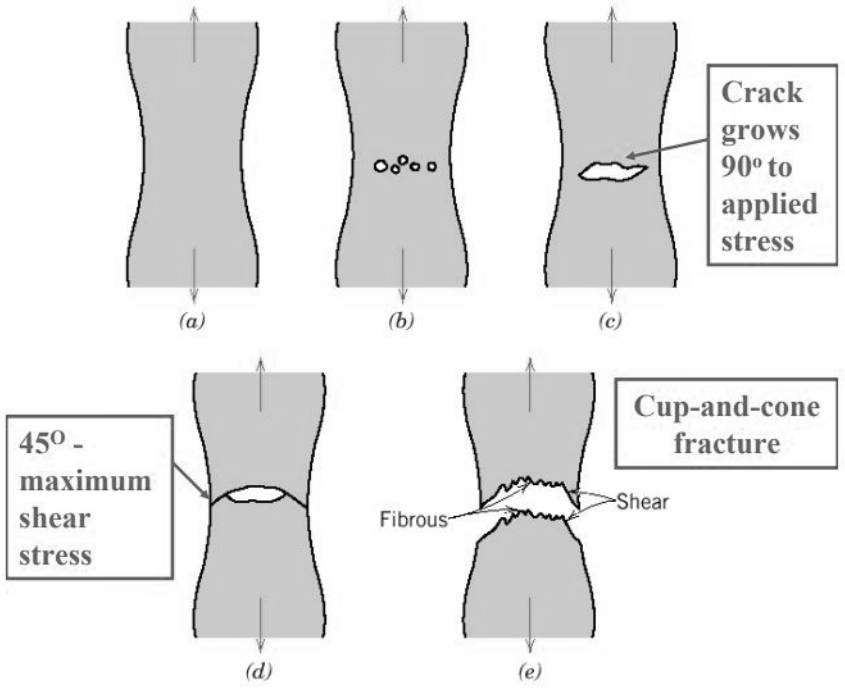

Figure 75: Ductile Fracture. (a) Necking, (b) Formation of microvoids, (c) Coalescence of microvoids to form a crack, (d) Crack propagation by shear deformation, (e) Fracture [9].

What deserves a further study is the **pores** section. Much information has been retrieved but many more would be necessary to assess an authentic conclusion. With the results obtained, a first guess can be stated about the coalescence of the pores and its nature during the test. The pore size differs depending on its formation, place and on the state where it is found. The pores inspected can be in their growth phase, can have suffered coalescence or can have remained unchanged during the whole process. For a proper solution, tomography may be advisable before and after the tests. Also, a higher number of pores should be investigated, and from more than one specimen of the same temperature and porosity. This takes too much time to be done within the scope of this project but it is fully recommended as future work. Anyhow, some discussion can be made with the information that is had.

Together with the area, an estimated diameter has been calculated, as computing the pore margins is done by hand and perfect circles are not possible to be made. Also, there are some pores with a more elliptic shape, but the diameter has been calculated too in order to make a small comparison between them even if it not real altogether. Regarding the shape of the pores, they are spherical in its majority. The ones that may appeared non-spherical with the 5X augmentation, turned out to be because of the coalescence of smaller spherical pores when changing to 20X. If the breakage has not been produced due to that specific pore, when the specimen failed they stopped agglutinating, finding therefore that weird shapes. In another hypothetic scenario, the inspected pore is the one that have caused failure. In that case, which is the one of big spherical pores, they ended their life with a higher volume and an almost spherical shape.

The place of the pores has been selected randomly. There are times when it is clear that the center of the piece is the one that have withstand the most, and the pore (or pores) that have contributed more to breakage can be found there, but that is not always the case. Also, it is expected that the size and amount of pores change depending on if they are more superficial or nearer to the core of the specimen, but again, another type of technology is needed in order to make these inspections. Previous figure would explain the belief of finding bigger pores in the center of the specimen rather than in the borders, as they begin their increase in the core. The diameter of the pores is interesting even knowing all of this. Leaving aside the solitary spherical pores, with diameters of more than 220 μm, in the coalescence process the diameter of the pores that have joint have close values. For the cases where there are many pores taking part on the coalescence, there are two categories: main pores leading that union (100-140 μm) and smaller ones accompanying in the process ($\sim$70 μm), but not having a decisive role in the process. This difference in size can be due to the formation or even because of a previous coalescence.

Finally, the **necking** has been examined. The radius of curvature has been computed for several cross-sections of the same specimen in order to see how they change with respect to the rest of the pieces. This serves as a checking method of ductile materials, and can be used as a good comparison mechanism. For Figures 70 and 71 where it is not the ratio $\Delta r/r_0$ the value that is being plotted, the measurements have been transformed to dimensionless numbers, as not every cross-section is placed in the same exact distance to fracture. The same has been done with the radius of curvature itself, making it dimensionless by taking at r_0 the value of the radius at a place where the necking did not take place, and the results show, one more time, how the specimens behave under different temperatures.

Following the explanation of a ductile tendency from above, the radius of curvature should be decreasing as it reaches the border of the fracture. This can be seen in the graphs, as for the same porosity, all the specimens apart from their temperature go from a smaller radius of curvature to a higher one when moving away from the border, that is, when L/L_0 goes to one. Also, these values decrease with temperature. When the temperature grows, the ability of the particles to move grows too, having more time to stretch and creating a thinner necked region, same as what occurred with the fracture surface. When comparing the radius of curvature for the two different porosities the values are almost the same but a little bit higher for the 99.5% of porosity. Although having similar values, 95% of porosity should have a bigger radius of curvature, as the higher number of pores will make it fail before, and the necked region will end having a higher cross-section. Possible sources of errors are, together with the lack of inspections to a wide range of specimens, the orientation of the piece when taking those measurements. Even supposing symmetry from the two broken pieces of the same specimen, axial symmetry is not necessarily found in the specimens. So, selecting a particular position will lead to a certain result that may not be the most precise one. A way of mitigating this error would be to take several measurements turning the specimen and compute the mean of each position. Even with this way it would be really hard, as taking a measurement at the same distance to fracture is not an easy task.

For the case of the ratio, the results are consistent. The ratio formula has r_0 in the denominator, so it will have the same value for every case. On the other hand, the numerator will be the substraction of $r_0 - r_f$. Having a lower value of r_f will lead to a higher numerator, and therefore to a higher ratio. It can be seen that the ratio increases with temperature for both porosities, showing the ductile behavior of the metal, and that for the same temperature, the value of the ratio of the 99.5% of porosity is higher, as it has a smaller radius of curvature. The reason why this graph is consistent but when comparing both porosities is not is because of the value of r_f. It is smaller for the 99.5% of porosities for the whole cases, but then it happen the other way around for the rest of the points. As the value that is used for the ratio is r_f and it is appropriate, it works.

Regarding the type of necking, which is translated to a type of fracture surface, the specimens can be divided in two groups: the ones having a shear lip formation and the ones with an asymmetric cross-sectional slip. The first group

is the one formed by the majority of the specimens, and will retrieve two pieces with convex and concave parts, also called “cup and cone failure”. The cup will correspond to concave part, while the cone will be the convex one. It is formed due to crack growths in the middle of the necked region. The second group is not that common among the investigated specimens, and it shows an inclined fracture surface. This last fracture mode is not as typical as the cup and cone failure in ductile fracture mechanisms.

Just as an hypothesis, the stretch marks that have been previously analyzed may be related wit the axial building direction. It feels like the circular marks can be linked with the layered deposition process of the metal during its printing, following the axial direction.

8 Conclusions

After analyzing how various Stainless Steel specimens with a variety of characteristics work under different temperatures, some data has been obtained and clear results have shown up. The specimens have been subjected to Uniaxial Tensile Tests until complete failure occurred, and afterwards they have been inspected with a profilometer, measuring their roughness, analyzing their pores and radius of curvature at necking, and retrieving 3D representations of their fracture surface and necking region.

The roughness has turned out to be constant for every temperature, while the roughness parameters decreasing with the augmentations. Also, the higher the porosity the lower the roughness will be, as having a higher porosity means leaving less space to voids that will damage the surface. Ultimately, the surface parameter S_a has been noticed that, although it is not as used as the profile parameter R_a, is more useful as it gives a more realistic information about the studied surface.

Ductility has also played a role in the investigation. This property measures the elongation to failure of a sample that is being subjected to a load. As being more ductile means having more resistance to failure, the higher the ductility the higher the maximum fracture height will be. It has been confirmed that ductility increases with temperature, as the maximum fracture height that the specimen will end having after the test increases with it. Besides, fracture height assumptions have been made with respect to porosity variations: it should increase with it as these specimens tend to withstand better the external load.

Regarding the pores, it has been realized that understanding them requires a high amount of time and various types of technology. Nevertheless, some pores have been inspected and several conclusions have been reached. Coalescense is common between voids, as well as normal growth, and it will end being the main cause of failure. They will have a spherical shape unless during the coalescence, where weird shapes can be detected, and their diameter cannot be standardized as it will depend on the pore formation, location of the surface and stage in which it is found when doing the inspection.

The last thing that has been studied is the necked region that the metal forms during the tensile test. Computing a ratio in which the initial and the final radius of curvature are included helps understanding how the specimens behave under the load. The final radius is found to decrease with temperature, which indicates one more time the increase of ductility with this factor. Having more ductility will decrease the radius of curvature. Also, this final radius is expected to be lower the higher the porosity is, but it is not easy to measure and disconcerting results can arise, so actions have to be taken to mitigate that possibility. Finally, the shape of the fracture will be a cup and cone failure, although some specimens can also break with an asymmetric cross-sectional slip, which has an inclined fracture surface.

9 Future work

This Bachelor Thesis is thought as a starting point in one of the main tasks for a bigger researching project. Having only a few months to investigate leaves a lot of unexplored fields that will take more years to analyze. In addition to it, the project has started just before the beginning of the thesis, and that has worked as a double-edge sword. It has had a positive part, which includes the amount and variety of topics that could be dealt with and the fact of being an open project with no boundaries. But it also has a negative part, which is the ignorance of the treated topics, the needed of understanding how the profilometer works, and the feeling of be giving blind steps sometimes as things were not known to be useful prior to the investigation. Once the project has started and the objectives clarified, selecting its scope has been the last step.

The future investigation lines should be based in the pores analysis. Taking a higher number of pores per specimen at each of the broken parts, from different fracture surface locations for a better comprehension of the results may be recommended. Also, trying to investigate through tomography the quantity, size and geometry of these pores regarding its location would be desirable, before and after performing the tests. This includes new technology that has to be learned and understood carefully. For the roughness, flat samples should be built in order to take roughness measurements without the need of taking them in the bottom of the specimen. Another interesting task would be to cut the specimens and look for pores nor only in the surface but inside the piece, without just tomography. Mixing both technologies in a balanced way can lead to more accurate results.

Following this procedure, the quality of the investigation outcomes can be increased having this report as a basis, learning from its errors and trying to improve the project with new features. Not only Uniaxial Tensile Test can be done, implementing new tests such as bending, impact (Charpy test), hardness, fatigue, corrosion resistance, wear... and non-destructive tests as well such as the tomography that has been previously mentioned. This will help to investigate more mechanical properties of the metal but will also increase the time and cost of the experiments. A good choice has to be made of whether a test is more interesting than another.

To conclude, the key factor in order to obtain strict results is to repeat the same steps for a wide range of specimens, as big as possible. The higher the number of inspected specimens the more accurate the results will be. For the same kind of specimen, with a certain temperature of porosity, many metal pieces should be built, and repetition of the tests and procedures for all of them should be made. Besides, extending the number of porosities and temperatures should be a must. Not only those features, investigating the specimens behavior under different orientations, adding to the actual axial orientation the flat and inclined ones, and extrapolating it to many more metals such as Titanium and Aluminum alloys will be the last point to settle a complete project.

10 Temporal planning

One of the key things for the correct resolution of a project is to plan beforehand all the activities that are needed to be done. It helps to list the number of tasks and try to set a logic and realistic order in the available time. It will therefore divide time in the most efficient way for the realization of all of the activities.

The project was selected on January 2019, and started at the end of the same month. A Gantt's diagram is included trying to represent in a clear way the distribution of the tasks. In addition to it, a table showing the exact initial and final dates, together with the duration of each of the activities is presented below.

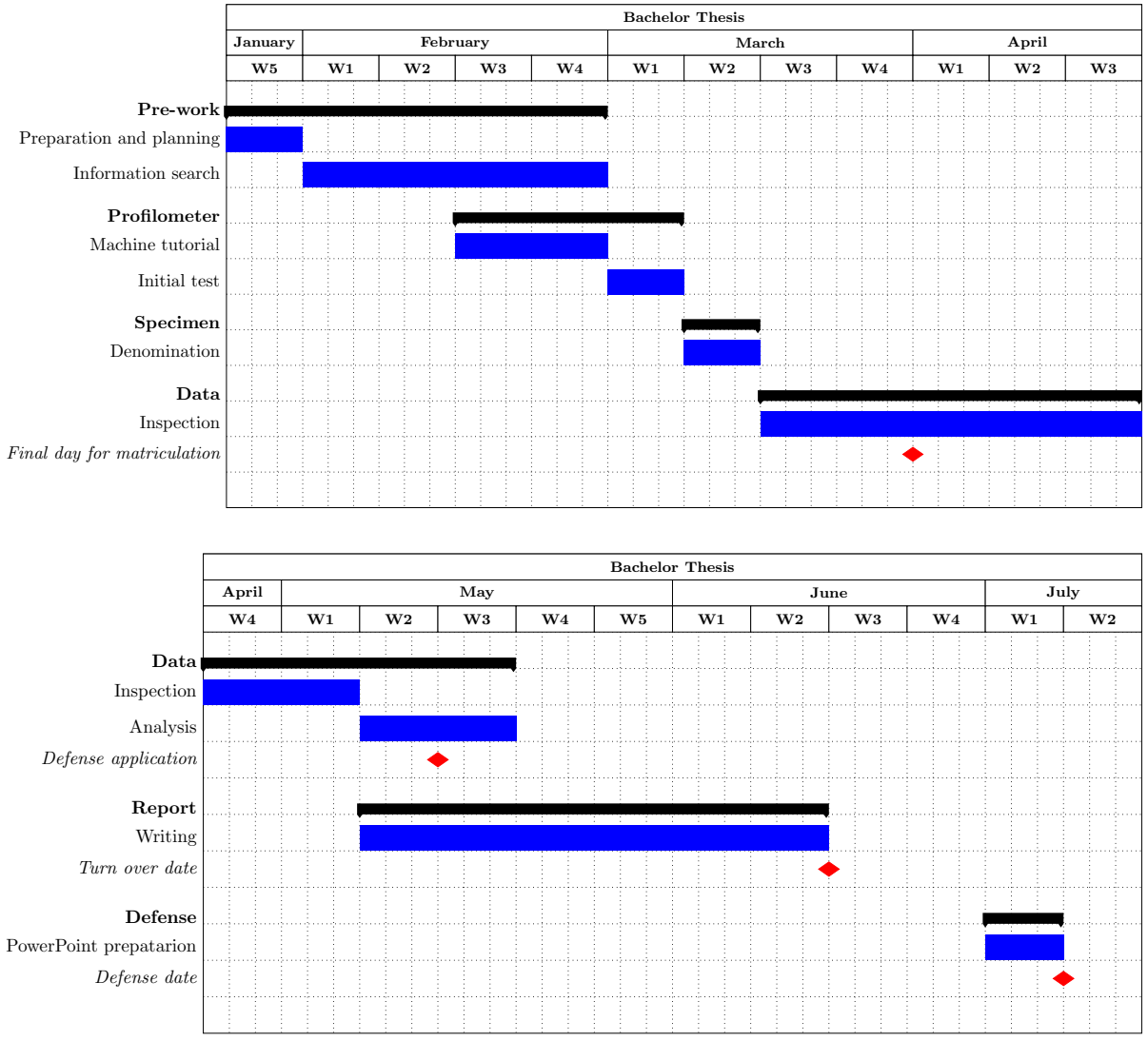

Figure 76: Gantt's diagram for the 2019 Bachelor Thesis.

Task	**Beginning date**	**Ending date**	**Duration [Days]**
Preparation and planning	28/01/2019	03/02/2019	7
Information search	04/02/2019	03/03/2019	28
Machine tutorial	18/02/2019	03/03/2019	14
Initial test	04/03/2019	10/03/2019	7
Specimen denomination	11/03/2019	17/03/2019	7
Data inspection	18/03/2019	05/05/2019	49
Data analysis	06/05/2019	19/05/2019	14
Report writing	06/05/2019	16/06/2019	42
Power Point preparation	01/07/2019	07/07/2019	7

Table 18: Temporal planning.

11 Budget

The Bachelor Thesis main goal is to begin with the analysis and investigation of a Stainless Steel printed with 3D technology. This process is part of an ambitious project where many other metals are involved. Because of that, this study is just a way of exploring what and how can things be done, and it will help as a tool for further investigations.

As the proposal was done when the project was already set, many of the materials needed were already bought, along with the profilometer machine. They were not only thought for this investigation, that is the reason why the specimens are not included in the costs sections. An amortization of the machine is done instead of stating its direct cost for the same reason.

The encompassed costs will therefore be indirect costs such as the time used by the different people that have participated and material costs like the machine amortization.

11.1 Personal cost

As it is a Bachelor Thesis, the student is guided with a Tutor, so both working hours are included in the personal costs. Moreover, the technicians have also taken a role in the investigation performing the Uniaxial Tensile Tests in the university facilities.

Job	**Employed hours**	**Cost per hour [€/h]**	**Total Cost [€]**
Tutor	50	70	3500
Technicians	10	70	700
Student	500	50	25000
Total			29200

Table 19: Personal cost.

11.2 Material cost

Without including the specimens cost provided by *Materialise*, the rest of the costs would be simply the machine one, which represents an important initial investment. The benefit is that, as the technology that it uses is cutting edge, its useful lifetime will be high enough not to increase the project final cost. It is supposed to last for 14 years, and it has an applied percentage of a 15%, so its amortization will be completed earlier.

Using a constant percentage method, the formula that is needed to calculate the profilometer cost will be the one that follows.

$$Cost = Initial\ cost \times Applied\ percentage \times \frac{Number\ of\ months\ used}{12\ months/year} \tag{5}$$

Machine	**Price [€]**	**Applied percentage [%]**	**Project duration [Months]**	**Total Cost [€]**
Profilometer	50000	15	3	1875

Table 20: Material cost.

In order to calculate how many years will it take to amortize the machine with this method, it has to be calculated how much time will it take to surpass the initial investment. By computing $50000/(50000 \times 0.15) = 6.66$ years are found, so it will be amortized long before the 14 predicted years.

11.3 Total cost

Concept	**Amount [€]**
Personal cost	29200
Material cost	1875
Total	31075

Table 21: Total cost.

The final cost of the investigation will be 31075 €, price that has to be incremented with a Value-Added Tax (VAT) of 21%. After all, the total Bachelor Thesis cost is 37600.75 €. It always has to be kept in mind that this is a fictitious approximation and that it is not real. However, it serves as a way of realizing that things have its associated cost and that the institution is making a big effort with their students.

References

[1] Cassiopée Galy, Emilie Le Guen, Eric Lacoste, and Corinne Arvieu. Main defects observed in aluminum alloy parts produced by slm: From causes to consequences. *Additive Manufacturing*, 2018.

[2] Andrew Townsend, N Senin, Liam Blunt, RK Leach, and JS Taylor. Surface texture metrology for metal additive manufacturing: a review. *Precision Engineering*, 46:34–47, 2016.

[3] Stainless steel grades and families: Explained. `https://www.unifiedalloys.com/blog/stainless-grades-families/`.

[4] Lewis Newton, Nicola Senin, Carlos Gomez, Reinhard Danzl, Franz Helmli, Liam Blunt, and Richard Leach. Areal topography measurement of metal additive surfaces using focus variation microscopy. *Additive Manufacturing*, 25:365–389, 2019.

[5] Karolien Kempen, Lore Thijs, Jan Van Humbeeck, and J-P Kruth. Mechanical properties of alsi10mg produced by selective laser melting. *Physics Procedia*, 39:439–446, 2012.

[6] WJ Brayshaw, AJ Cooper, and AH Sherry. Assessment of the micro-mechanical fracture processes within dissimilar metal welds. *Engineering Failure Analysis*, 97:820–835, 2019.

[7] Imade Koutiri, Etienne Pessard, Patrice Peyre, Ouafae Amlou, and Thibaut De Terris. Influence of slm process parameters on the surface finish, porosity rate and fatigue behavior of as-built inconel 625 parts. *Journal of Materials Processing Technology*, 255:536–546, 2018.

[8] R Rashid, SH Masood, D Ruan, S Palanisamy, RA Rahman Rashid, J Elambasseril, and M Brandt. Effect of energy per layer on the anisotropy of selective laser melted alsi12 aluminium alloy. *Additive Manufacturing*, 22:426–439, 2018.

[9] Mse 2090: Introduction to materials science. chapter 8, failure. `http://people.virginia.edu/~lz2n/mse209/Chapter8.pdf`.

[10] Surface metrology guide. `https://guide.digitalsurf.com/en/guide.html`.

[11] Stainless steel - grade 316 (uns s31600). `https://www.azom.com/article.aspx?ArticleID=863`.

[12] Mterialise: Stainless steel (316l or 1.4404). `https://www.materialise.com/en/manufacturing/materials/stainless-steel`.

[13] Dimitris Mourtzis, Anastasios Vasilakopoulos, Evagoras Zervas, and Nikoletta Boli. Manufacturing system design using simulation in metal industry towards education 4.0. *Procedia Manufacturing*, 31:155–161, 2019.

[14] All about the steel industry. `https://www.worldatlas.com/articles/all-about-the-steel-industry.html`.

[15] Metals industry: Growth strategies to outlast commoditization. `https://www.strategyand.pwc.com/strategythatworks/growth/metalsindustry`.

[16] The economic times: Steel. `https://economictimes.indiatimes.com/industry/indl-goods/svs/steel/steel-industry-needs-to-prepare-for-advancements-in-processing-and-manufacturing/articleshow/57254780.cms`.

[17] Alex Roschli, Katherine T Gaul, Alex M Boulger, Brian K Post, Phillip C Chesser, Lonnie J Love, Fletcher Blue, and Michael Borish. Designing for big area additive manufacturing. *Additive Manufacturing*, 25:275–285, 2019.

[18] Diego Manfredi, Flaviana Calignano, Manickavasagam Krishnan, Riccardo Canali, Elisa Ambrosio, and Eleonora Atzeni. From powders to dense metal parts: Characterization of a commercial alsimg alloy processed through direct metal laser sintering. *Materials*, 6(3):856–869, 2013.

[19] Milad Hamidi Nasab, Dario Gastaldi, Nora Francesca Lecis, and Maurizio Vedani. On morphological surface features of the parts printed by selective laser melting (slm). *Additive Manufacturing*, 24:373–377, 2018.

[20] Thomas G Spears and Scott A Gold. In-process sensing in selective laser melting (slm) additive manufacturing. *Integrating Materials and Manufacturing Innovation*, 5(1):2, 2016.

[21] Grade data sheet. `http://www.atlassteels.com.au/documents/Atlas_Grade_datasheet_316_rev_Jan_2011.pdf`.

[22] Ccd sensor. `https://www.parentesis.com/tutoriales/Sensor_CCD_o_CMOS_Que_significa_todo_esto`.

[23] Focus-variation in comparison. `https://www.alicona.com/en/news-detail/newsitem/focus-variation-in-comparison/`.

[24] P Ponnusamy, SH Masood, D Ruan, S Palanisamy, and Rizwan Rashid. High strain rate dynamic behaviour of alsi12 alloy processed by selective laser melting. *The International Journal of Advanced Manufacturing Technology*, 97(1-4):1023–1035, 2018.

[25] KG Prashanth, S Scudino, HJ Klauss, Kumar Babu Surreddi, L Löber, Z Wang, AK Chaubey, U Kühn, and J Eckert. Microstructure and mechanical properties of al–12si produced by selective laser melting: Effect of heat treatment. *Materials Science and Engineering: A*, 590:153–160, 2014.

[26] Twi: What is hot cracking (solidification cracking)? `https://www.twi-global.com/technical-knowledge/faqs/faq-what-is-hot-cracking-solidification-cracking`.

[27] John Slotwinski, April Cooke, and Shawn Moylan. Mechanical properties testing for metal parts made via additive manufacturing: a review of the state of the art of mechanical property testing. *National Institute of Standards and Technol-ogy*, 2012.

[28] R Prokić Cvetković, O Popović, R Jovičić, N Milošević, Z Burzić, and I Cvetković. Microstructural and fracture analysis of microalloyed steel weld metal. *Procedia Structural Integrity*, 13:2221–2226, 2018.

[29] Nikita Khlystov, Daniel Lizardo, Keisuke Matsushita, and Jennie Zheng. Uniaxial tension and compression testing of materials. 2013.

[30] Graphpad statistics guide. `https://www.graphpad.com/guides/prism/7/statistics/stat_semandsdnotsame.htm?toc=0&printWindow`.

[31] Roger Lumley. *Fundamentals of aluminium metallurgy: production, processing and applications*. Elsevier, 2010.

[32] YT Zhu and XL Wu. Ductility and plasticity of nanostructured metals: differences and issues. *Materials Today Nano*, 2018.

Annex

Profilometer tool

The views of the tool that has been used together with a hex nut to put the specimen and ease the inspections, eliminating any type of movement, are included.

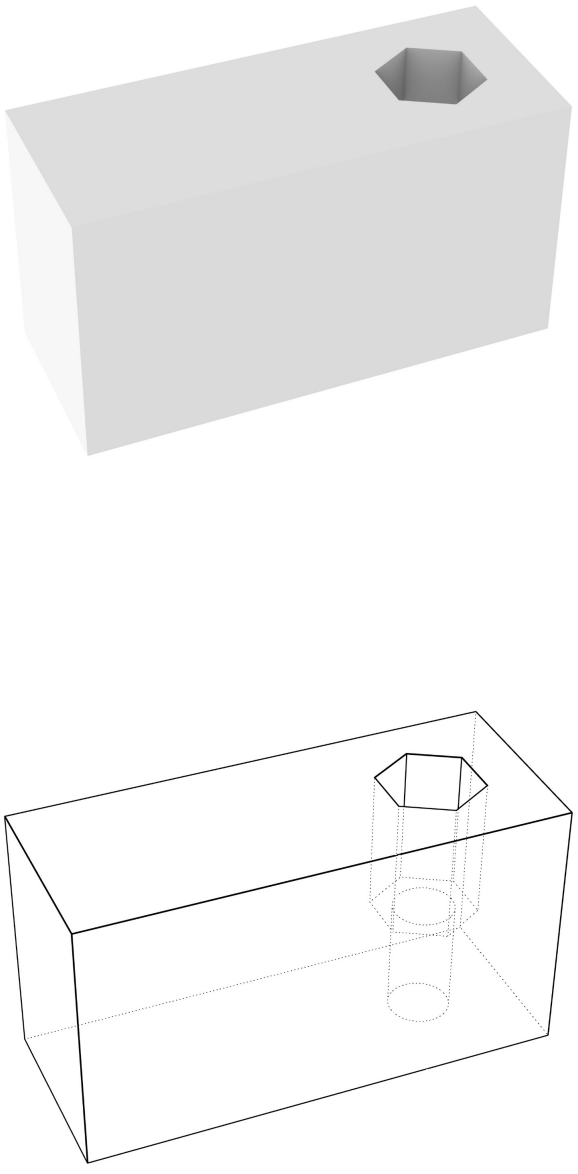

Figure 77: 3D Profilometer tool views.

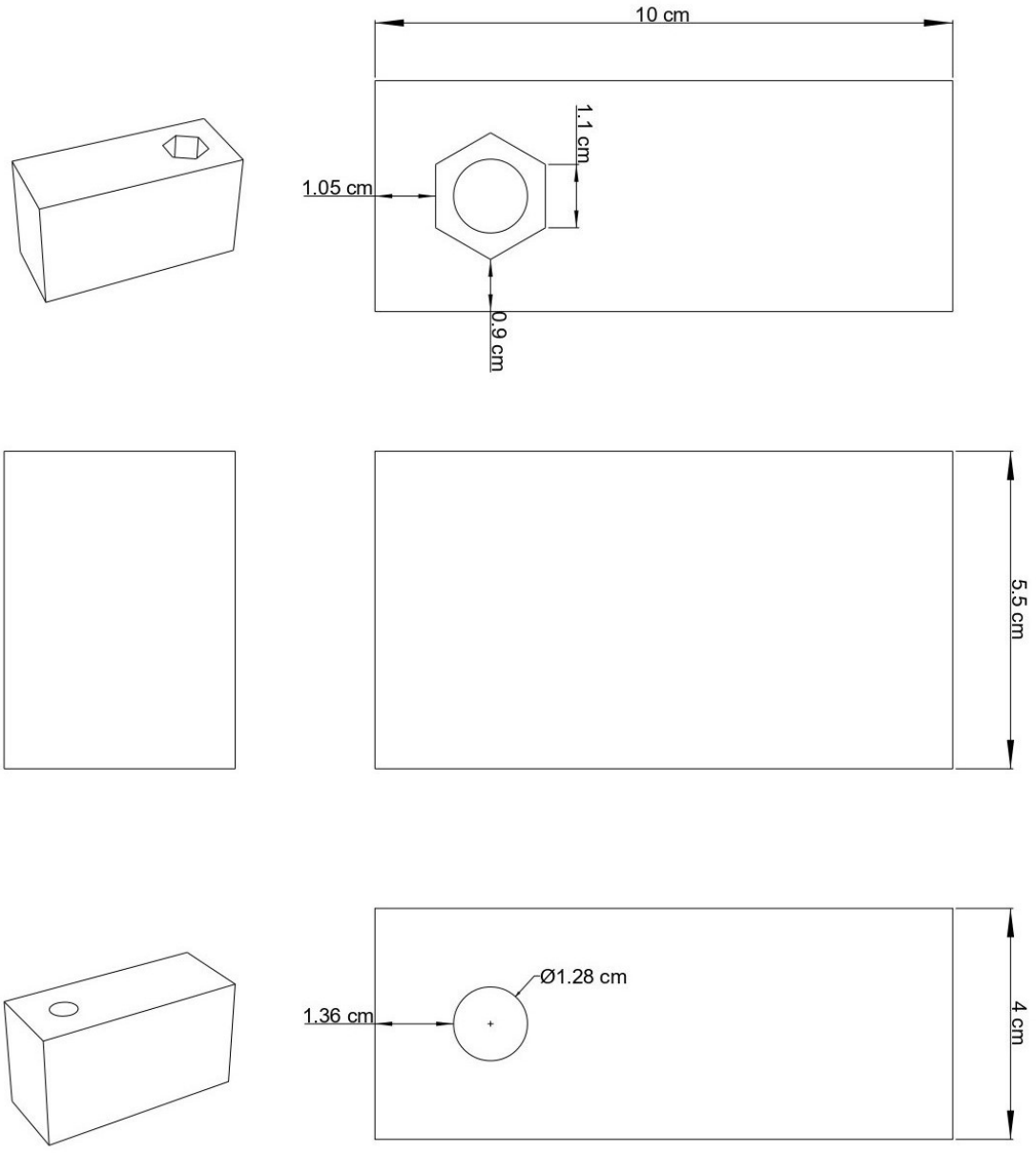

Figure 78: Views and measurements of the profilometer tool.